COUPLED MICROSCALE ELECTROPHORESIS AND ELECTROCHEMISTRY: A VERSATILE PLATFORM FOR LABEL-FREE DETECTION, MANUFACTURE OF ENCAPSULATED MICROBUBBLES AND PROTEIN CRYSTALLIZATION

A Dissertation

by

YU-WEN HUANG

Submitted to the Office of Graduate and Professional Studies of
Texas A&M University
in partial fulfillment of the requirements for the degree of

DOCTOR OF PHILOSOPHY

Chair of Committee,	Victor M. Ugaz
Committee Members,	Yue Kuo
	Arul Jayaraman
	Hae-Kwon Jeong
Head of Department,	M. Nazmul Karim

December 2013

Major Subject: Chemical Engineering

ABSTRACT

Microfluidics has geniuses of low consumption of reagents and sample, miniaturization of device, and fast turnaround time for analysis that enables to develop high-speed, high-resolution, portable bio-analysis devices to be immediately used at the point-of-care and homebased assays. Here, we established a versatile microfluidic system incorporating micro-arrays of individually addressable electrodes (patterned along the microchannel floor, 50 µm wide, 250 µm edge-to-edge spacing) that make it possible to transport charged macromolecules from the bulk solution to an electrode surface where they become compacted into an ultra-thin film. Using this principle, we focused on seeking new detection strategies (label-free detection), new applications (encapsulated microbubble synthesis, protein crystallization), and tried to get the diagnostics method out of the laboratory by using pervasive smartphone optics.

First, we used DNA as a probe to build up a label-free detection system with microfabricated platinum electrode arrays in free solution and without the need of conventional labeling. Simply applying a DC potential (1-3 V) and illuminating the electrode surface, we could observe the surface reflectivity of microbubbles responsible from the electrolysis of water (with a threshold of ~1.3 V), which is stabilized by the highly compacted DNA film at the electrode surface. This effect is reversible and can be applied to proteins and other charged analytes to be detected. The interplay between microscale electrokinetics and electrochemistry can also be harnessed to simultaneously

confine macromolecular encapsulants near an electrode surface while inflating them with electrochemically generated gasses to synthesize tunable encapsulated microbubbles.

Microfabricated chromium electrode arrays demonstrate another unlabeled detection approach by monitoring electrode degradation under ordinary white-light illumination. This reaction is highly compositional and size dependence that provides a possibility for real-time PCR detection application. Further, since dissolution is readily observable owing to the relatively large electrode sizes involved, we incorporated this microsystem with an Apple iPhone 4S to demonstrate the feasibility of smartphone-based detection for near point-of-care application.

Protein crystallization has also been demonstrated by transparent electrode arrays with hen egg white lysozyme *via* electrokinetic actuation to pre-concentrate protein molecules and to migrate the movement of certain ions simultaneously that enables to obtain single crystals in a short timescale (1-2 hours) and without previous purification. This technique provides capabilities for a straightforward interface of *in-situ* x-ray diffraction structural analysis to be performed as the protein formed inside the system.

DEDICATION

I would like to dedicate this doctoral dissertation to
My dear parents, Prof. Wen-Liang Huang and Ms. Shih-Fang Fu;
My beloved husband, Dr. Chieh-Wei Chang;
My adorable babies, Vivian and Lucas.

Thanks for always being there for me. Without your support, love and encouragement, I could not have completed this process.

ACKNOWLEDGEMENTS

First of all, I would like to express my deep gratitude for the invaluable assistance and guidance provided to me during my Ph.D. study and research from my dear advisor, Dr. Victor M. Ugaz. His patience, frankness, and devotion to his work inspired me to solve many problems and to accomplish lots of goals. I obtained a number of perspectives from him, not only on research ideas but also on values of life, which will benefit me for a long way and entirely enrich the word “advisor” to me.

I would also like to thank my committee members, Dr. Yue Kuo, Dr. Arul Jayaraman, Dr. Hae-Kwon Jeong, and Dr. Gyula Vigh, for their time and guidance throughout the course of this research.

Thanks also go to my all friends in College Station and the department faculty and staff, especially my colleagues in microfluidic laboratory, Roger, Tony, Serdar, Faisal, Airlong, Nan, Radha, Fanxu, Aashish, Contreras, and Duanduan, for their assistance in my study life and for making my time at Texas A&M University a great experience.

Last but not least, I would like to gratefully thank my parents for their support and encouragement to pursue my Ph.D. degree, and my husband for his love and company to help me keeping moving forward whenever I faced difficulties and obstacles. Also, thanks to God for giving my family the gorgeous babies, Vivian and Lucas, who bring shine and joy for us every day so we can forget the tough times.

NOMENCLATURE

µ-TAS	Micrototal-Analysis-Systems
POC	Point-of-Care
HIV	Human Immunodeficiency Virus
MS	Mass Spectrometry
NMR	Nuclear Magnetic Resonance
SPR	Surface Plasmon Resonance
NEMS-MS	Nanoelectromechanical System-Based MS
DNA	Deoxyribonucleic Acid
dsDNA	Double Stranded DNA
PCR	Polymerase Chain Reaction
qPCR	Quantitative PCR
NAT	Nucleic Acid Testing
LOD	Low Limit of Detection
PBS	Phosphate Buffer Saline
SDS	Surfactant Sodium Dodecyl Sulfate
AOT	Dioctyl Sodium Sulfosuccinate
CMC	Critical Micelle Concentration
PFB	Perfluorobutane
CEHDA	Coaxial Electrohynamic Atomization
PDMS	Polydimethylsiloxane

TABLE OF CONTENTS

Page

ABSTRACT ii

DEDICATION iv

ACKNOWLEDGEMENTS v

NOMENCLATURE vii

TABLE OF CONTENTS viii

LIST OF FIGURES xi

LIST OF TABLES xix

I. INTRODUCTION 1

- 1.1 Microfluidics Meets Requirements of Point-of-Care Applications 1
- 1.2 Strategies for Detection of Biomolecules in Microfluidic Systems 6
- 1.3 Current Technologies and Challenges of Nucleic Acid Testing for Microfluidic-Based Point-of-Care Applications 13
- 1.4 Motivation and Objectives 18

II. A MICROFLUIDIC PLATFORM FOR PRE-CONCENTRATION AND LABEL-FREE DETECTION OF DNA BY USING ON-CHIP ELECTRODE ARRAYS 22

- 2.1 A New Label-Free Detection Approach Performed in Free Solution 22
- 2.2 Morphological Characteristics of the Compacted DNA Layer 26
- 2.3 Mechanism of Macromolecular Transport and Compaction 29
- 2.4 Kinetic Analysis of Microbubble Cloud Formation 34
- 2.5 Materials and Methods 38

Page

III. UNLABELED DETECTION OF DNA VIA ELECTROCHEMICAL DISSOLUTION OF MICROFABRICATED CHROMIUM ELECTRODE ARRAY 42

3.1 A Novel Unlabeled Detection Approach by Using Highly Reactive Chromium Electrode Array 42
3.2 Compositional and Size Dependence of the Chromium Dissolution Kinetics 45
3.3 Possibility for Real-Time PCR Detection Application 49
3.4 Application for Smartphone-Based Detection of Unlabeled DNA 51
3.5 Possible Approaches for Quantification and Explication of the Dissolution Kinetics 52
3.6 Progress and Outlook 56
3.7 Materials and Methods 57

IV. TUNABLE SYNTHESIS OF ENCAPSULATED MICROBUBBLES BY COUPLED ELECTROPHORETIC STABILIZATION AND ELECTROCHEMICAL INFLATION 59

4.1 Challenges, Limitations and Applications of Microbubbles 59
4.2 A Single Device for Tunable Size of Encapsulated Microbubble Preparation *via* Electrochemically Microfluidic Actuation 61
4.3 Surfactant-Coated Microbubbles Formation *via* Different Power Strategy 65
4.4 Surfactant-Coated Microbubble Formation under Different Surfactant Concentration 67
4.5 Materials and Methods 72

V. APPLICATION FOR ELECTROKINETICALLY ACTUATED PROTEIN CRYSTALLIZATION BY USING ON-CHIP ELECTRODE ARRAYS 73

5.1 Challenges and Conventional Methods of Protein Crystallization 73
5.2 New Strategy for Protein Crystallization Using an Internal Electric Field 78
5.3 Preliminary Studies of Lysozyme Single Crystals 81

Page

5.4 Materials and Methods 83

VI. CONCLUSIONS AND FUTURE WORK 84

6.1 Summaries and Conclusions 84
6.2 Future Work 86

REFERENCES 94

LIST OF FIGURES

Page

Figure 1.1 Annual trends in the number of publication for microfluidic-based point-of-care, point-of-care, and DNA biosensor. The terms “microfluidic point of care detection*”, “point of care diagnostic*”, “point of care detection*”, “gene array*”, “gene chip*”, “DNA biosensor*”, “DNA array*”, “DNA sensor*”, “genosensor*”, “DNA biochip*”, “DNA chip*”, “DNA microarry*” have been considered. The literature search was done using ISI’s Web of Science (http://www.isiknowledge.com), accessed October 2012 2

Figure 1.2 The ideal POC diagnostic device, which can quantitatively detect several analytes, within minutes, at femtomolar sensitivity from 1 μL of bodily fluid and report the result. This ideal device is disposable and the mass manufacturing material cost would be less than $1. It does not exist now but the research progress in microfluidics and material science point toward the realization of such a POC device in the near future.. 5

Figure 1.3 The typical optical detection methods. (a) Fluorescence (in this case, fluorescent resonance energy transfer/FRET), (b) absorbance, (c) luminescence, and (d) surface plasmon resonance (SPR)-based optical detection methods. GFP: green fluorescent protein; YFP: yellow fluorescent protein; GS: glass substrate 10

Figure 1.4 The typical electrochemical detection methods for microfluidics: (a) amperometric, (b) potentiometric, and (c) conductometic (capacitively coupled conductivity detector) detection....................... 11

Figure 1.5 Nanoelectromechanical system-based MS (NEMS-MS) developed by Roukes’s group in Caltech. (a) the simplified schematic of the experimental configuration for first-generation NEMS-MS system, (b) the NEMS mass spectrometry of a gold nanoparticle dispersion, and (c) real-time records of single-molecule adsorption events on a NEMS mass sensor from their experiments....................................... 12

Figure 1.6 Selected technologies for POC NAT. (a) Detailed schematic of Cepheid’s GeneXpert cartridge, nucleic acid purification valve body, and cartridge valve body. (b) Detail of Liat Analyzer operation. The analyzer can automatically perform the nucleic acid testing steps and report results within 1h from a sample such as whole blood 15

Figure 2.1 (a) Microdevice design incorporating a glass microchannel (275 x 45 µm cross-section) bonded to a Si substrate patterned with an Pt microelectrode array (50 µm wide, 250 µm edge-to-edge spacing). (b) Compaction of DNA fluorescently labeled with YOYO-1 dye yields a bright zone at the anode upon application of 1-2 V. (c) At higher potentials (2.5 V), the same arrangement enables detection of unlabeled DNA under oblique white light illumination...................... 24

Figure 2.2 (a-d) Label-free detection of a 100 bp dsDNA ladder sample initially at 12 µg/mL in 1x TBE, 2.5 V. The compacted DNA layer appears as (a) a dark zone when illuminated from above, and (b) a brightly reflective zone when illuminated from the side. (c) The reflective zone dissipates within 5-10 s after the potential is removed, and (d) can be transported between neighboring electrodes upon switching the potential. (e-h) Similar reflectivity is observed with proteins. Unlabeled egg white lysozyme (initially at 10 mg/mL in 1x TBE, 2.5 V) becomes visible within 10-20 s either (e) at the cathode, pH = 8, or (f) at the anode, pH = 11. (g) Unlabeled prostate specific antigen (initially at 0.1 mg/mL in PBS at pH = 7.2, 2.5 V). (h) Label-free detection of heptakis (6-O-sulfo)-β-cyclodextran (MW = 1,849 Da) initially at 100 µg/mL in 1x TBE, 3 V. Scale: all electrodes are 50 µm wide horizontally 25

Figure 2.3 (a-d) Reflective zones evident when unlabeled DNA is compacted and viewed under oblique white light (left) are attributable to formation of a stable microbubble layer that can be seen under transmitted polarized illumination (right). In panel (d) the DNA has become ultra-concentrated by sequentially sweeping across 10 electrodes. (e) Microbubbles follow the stabilizing DNA as it migrates from one electrode to the next upon switching the potential (left) and re-accumulate on the new anode (right). (f) Birefringent zones sometimes become evident when viewed through crossed polarizers. All experiments were performed using a 100 bp dsDNA ladder initially at 20 µg/mL in 50mM histidine with 10 %v/v β-mercaptoethanol, 1.8 V applied for 2.5 min. Scale: all electrodes are 50 µm wide horizontally 27

Figure 2.4 Confocal laser scanning microscopy provides a 3-D view of the electrophoretically compacted DNA layer. (a) Cross-sectional slice views of the DNA layer (100 bp dsDNA ladder labeled with YOYO-1 initially at 10 µg/mL in 50 mM histidine buffer, 1 V) before and after compaction. (b) Corresponding cross-sectional intensity profile above the electrode surface. Images were acquired using a confocal microscope (Leica) with a 10x objective (2x zoom) at 400 Hz scanning speed and ~ 2.5 μm resolution in the z-direction 29

Figure 2.5 Overview of key physiochemical mechanisms associated with macromolecular compaction and subsequent microbubble formation. Charged macromolecules are electrophoretically transported to the electrode surface where they are locally subjected to gas evolution due to water electrolysis. Oxygen is produced at the anode and hydrogen is produced at the cathode above a threshold potential of ~ 1.3 V 30

Figure 2.6 (a) Microbubble clouds are not evident below the electrolysis threshold, even though electrophoretically compacted DNA is visible when fluorescently labeled (100 bp dsDNA ladder labeled with YOYO-1 initially at 10 μg/mL in 50 mM histidine, 0.7 V). (b) Above this threshold the electrophoretically compacted DNA film acts to stabilize electrolytically produced oxygen microbubbles, generating strong reflectivity under oblique white light illumination (100 bp dsDNA ladder initially at 12 μg/mL in 10x TBE, 2.5 V). (c) The stabilizing macromolecular film resists local oversaturation so that coalescence into larger bubbles occurs more readily at the cathode (heptakis (6-O-sulfo)-β-cyclodextran initially at 100 μg/mL in 10x TBE, 3 V). (d) Oversaturation eventually sets-in at the anode under high potentials and/or at long times, rupturing the compacted film (100 bp dsDNA ladder initially at 20 μg/mL in 50 mM histidine, 1.8 V; images under reflected and transmitted light are shown at the left and right, respectively). (e) When fluorescently labeled, the ruptured DNA film is evident by a dark region on the anode flanked by bright zones on either side (100 bp dsDNA ladder labeled with YOYO-1 initially at 10 μg/mL in the supplied buffer, 1.5 V). (f) Microbubble clouds are no longer evident under either reflected (left) or transmitted (right) illumination upon addition of a reducing agent (100 bp dsDNA ladder initially at 20 μg/mL in 50 mM histidine with 0.06% w/v $Na_2S_2O_4$, 2.5 V applied for 30 min). Scale: all electrodes are 50 μm wide horizontally............................... 34

Figure 2.7 Normalized kinetic data associated with formation of microbubble layers in unlabeled DNA capture experiments (data in (a-d) correspond to plots in Figure 2.8, respectively). The resulting time constants are reported in Table 2.1. Data are shown for experiments varying (a) applied potential, (b) initial DNA concentration, (c) DNA fragment length, and (d) reducing agent concentration....................... 35

Figure 2.8 Kinetics of microbubble cloud formation. (a) Effect of applied potential (unlabeled 100 bp dsDNA ladder initially at 20 µg/mL in 50 mM histidine). (b) Effect of initial DNA concentration (unlabeled 100 bp dsDNA ladder in 50 mM histidine, 2.3 V). (c) Effect of DNA length (all samples initially at 20 µg/mL in 50 mM histidine, 2.3 V). (d) Effect of reducing agent $Na_2S_2O_4$ (unlabeled 100 bp dsDNA ladder initially at 20 µg/mL in 50 mM histidine, 2.3 V). Scale: all electrodes are 50 µm wide horizontally 37

Figure 2.9 Decreased reflectivity in the presence of a reducing agent is restored when the DNA capture process is repeatedly performed. (a) Kinetics of surface reflectivity growth in response to repeated electrode capture. (b) Corresponding images show restoration of surface reflectivity (100 bp dsDNA ladder initially at 20 µg/mL in 50mM Histidine buffer with 0.01 wt% of $Na_2S_2O_4$, 2.3 V potential)............. 38

Figure 3.1 The microdevice design incorporates a glass microchannel (275 x 45 µm cross-section) bonded to a Si substrate patterned with a Cr microelectrode array. When a 2.5 V potential is applied, the Cr electrodes electrochemically dissolve at a rate dependent on the chemical composition of the bulk solution (arrows). The dissolution process can be readily detected by observing the change in reflected light intensity from the electrode surface... 44

Figure 3.2 Effect of initial DNA concentration to chromium electrode compaction. DNA compaction experiments were performed using a 100 bp ds DNA ladder labeled with YOYO-1 in 50mM histidine at 2.5V. The initial DNA concentration is 20 µg/mL (a), 10 µg/mL (b) and 5 µg/mL (c). Scale: all electrodes are 50 µm wide horizontally ... 46

Figure 3.3 Electrode surface reflectivity unfolds differently during dissolution involving different analytes. (a) Evolution of reflected light intensity from the active electrode displays composition-dependent behavior as evident by comparing dissolution kinetics of histidine buffer (50 mM, pH 7.6), a 100 bp dsDNA ladder (20 µg mL^{-1} in 50 mM histidine), a reducing agent (0.06% w/v $Na_2S_2O_4$ in 50 mM histidine), and at low pH (50 mM histidine, pH 4.4). Results from two independent experiments are shown for each analyte to assess reproducibility. (b) The dissolution process evolves more slowly when DNA fragments of increasing length are probed (all samples prepared at 20 µg/mL in 50 mM histidine). These differences are accompanied by a transition from uniform reflectivity to the appearance of speckled zones on the dissolving electrode.................. 48

Figure 3.4 PCR products can be detected by observing electrode dissolution kinetics. (a) Accelerated dissolution kinetics are observed in the presence of the post-PCR products, as compared with the pre-reaction control. The time to reach a peak reflective intensity value before decreasing due to dissolution ($\Delta t_{\max}$) offers a convenient observable parameter that is independent of run-to-run variations in absolute reflected light intensity. Results from two independent experiments are shown for each analyte to assess reproducibility. (b) Dissolution kinetics evolve differently at intermediate cycles of the PCR, likely owing to the presence of longer non-specific products produced at early stages of the reaction, potentially providing a way to determine the onset of exponential target replication 50

Figure 3.5 The microelectrode arrays are large enough to enable dissolution to be directly imaged using an ordinary smartphone (Apple iPhone 4S). Scale: all electrodes are 50 µm wide horizontally............................... 52

Figure 3.6 Various parameters presented on the kinetics profile associated with the underlying mechanisms. (a) Data normalization to scale the reflective intensity. The slopes before (S_1) and after (S_2) the time reaching a peak intensity value simply imply the reaction rate of two electrochemical reactions, electrolysis of water and chromium dissolution, respectively. The peak time value ($t_{\max}$) and the time when the intensity crosses the x-axis (t_{cross}) are considered as the termination of these two reactions. The peak intensity value ($I_{\max}$) is regarded as oxygen production provided from hydrolysis of water. (b) Original kinetics profile from experiments presents different values of slopes before (S_1) and after (S_2) the peak time since the data normalization twists the curve (data is corresponding to plots in Figure 3.3 a) 53

Figure 3.7 Simultaneously measure the reaction current as a function of time (data is corresponding to plots in Figure 3.3). Results from two independent experiments are shown for each analyte to assess reproducibility. Trendlines (green lines) are displayed the similar behavior among all compositions. Violent fluctuation was observed with reducing agent added. All experiments were performed at a constant potential of 2.5 V 55

Figure 4.1 Microbubble dissolution kinetics based on the modified Epstein-Plesset equation. (a) Radius-time curves of a free microbubble composed of air and perfluorobutane (PFB) in a gas-saturated liguid (*f* = 1) condition. (b) Radius-time curves of lipid-coated microbubbles in degassed liguid (*f* = 0) condition 60

Figure 4.2 Typical size distributions of microbubbles prepared from a phospholipid suspension *via* sonication, coaxial electrohynamic atomization (CEHDA) and a microfluidic T-junction device 63

Figure 4.3 (a) SDS microbubbles are formed under the concentration slightly below the CMC at higher potential and longer time (10^{-1} CMC, 3 V applied for 15 min). (b) Gas filled SDS micelles are compacted at the anode under the CMC (1 CMC, 3.5 V applied for 60 s). (c) Larger bubble forms due to locally oversaturated gases coalescence at a longer time applied (1 CMC, 3.5 V applied for 5 min). (d) View of the moment of SDS microbubble formation at the concentration great than the CMC (10 CMC, 3 V applied for 20 s). (e) Discrete SDS microbubbles are produced by applying an initially higher potential then following a lower potential at the concentration above the CMC (10 CMC, 5 V applied for 15 s, then switched to 3 V applied for 30 s). (f) Large amount of discrete SDS microbubbles are produced by a low and then a higher potential applied at the concentration above the CMC (10 CMC, 3 V applied for 60 s, then switched to 5.5 V applied for 50 ms to trigger release). Scale: all electrodes are 50 μm wide horizontally 66

Figure 4.4 (a) Only weak surface reflectivity is evident at the anode when the surfactant concentration is below the CMC (2.8 V applied for 90 s). (b) Bright spots appear in the vicinity of the CMC, transforming into a dense opaque halo at higher potentials and/or longer times (top: 3 V applied for 90 s; bottom: 3.5 V applied for 60 s). (c) Discrete encapsulated microbubbles are produced at bulk concentrations above the CMC (3 V applied for 60 s for bubble formation, then switched to 5.5 V for 50 ms to trigger release). (d) Under these conditions, compacted micelles confined at the electrode surface become infused with electrochemically generated gasses. All surfactant solutions contain SDS in 50 mM histidine. Scale: all electrodes are 50 μm wide horizontally 69

Figure 4.5 (a) Illustration of the reverse micelle forming and resulting reverse micelle particle. (b) Gas filled AOT micelles clouds are apparent at cathode in the vicinity of the CMC (1 CMC, 3 V applied for 15 min). (c) Denser AOT micelles clouds show at cathode while a larger bubble forms due to locally oversaturated gases coalescence when a longer time applied with the concentration slightly above the CMC (5 CMC, 3.5 V applied for 16 min) (d) AOT aggregates is evident in the bulk solution when the concentration is far above the CMC and a halo forms while the supplied potential applied to the cathode (20 CMC, 3 V applied for 20 sec). (e) Larger non symmetrical bubbles are produced under the concentration far above the CMC for a longer time potential applied (20 CMC, 3 V applied for 10 min). (f) Discrete uniform microbubbles are produced at a high viscosity solution prepared from glycerol and high concentration of SDS (30% glycerol and 40 CMC of SDS, 3.3 V applied for 150 s, then switched to 2.5 V applied for 30 s). Scale: all electrodes are 50 μm wide horizontally.. 71

Figure 5.1 Simplified phase diagram for protein crystallization. Adjustable parameters include precipitant or additive concentration, pH and temperature. The overview of traditional crystallization methods is represented: (i) microbatch, (ii) vapor diffusion, (iii) dialysis and (iv) free interface diffusion. Each involves a different route to reach the nucleation and metastable zones, and all require long timescales (days to weeks).. 77

Figure 5.2 Experimental set-ups of a crystallization cell using an external and an internal electrical field, respectively. For the external-electrical-field-setting, the electrodes are not in contact with the solution containing the interested proteins. On the contrary, the electrodes are directly in contact with a protein solution, called internal-electrical-field-setting.. 79

Figure 5.3 (a) Microelectrode array constructed using an optically transparent 40 nm gold film that permits the electrode compaction process to be observed using polarizing optical microscopy. Birefringent textures become evident when captured DNA is viewed under crossed polarizers – a clear signature of ordered phase formation. (b) 3-D confocal image of multi-dimensional compaction of dsDNA labeled with YOYO-1 after sweeping across 7 electrodes. To determine the thickness of the accumulated molecules layer and its distribution over electrode surface to obtain cross-section slice view of the captured molecules in the vicinity of the electrode surface. 80

Figure 5.4 Preliminary results demonstrating feasibility of forming lysozyme single crystals by electrokinetic actuation. Within one minute after application of a 2 V potential between electrodes, a dense ultra-compacted protein layer becomes evident surrounding the capture electrode. The densely packed protein within this "halo" are then released when the voltage is switched off, and the resulting compacted front returns to equilibrium ionic conditions while remaining in a supersaturated state for nucleation of crystallization.

Large single crystals are formed within 1-2 hours. Scale: all electrodes are 50 µm wide horizontally 83

Figure 6.1 Illustration of microdevice construction and microfabricated electrode arrays 84

Figure 6.2 (a-b) Cross-sectional view of two-layer PDMS membrane valve. The valve is operated as closed when a positive pressure provided (a) and open when a negative pressure provided (b) (1: silicon substrate; 2: PDMS pneumatic layer; 3: PDMS microfludic channel; 4: displacement chamber). (c) Schematic diagram of micropump. The pumping involves cycles of three steps: open input valve and close diaphragm and output valves; open diaphragm valve and close input and output valves; open output valve and close input and diaphragm valves. (d) Schematic diagram of three microvalves and microfludic channel (i: buffer inlet; ii: buffer outlet; iii: sample injection; iv: electrode array; v: microvalves) 88

Figure 6.3 Illustration of acrylic clip and microdevice construction 89

Figure 6.4 Preliminarily results demonstrating the performance of the micropump operation. Experiments were performed using a 100 bp dsDNA ladder initially at 10 µg/mL in 50 mM histidine with 10 %v/v β-mercaptoethanol, 2.0 V applied to capture the hydrodynamic flow DNA samples. The flow was setting from right to left on the diagram. Captured DNA samples wash away slowly with the increase of the flowrate based on the observation of the intensity decreasing. Scale: all electrodes are 50 µm wide horizontally 89

LIST OF TABLES

Page

Table 1.1 Variety of samples for diagnostics 3

Table 1.2 The important analytical procedure for the routine determination of analytes 8

Table 1.3 Examples POC NAT platforms that that are commercially available or close to market 16

Table 2.1 Time constants τ associated with evolution of microbubble clouds in DNA capture experiments, obtained by fitting the kinetic data to a single-parameter exponential equation: $y = 1 - \exp(-t/\tau)$. All experiments were performed at a potential of 2.3 V, except for the data where the applied potential was varied....................................... 37

Table 3.1 Normalized kinetics parameters associated with two electrochemical reactions, electrolysis of water and chromium dissolution, in unlabeled DNA detection experiments. All experiments were performed at a potential of 2.5 V and data is corresponding to plots in Figure 3.3 a... 54

Table 4.1 Comparison of microbubble yields obtained from different microfluidic technologies 63

CHAPTER I

INTRODUCTION

Incredible advances have been made toward the development of microfluidic systems capable of performing a wide range of chemical and biochemical analysis operations. This progress has been driven by the compelling benefits of miniaturization, including reduced reagent consumption and an increased capacity for automation so that the costs of performing reactions can be dramatically lowered. However, the necessity for high-performance and rapid capabilities micrototal-analysis-systems (μ-TAS) and lab-on-a-chip devices to operate in hospitals and emergency treatment in ambulances or disaster sites has never been more relevant. Thus, developing high-speed, high-resolution, portable bio-analysis devices which can be immediately used at the point-of-care (POC), homebased and field-based assays becomes a very important research topic.

1.1 Microfluidics Meets Requirements of Point-of-Care Applications

Considering the features of microfluidics, including low consumption of reagents and sample, miniaturization of device, and fast turnaround time for analysis, it is a nature fit for a POC diagnostics device, which performs at near-patient testing in a hospital, doctor's office, clinic, or home without the use of laboratory staff and facilities to receive the result in seconds to hours[1]. Thus, there is no surprise that a growing research has focused on microfluidic-baesd application in POC sensors and diagnostics (Figure 1.1). The diagnostic samples for POC testing can be blood, saliva, urine, or other bodily fluids or solids, and the targets include proteins, nucleic acids, metabolites, dissolved ions, microbes and so on[2]. Table 1.1 shows a variety of liquid samples from body fluids may be routinely analyzed in POC testing[3].

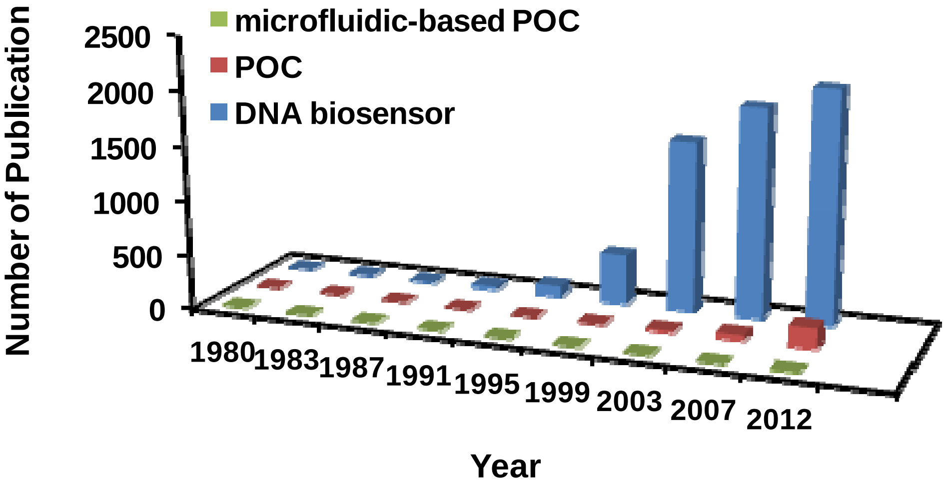

Figure 1.1 Annual trends in the number of publication for microfluidic-based point-of-care, point-of-care, and DNA biosensor. The terms "microfluidic point of care detection*", "point of care diagnostic*", "point of care detection*", "gene array*", "gene chip*", "DNA biosensor*", "DNA array*", "DNA sensor*", "genosensor*", "DNA biochip*", "DNA chip*", "DNA microarry*" have been considered. The literature search was done using ISI's Web of Science (http://www.isiknowledge.com), accessed October 2012.

Table 1.1 Variety of samples for diagnostics[3].

sample	Relevant composition	Typical tests
Blood	45% hematocrit: erythrocytes, reticulocytes, platelets, leukocytes 55% plasma	Blood typing, genetic, cardiovascular, metabolism, infectious disease, cancer, drug and hormone monitoring
Plasma	Albumin, globulins, clotting factors, hormones, glucose and ions	Genetic, cardiovascular, metabolism, infectious disease, cancer, drug and hormone monitoring
Saliva	Proteins, nucleic acids, proteolytic enzymes, enzymes from bacteria, bacteria	Mostly qualitative: genetic, cardiovascular, metabolism, infectious disease, cancer, drug and hormone monitoring
Urine	Metabolites, ions Abnormal: protein, blood cells, pathogens	Metabolism, liver, kidney, pregnancy, drug and hormone monitoring
Stool	Bacteria, fiber, cells Abnormal: blood, undigested nutrients	Digestive tract diseases (liver, pancreas, colon), parasites, infectious disease
Amniotic, cerebrospinal, lymphatic fluid	Cells, proteins and nucleic acids Abnormal: pathogens	Genetic mutations, infectious disease, metabolism
Liquid from puncture of lung, pleura, ascites (abdomen) or joint	Cells, proteins and nucleic acids	Cardiovascular, pulmonary, infectious disease, cancer

1.1.1 Essentials of Idealized Microfluidic-Based POC Device

The easier successful POC tests for diagnosis involve the lateral flow tests, which require only addition of sample, and are well known as pregnancy test and widely used to human immunodeficiency virus (HIV) diagnosis in developing countries. Although these tests are simple to perform by untrained people, the analysis does not mimic the multi-steps handling in laboratory-based procedures, which raises a consideration of producing highly reproducible, quantitative, and sensitive results[4]. Another well known successful POC test is the blood glucose test, which has improved diabetic patients' lives and occupied most of the diagnostics market. However, the glucose test is based on a unique biochemical reaction and the concentration of the analytes is in the mM rang, which is far exceeds the concentration of most diagnostics markers[4]. Therefore, a microfluidic-based device, which can achieve real clinical requirements and detect low concentration of targets with an ability of quantify, will open a new page for the next generation of POC testing in healthcare. Figure 1.2 displays an idealized concept of a microfluidic-based POC device, which is challenged by small sample volumes (hundreds of nanoliters to ~1 mL) and conducts complex biological media with femtomolar to millimolar concentration of analytes[3].

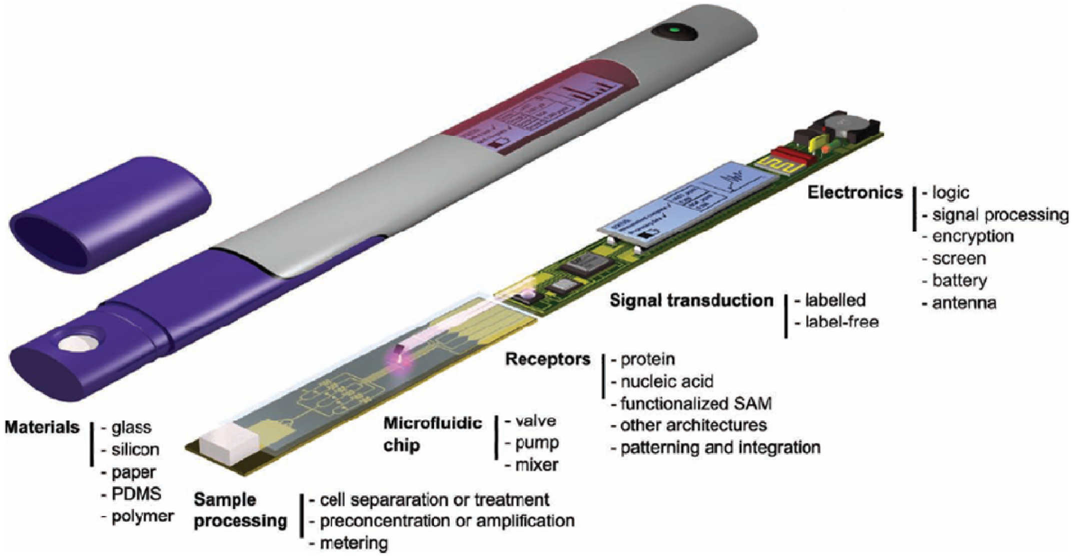

Figure 1.2 The ideal POC diagnostic device, which can quantitatively detect several analytes, within minutes, at femtomolar sensitivity from 1 μL of bodily fluid and report the result. This ideal device is disposable and the mass manufacturing material cost would be less than $1. It does not exist now but the research progress in microfluidics and material science point toward the realization of such a POC device in the near future[3]. Copyright 2011 John Wiley & Sons, Inc.

1.1.2 Challenges of Microfluidic-Based POC Applications

Overview of the features of microfluidics, they do have huge potential to benefit POC testing in the future. Nevertheless, the requirements of POC diagnostics still present several new challenges for microfluidic-based POC applications. For instance, detecting target analytes with high sensitivity and selectivity is a major challenge due to the ultra-small sample volumes[5]. Moreover, the tests need to be cheap, rapid and simple to use. Preferably, the whole assay covers sample taking until the read-out of the results without any additional handling by the user[6]. Thus, another important challenge is to integrate the varied microfluidic technologies into a single disposable platform, which means the peripheral equipment (microscopes, pumps, readers, etc.) has to be merged for processing and analyzing a sample, and reporting the results on a chip. In addition, the size and the weight of the devices, as well as the energy consumption, need to be minimized for the portability. Typically, microfluidic devices require manufacturing processes that are expensive and non-scaleable. Therefore, using inexpensive materials (e.g., paper[7]), low-cost manufacturing and packing methods, and pervasive detection device (e.g., cameras from consumer electronics[8, 9]) to get the diagnostics out of the laboratories are the new trends in the future.

Summarily, the future trends and technologies for the microfluidic-based POC devices include three main ways:

- *New materials*, to reduce cost and complement the current focus on planar microfluidics. (e.g., paper as substrate, materials that enable autonomous)
- *New detection strategies* (e.g., label-free detection)
- *New applications* (e.g., investment in $1000 whole-genome sequencing may accelerate the development of POC molecular testing)[10]

1.2 Strategies for Detection of Biomolecules in Microfluidic Systems

There are over 6000 experimental procedures available with subspecifications for medicinal laboratory diagnostics[11]. The testing materials are very diverse and depending upon its origin and nature, which have been showed in Table 1.1. The most important methods have been selected and listed in Table 1.2. Opportunely, a number of approaches have been investigated to perform biomolecules detection in microfluidic systems[12, 13], which can be classified into several major types: optical methods[14-22], electrochemical methods[23-27], mass spectrometry (MS) methods[28, 29], nuclear magnetic resonance (NMR) spectroscopy[30], magnetoresistive[31], and acoustical[32]. In regard to the selectivity and sensitivity, optical and electrochemical methods are the most frequently utilized.

1.2.1 Optically-Based Technologies

Among these methods, optically-based technologies are the most mature and popular methods, which can be broadly categorized into two groups, namely labeled methods and label-free methods. In labeled methods, biomolecules (e.g., DNA or proteins) are detected by fluorescent labeling, which has been largely used in optically-based study of molecular interactions. But these approaches are also subject to important drawbacks including the additional time and expense required to perform chemical labeling, and the possibility that fluorescent tags may render the biomolecules incompatible with subsequent reactions[33]. Another important drawback is that sensitive macro-scale optical detection instrumentation is typically needed because the levels of emitted fluorescence are inherently low. The size, complexity, and cost of these components can negate many of the benefits of miniaturization.

Table 1.2 The important analytical procedure for the routine determination of analytes.[11]

Spectrometry	***Electrophoresis***
• absorption spectroscopy/photometry • UV/Vis/NIR/IR spectroscopy • atomic absorptions spectroscopy (AAS) • atomic fluorescence spectroscopy (AFS) • NMR spectroscopy • luminescence spectroscopy: bioluminescence measurement, chemiluminescence, fluorescence, time-resolved fluorescence, fluorescence polarization and phosphorescence spectroscopy • nephelometry/ immunonephelometry • turbidimetry/ immunoturbidimetry • atomic emission spectroscopy (AES) • flame emission spektroscopy • ICP mass spectrometry (ICP-MS), MALDI-TOF-MS	• zone electrophoresiscellulose acetate; electrophoresis • immunoelectrophoresis/ immunofixation • isoelectric focusing • pulse-field gel electrophoresis • counterimmune electrophoresis (countercurrent electrophoresis) • isotachophoresis • capillary electrophoresis • rocket electrophoresis
Ligand Assays	***Electrochemical Studies***
• enzyme immunoassay • fluorescence immunoassay • immunoblot (Western blot) • luminescence and electrochemiluminescence immunoassay (CLIA/ECLIA) • fluorescence polarization enzyme immunoassay • radioimmunoassay • receptor assay	• amperometry: O_2 partial pressure (Clark electrode) • potentiometry: pH value, CO_2 partial pressure, ion-selective electrodes • coulometry • voltammetry
Chromatography	***Molecular Biological Methods***
• thin-layer chromatography (TLC) • liquid chromatography (LC) • gas chromatography (GC) and GC-MS • high-performance liquid chromatography (HPLC) and HPLC-MS	• (real-time) polymerase chain reaction • Southern blot • fluorescence in situ hybridization (FISH) • evidence for single-nucleotide polymorphisms (SNPs) with, e.g. restriction fragment length polymorphisms (RFLPs), FRET probes (FRET: fluorescence resonance energy transfer), density gradient gel electrophoresis (DGGE), denaturing HPLC (DHPLC)

As a result of the above drawbacks of labeled technologies, researches have been exploring the area of label-free detection to overcome these problems, including autofluorescence[16], confocal Raman spectroscopy[19], intracavity spectroscopy[20], optical scattering[15] and surface plasmon resonance (SPR)[34, 35]. However, most of these techniques have been developed for biophysical studies, which are hindered by the bulky and expensive equipment needed, and limited cell and biomolecule manipulation. Electrochemical detection is also explored as label-free alternative because of the capability of providing direct electrical output signals based on amperometry[23, 24], conductimetry[25, 26], and potentiometry[27]. Also, electrochemical detection is highly amenable to miniaturization, which has been demonstrated for detection of analytes during capillary electrophoresis[36] as well as for sensing of hybridization at functionalized electrode surfaces[37]. Although electrochemical detection can be applied to detect charged molecules, detection of DNA in free solution still requires addition of electrochemically active intercalation agents and is not particularly sensitive to low DNA concentrations[13, 38].

The typical optical detection methods involve the detection by directly monitoring the light properties, including fluorescence[18, 39, 40], absorbance[21], and luminescence[22], and the light property modulation such as surface plasmon resonance (SPR)[34, 35], which have been demonstrated in Figure 1.3. Although SPR techniques have been widely used for detection of binding events at surfaces, they are generally unable to apply for analysis of species in free solution. As for the electrochemical measurements, the principles have been demonstrated in Figure 1.4, which are based on the electrical property modulations of the analyte species that undergo redox reactions and are usually employed for the detection of the eletroactive species[41].

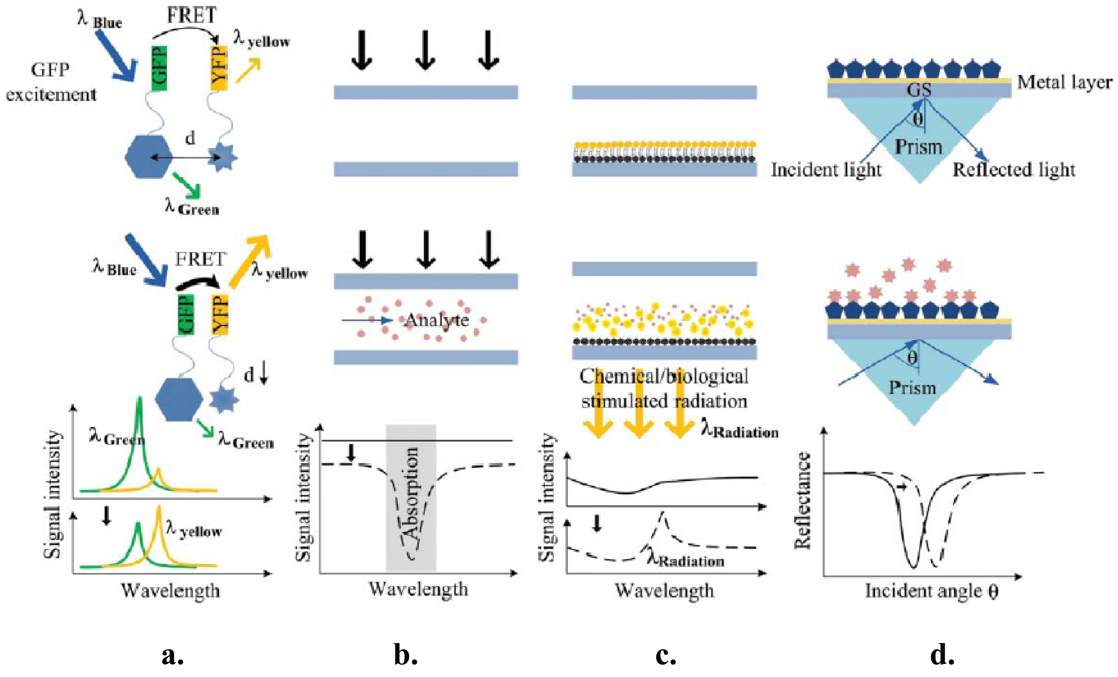

Figure 1.3 The typical optical detection methods. (a) Fluorescence (in this case, fluorescent resonance energy transfer/FRET), (b) absorbance, (c) luminescence, and (d) surface plasmon resonance (SPR)-based optical detection methods. GFP: green fluorescent protein; YFP: yellow fluorescent protein; GS: glass substrate.[41] Copyright 2011 SPIE.

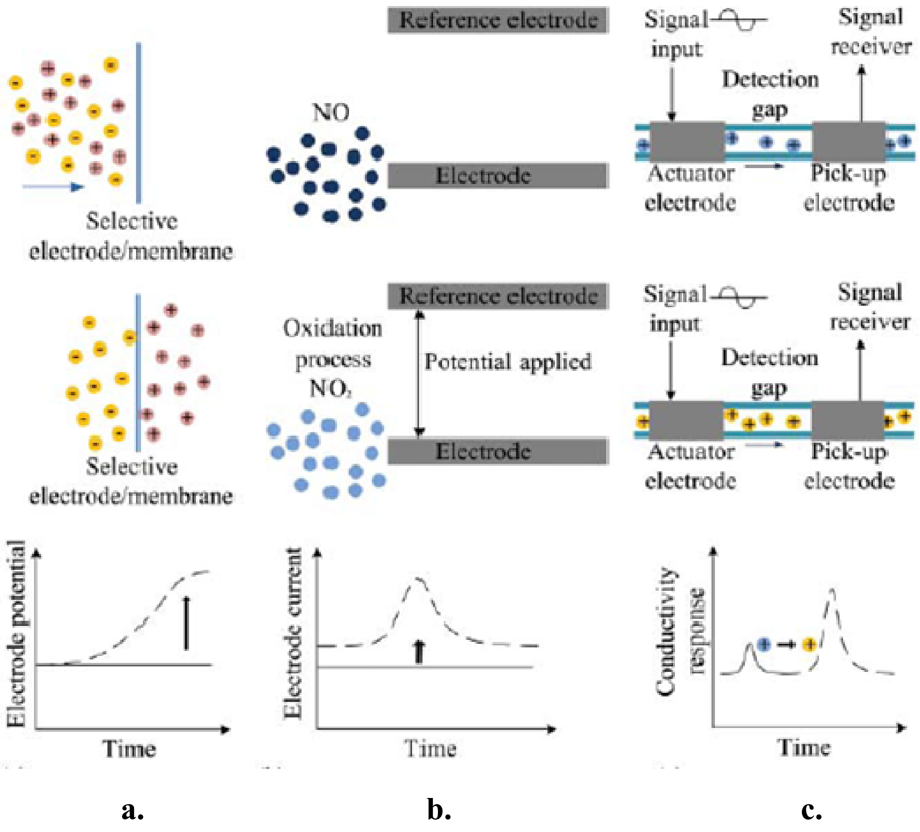

Figure 1.4 The typical electrochemical detection methods for microfluidics: (a) amperometric, (b) potentiometric, and (c) conductometic (capacitively coupled conductivity detector) detection.[41] Copyright 2011 SPIE.

1.2.2 Mass Spectrometry Related Technologies

Detection methods based on mass spectrometry (MS) also show great promise[42] to perform highly selective detection by monitoring ions in electric and/or magnetic fields. The most important application for MS detection is in proteomic studies for protein separation and further identification from the fragmentation. However, a major challenge remains to be overcome before all the associated instrumentation can be fully miniaturized and integrated with other microfluidic components. Roukes's group[29] in

Caltech developed a nanoelectromechanical system-based MS (NEMS-MS), which could be realized to analyze biological or chemical species (e.g., proteins or nanoparticles) at a single molecular level with the ability to operate in multiplexing and parallel modes (Figure 1.5). It can be expected to meet the microfluidics' demands in the future.

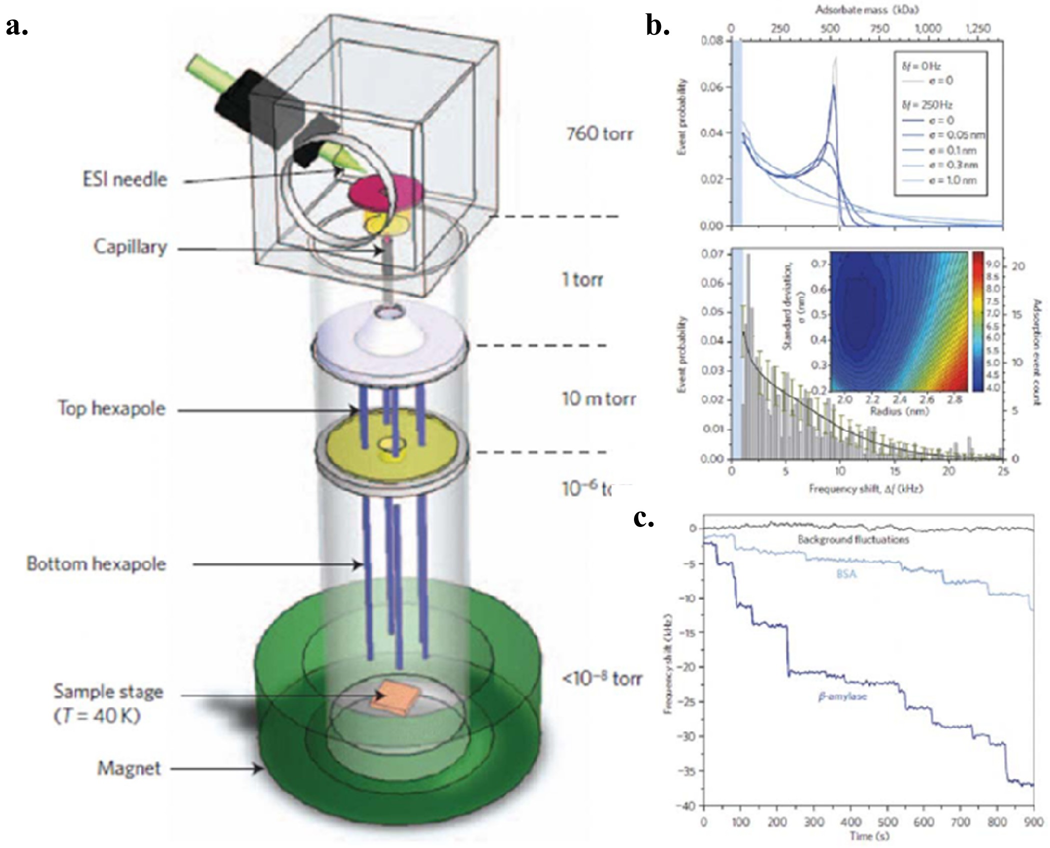

Figure 1.5 Nanoelectromechanical system-based MS (NEMS-MS) developed by Roukes's group in Caltech. (a) the simplified schematic of the experimental configuration for first-generation NEMS-MS system, (b) the NEMS mass spectrometry of a gold nanoparticle dispersion, and (c) real-time records of single-molecule adsorption events on a NEMS mass sensor from their experiments.[29] Copyright 2009 Macmillan Publishers.

1.3 Current Technologies and Challenges of Nucleic Acid Testing for Microfluidic-Based Point-of-Care Applications

Researches for microfluidic-based POC devices are still emerging; particularly, there is an increasing clinical demand in high-throughput deoxyribonucleic acid (DNA) detection to assist monitor and diagnostics at the POC testing. Thus, we can see a tremendously growing research on the DNA biosensors over the past ten years as demonstrated by the large number of scientific publications (Figure 1.1). However, most of the available POC devices on the market are based on immunoassays. The Cepheid GeneXpert, a polymerase chain reaction (PCR)-based system, is currently the only moderate complexity nucleic acid testing (NAT) platform approved in the USA, but the system is still relatively expensive and complex that is still inappropriate for POC setting and can only be used in hospital[43]. Compared to equivalent laboratory tests, the POC testing is usually more expensive per test, although a true cost comparison needs to consider central laboratory overhead costs, better management, and disease containment[44]. Undeniably, nevertheless, POC NAT still provides much needed in the developing countries, which have limited financial resources, for example, the efforts are underway on HIV, tuberculosis (TB)[45-47], and enteric diseases[48]. For the developed countries, POC NAT provides a more personalized healthcare for immediate clinical management decisions that can ensure optimal use of medical resource. Additionally, Gascoyne *et al.*[49] compared different methods for Malaria detection and pointed out the genetic detection methods would offer significant advantages if they would be implemented in a μ-TAS format.

1.3.1 Demands of Microfluidic-Based POC NAT Applications

We expect POC NAT can provide much-needed diagnostic methods in low-resource, high disease-burden areas, but it has not been found widespread use in the world and a complete μ-TAS platform has not been successfully commercialized yet. The main reason is the requirement of a comprehensive tool-chain (e.g., PCR, electrophoresis, and fluorescence reader) and some case need high cost of integrated tools hybridization assays[5]. Thus, the greatest challenge for microfluidic-based POC NAT applications is combination of the principal NAT steps, sample preparation, amplification, and detection which usually use high-end instrumentation and skilled personnel, into one integrated and automated system. Table 1.3 listed examples of fully or partially integrated platforms that are commercially available or close to market[43, 50], but the time to result still needs ~1-2 hours and the formats are still laboratory-based NAT, close to the benchtop system (Figure 1.6).

1.3.2 Sample Preparation Is the Key

In general, sample preparation is a bottleneck in NAT, especially for microfluidic-based POC application[50], because it involves lengthy and varied processes that are often manually performed. For example, lysis needs to be performed by chemical or enzymatic means, and some microorganisms are very difficult to lyse. Meanwhile, nucleic acid purification is a necessary step because the subsequent target amplification using PCR can be inhibited by compounds found in clinic samples or ions added from lysis. Thus, sample preparation is very complicated to be integrated into an inexpensive, automated, miniaturized, and closed system format.

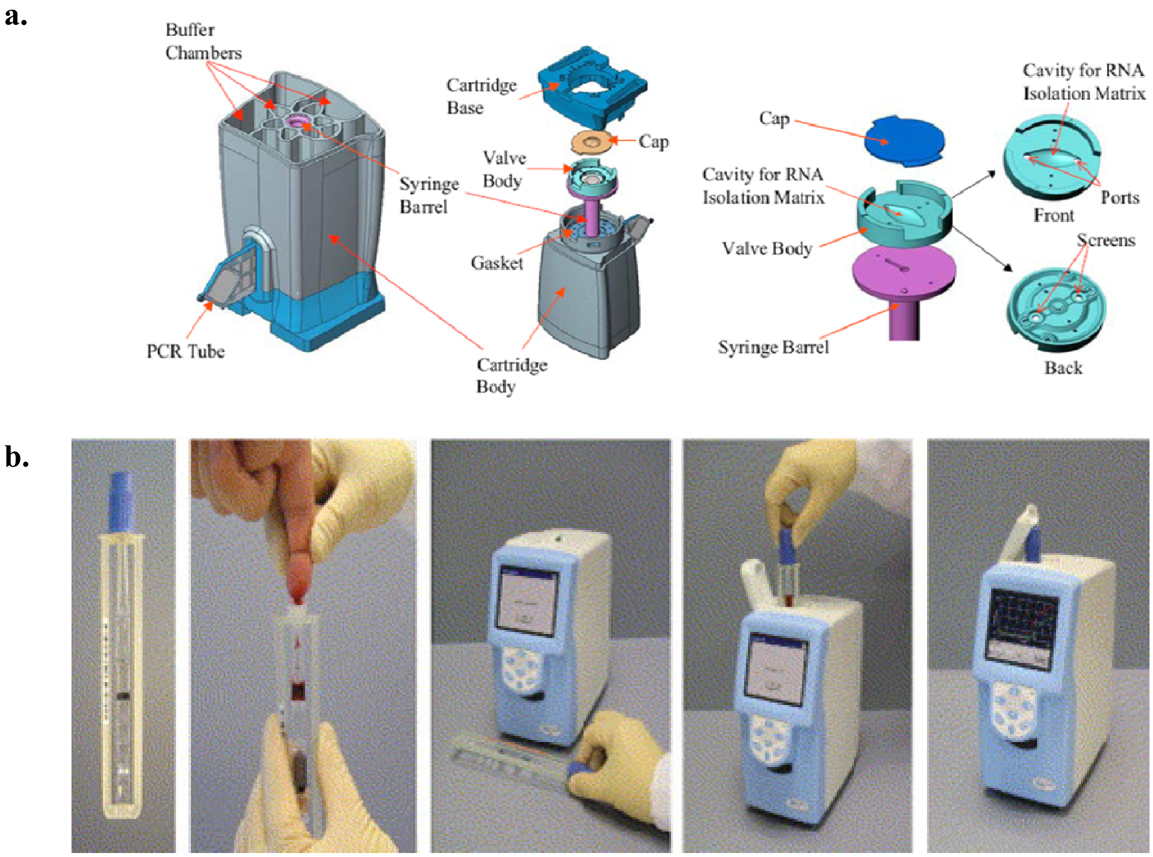

Figure 1.6 Selected technologies for POC NAT. (a) Detailed schematic of Cepheid's GeneXpert cartridge, nucleic acid purification valve body, and cartridge valve body[51]. Copyright 2005 American Association for Clinical Chemistry. (b) Detail of Liat Analyzer operation. The analyzer can automatically perform the nucleic acid testing steps and report results within 1 h from a sample such as whole blood[52]. Copyright 2010 Infectious Diseases Society of America.

Table 1.3 Examples POC NAT platforms that that are commercially available or close to market[43, 50].

Platform	**Manufacturer**	**Integrated Sample Preparation**	**Amplification**	**Detection**[a]	**Time to Result**[b] **(min)**	**Website**
GeneXpert	Cepheid	Yes	Real-time PCR	RTF	<120	http://www.cepheid.com/
Liat Analyzer	IQuum	Yes	Real-time PCR	RTF	<60	http://www.iquum.com/
FL/ML	Enigma	Yes	Real-time PCR	RTF	<45	http://www.enigmadiagnostics.com/
LA-200	Eiken	No	Loop-mediated amplification (LAMP)	RTT	<60	http://www.eiken.co.jp/
Twista	TwistDX	No	Recombinase polymerase amplification (RPA)	RTF	<20	http://www.twistdx.co.uk/
BART	Lumora	No	Loop-mediated amplification (LAMP)	RTB	<60	http://www.lumora.co.uk/
Genie II	Optigene	No	Loop-mediated amplification (LAMP)	RTF	<20	http://www.optigene.co.uk/

[a] RTB: real-time bioluminescence; RTF: real-time fluorescence; RTT: real-time turbidimetry
[b] Time to result depends upon the particular assay. Longer times may be required for assays with a reverse transcriptase step

1.3.3 Concentration Desires to Be Improved

Although microfluidic technologies have enabled increasingly sophisticated biosensing operations to be performed at the microscale, most infectious disease applications still require extraction and concentration of target nucleic acids from samples to reach a suitably low limit of detection (LOD). Concentration process is typically accomplished by either physical processes (e.g., centrifugation) or chemical amplification (e.g., PCR). Centrifugation is generally difficult to miniaturize and interface with microfluidic components, while techniques like PCR are not straightforward to apply when the sample of interest contains multiple components or is unknown. Moreover, the reaction products contain enzymes, primer oligonucleotides, and other chemical species, which are unique and expensive, in addition to the target nucleic acid often making it is necessary to incorporate additional purification steps prior to subsequent analysis. Thus, recent efforts have focus on technologies that allow a lower LOD[53], reduce the number of PCR cycles or even relax the need of a PCR step completely[54].

1.3.4 Detection System Needs to Be Merged and Minimized

Nucleic acid amplification can be analyzed after the reaction (endpoint detection) or while the reaction is progressing (real-time detection), but both of them relay on fluorescence detection, which requires optical excitation, involving gas lasers or high power broadband source and it is very difficult to merge into a microfluidic platform as mentioned earlier before. Most current POC NAT platforms are based on real-time fluorescence detection (Table 1.3), which requires relatively expensive and complex instrumentation, but superior for quantitative analyte detection. Recent studies have focused on label-free technologies by replacing the readout of fluorescence intensity with electrical readout. However, most label-free detection technologies involve the nucleic acid immobilization based on surface charge change[55] or diameter change[56] after DNA hybridization or direct detection of DNA hybridization on Metal-Oxide-Semiconductor Field Effect Transistor (MOSFET) gate[57]. Those methods need relatively high-cost manufacturing and packing and suffer from the changes must not be screened by the solution. For example, the limits of the salt concentration in solution to values of 0.005x phosphate buffer saline (PBS) which is significantly below the physiological concentration[5] that it is impossible to meet the clinic demands. Thus, developing quantitatively detect label-free nucleic acid in free solution would introduce new opportunities to greatly simplify the physical and operational design of integrated μ-TAS platforms. These capabilities also have the potential to enable the progress of on-chip processes to be observed and regulated in real-time.

1.4 Motivation and Objectives

POC NAT is still in the emerging stage, in particular of the microfluidic-based methods. Figure 1.2 has been demonstrated the ideal microfluidic POC device, in fact, the imagined ideal POC device does not exist at this moment but crystallizing a vision to help us identifying the desirable characteristics of the requirements on progress in the field of microfluidic POC. Although no method is clearly superior and most technologies are still at the laboratory-based research stage, there is a strong demand of a cheap, rapid and simple to use POC diagnostics device for the coming future. Generally, microfluidic devices are often first developed in research laboratories by integrating complex concepts into a single device, and then following the original prototype to simplify the technology while preserving its performance. Many promising technologies are still at the early research stage and will need fundamental innovations before clinical use, nevertheless, there will be always potential to move beyond benchtop-based approaches towards small POC handheld devices. Before that day coming, we still have a lot of work to do.

In this study, we will focus on seeking new detection strategies (label-free detection) and new applications (encapsulated microbubble synthesis, protein crystallization) based on a versatile microfabricated electrode arrays and try to get the diagnostics method out of the laboratory (using pervasive smartphone optics). The specific objectives are as follows:

- **Develop a microfluidic platform for label-free detecting charged molecules in free solution by using a simple device design and minimal electrical power.** We used unlabeled DNA as the beginning target to make it possible for detecting under very small potentials (1-3 V). The fundamental studies of the phenomena include several parameters, applied potential, initial DNA concentration, DNA length and amount of reducing agent, to verify the mechanism and determine optimum operation condition. Furthermore, we applied this method to detect protein and small -molecule cyclodextrans as well (Chapter II).

- **Build a novel unlabeled detection method based on the electrochemical reaction by using the microfabricated chromium electrode arrays with smartphone optics.** We used chromium as the studying material to fabricated microelectrode arrays. Since chromium is highly reactive and may unintentionally participate in the electrochemical reaction[58], we propose to harness this reactivity as the basis of a new detection method whereby the rate of electrode degradation is monitored and correlated with compositions of the bulk solution. The fundamental parameters to be studied including reducing agent amount, initial DNA concentration, DNA length, and buffer solution type to establish the sensitivity and detection limits. Furthermore, we applied this novel approach combine with smartphone optics to create an opportunity for a lighter weight telemedicine interfaces for a near-POC NAT application. (Chapter III).

- **Apply the DNA label-free detection methodology and hardware to establish a new application for synthesizing encapsulated microbubbles.** We apply the above DNA label-free detection method in the presence of surfactants instead of DNA to make it possible to produce discrete stabilized microbubbles. The surfactants include anionic surfactant sodium dodecyl sulfate (SDS) and cationic surfactant dioctyl sodium sulfosuccinate (AOT) under different critical micelle concentration (CMC) to establish optimal conditions and the governing parameters include electric field (amplitude, frequency, etc), buffer (type, concentration), and viscosity of bulk solution to enable production of microbubble of controlled size (Chapter IV).

- **Exploit an innovative application for protein crystallization by using the on-chip microfabricated electrode arrays.** We used hen egg white lysozyme as a model protein to explore the capability of a fast and easy strategy for on-chip protein crystallization *via* electrokinetic actuation. The aim of this study is to investigate a technique for shorter induction times of the nucleation and for production of larger enough crystals for subsequent structural analysis (Chapter V).

CHAPTER II

A MICROFLUIDIC PLATFORM FOR PRE-CONCENTRATION AND LABEL-FREE DETECTION OF DNA BY USING ON-CHIP ELECTRODE ARRAYS[*]

This chapter details a new technique we developed that can enable biomolecules (DNA, proteins) and other charged analytes to be detected in free solution without the need for conventional labeling with conjugated chemical fluorophores *via* a simple device design that consumes minimal electrical power. We used DNA as a probe to study the morphology of the compacted macromolecular film and the kinetic mechanism to determine optimum conditions. Using this arrangement, we have shown that it is possible to detect a variety of analytes in free solution by simply illuminating the electrode surface with white light and observing the accompanying strong increase in reflected intensity.

2.1 A New Label-Free Detection Approach Performed in Free Solution

We proposed exploratory research to develop an electrokinetically actuated microbubble synthesis method that addresses the need of label-free detection by establishing localized zones inside a microchannel network where a charged biomolecule can become enriched to a very high concentration while simultaneously

---

[*] Part of the data reported in this chapter is reprinted with permission from: Tunable Synthesis of Encapsulated Microbubbles by Coupled Electrophoretic Stabilization and Electrochemical Inflation by Huang, Y.-W., Shaikh, F.A., Ugaz, V. M., *Angewandte Chemie (International Edition)*, **2011**, 50, 3739-3743. Copyright [2011] by John Wiley & Sons.

experiencing infusion with electrochemically generated gasses. The cornerstone of our approach is a microfluidic system incorporating arrays of individually addressable electrodes (patterned along the microchannel floor) that make it possible to transport charged macromolecules from the bulk solution to an electrode surface where they become compacted into an ultra-thin film (Figure 2.1 a)[59]. The compaction process is illustrated by observing the behavior of fluorescently labeled DNA in response to a 1 V DC potential applied across neighboring electrodes. The negatively charged DNA contained between active electrodes migrates toward the anode and experiences local enrichment, yielding a fluorescent zone at the electrode surface (Figure 2.1 b). Remarkably, we discovered that this compacted film can also be clearly seen under ordinary white light even when the DNA sample is unlabeled, with no excitation or emission filters in the optical path, which provide an opportunity for label-free detection (Figure 2.1 c).

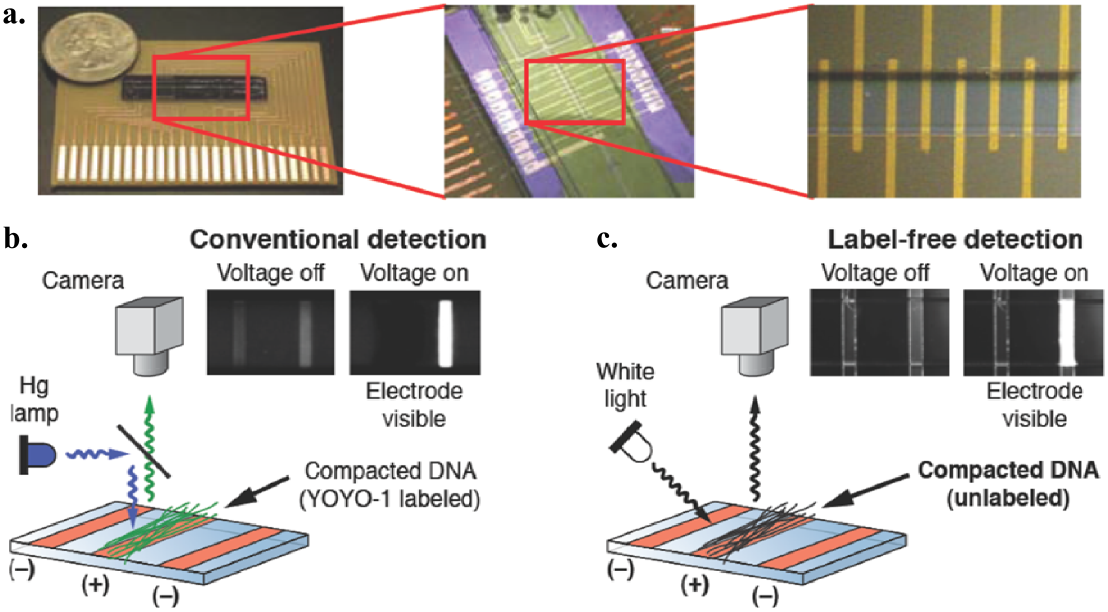

Figure 2.1 (a) Microdevice design incorporating a glass microchannel (275 x 45 μm cross-section) bonded to a Si substrate patterned with an Pt microelectrode array (50 μm wide, 250 μm edge-to-edge spacing). (b) Compaction of DNA fluorescently labeled with YOYO-1 dye yields a bright zone at the anode upon application of 1-2 V. (c) At higher potentials (2.5 V), the same arrangement enables detection of unlabeled DNA under oblique white light illumination.

We have demonstrated this microfluidic system as abovementioned, which can establish a highly concentrated and compacted DNA film at the electrode surface and can be seen under ordinary white light even when the sample are unlabeled. This phenomenon is possible due to the closely spaced electrodes within the array enable electric fields to be generated that are strong enough (50-100 V/cm) to confine the DNA sample within a very narrow layer at the electrode surface by applying very low potentials (~ 1-2 V). In this way, the biomolecules experience multi-dimensional focusing and compaction into an ultra-concentrated layer only a few microns thick.

Therefore, an anomalous highly reflective zone is formed at the electrode surface that is most clearly evident under oblique illumination, becoming visible within 10 – 20 s and completely dissipating within 5 – 10 s after the voltage is switched off (Fig. 2a-d). This unexpected phenomenon can be widely applied to detect a variety of unlabeled macromolecules including proteins (Figure 2.2 e-g) and small-molecule cyclodextrans (Figure 2.2 h). The effect can be tuned to localize compaction at either the anode or cathode by adjusting the buffer pH relative to the sample's isoelectric point (Figure 2.2 f). Thus, the unexpected phenomenon enables a label-free technique for detecting charged biomolecules.

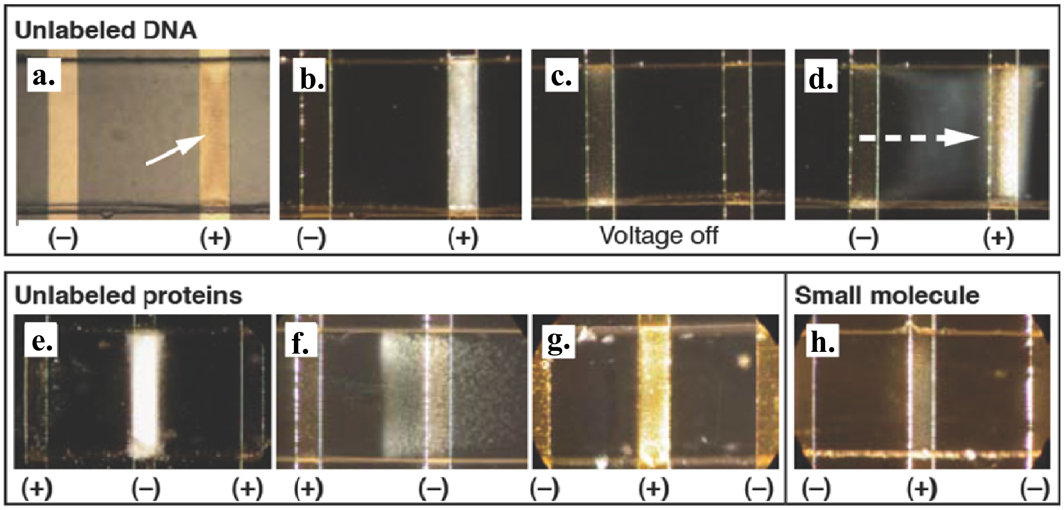

Figure 2.2 (a-d) Label-free detection of a 100 bp dsDNA ladder sample initially at 12 μg/mL in 1x TBE, 2.5V. The compacted DNA layer appears as (a) a dark zone when illuminated from above, and (b) a brightly reflective zone when illuminated from the side. (c) The reflective zone dissipates within 5-10 s after the potential is removed, and (d) can be transported between neighboring electrodes upon switching the potential. (e-h) Similar reflectivity is observed with proteins. Unlabeled egg white lysozyme (initially at 10 mg/mL in 1x TBE, 2.5 V) becomes visible within 10-20 s either (e) at the cathode, pH = 8, or (f) at the anode, pH = 11. (g) Unlabeled prostate specific antigen (initially at 0.1 mg/mL in PBS at pH = 7.2, 2.5 V). (h) Label-free detection of heptakis (6-O-sulfo)-β-cyclodextran (MW = 1,849 Da) initially at 100 μg/mL in 1x TBE, 3 V. Scale: all electrodes are 50 μm wide horizontally.

2.2 Morphological Characteristics of the Compacted DNA Layer

To determine the morphology of the compacted macromolecular films, we repeated the above mentioned DNA capture experiments under transmitted illumination using optically transparent thin gold electrode arrays. We observed the process under polarized light which reveals dense stabilized microbubble clouds are embedded within the enriched DNA zones (Figure 2.3 a). These clouds emerge because the compacted macromolecular film imposes a barrier against transport of electrochemically generated gasses produced by hydrolysis, introducing a highly reflective topology that makes label-free detection possible. The microbubble clouds are spatially distributed such that their density is greatest near the microchannel sidewalls (Figure 2.3 b) or corners of electrodes that do not span the entire microchannel width (Figure 2.3 c, d) suggesting higher levels of DNA enrichment at these locations, likely owing to the steeper electric field gradients present there. Upon switching the potential to an adjacent electrode pair, the reflective zone remains largely intact as it migrates toward the new anode indicating that the microbubbles remain stably embedded within the enriched DNA zone (Figure 2.3 e). Birefringent textures are also sometimes evident when viewed through crossed polarizers (Figure 2.3 f), suggesting local attainment of concentrations high enough to trigger transition to an ordered mesophase[60-63].

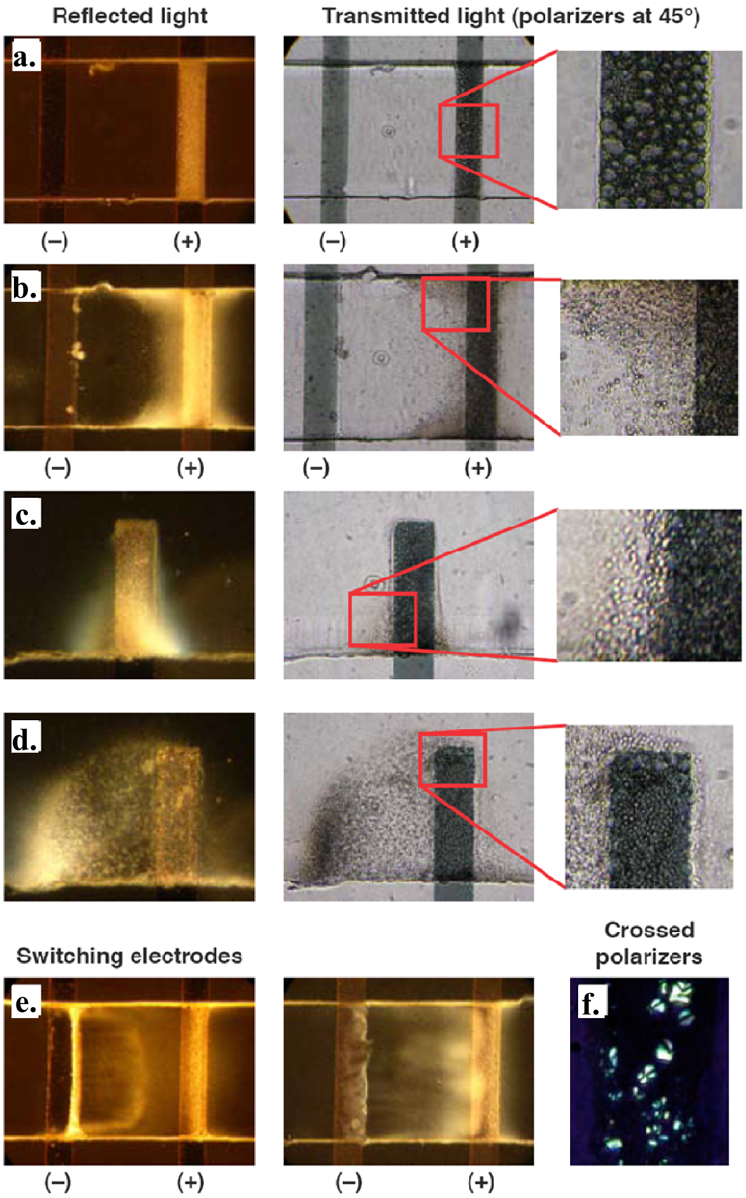

Figure 2.3 (a-d) Reflective zones evident when unlabeled DNA is compacted and viewed under oblique white light (left) are attributable to formation of a stable microbubble layer that can be seen under transmitted polarized illumination (right). In panel (d) the DNA has become ultra-concentrated by sequentially sweeping across 10 electrodes. (e) Microbubbles follow the stabilizing DNA as it migrates from one electrode to the next upon switching the potential (left) and re-accumulate on the new anode (right). (f) Birefringent zones sometimes become evident when viewed through crossed polarizers. All experiments were performed using a 100 bp dsDNA ladder initially at 20 µg/mL in 50mM histidine with 10 %v/v β-mercaptoethanol, 1.8 V applied for 2.5 min. Scale: all electrodes are 50 µm wide horizontally.

We also observed the biomolecule compaction layer at the electrode surface using confocal laser scanning microscopy of fluorescently labeled DNA as a probe to obtain cross-sectional slice views with confocal laser scanning microscopy (Figure 2.4). By scanning the laser across successively higher planes above the electrode surface (~ 2.5 μm resolution in the z-direction), we obtained a 3-D mapping of fluorescence that helped establish the spatial extent of the compacted layer near the electrode surface. This observation shows the DNA compaction layer is preferentially distributed near the microchannel sidewalls, most likely owing to the steeper electric field gradients present there. This information should, in principle, allow the concentration within the compacted layer to be quantified. But in practice, we found that reflection from the electrodes made it difficult to decouple the fluorescence signal due only to the captured DNA. Nevertheless, these experiments provide a useful qualitative picture of how DNA is distributed near the electrode surface.

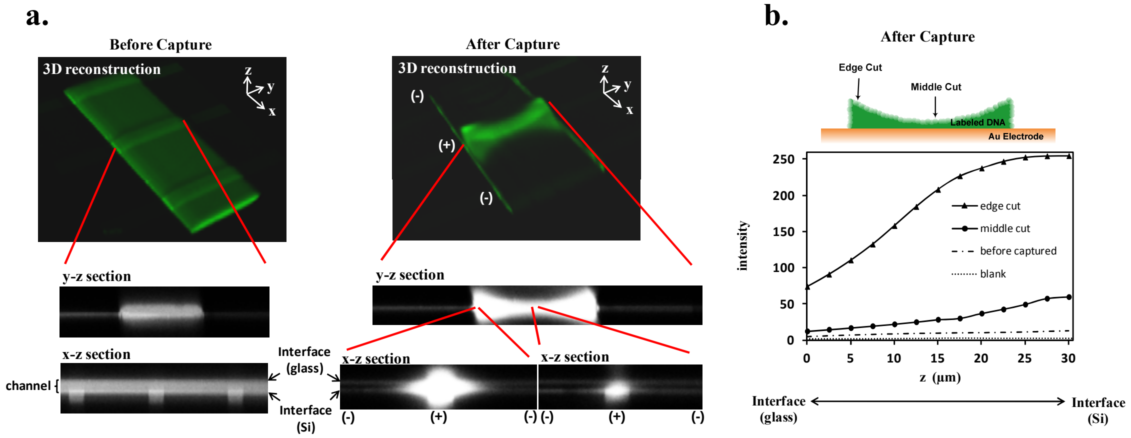

Figure 2.4 Confocal laser scanning microscopy provides a 3-D view of the electrophoretically compacted DNA layer. (a) Cross-sectional slice views of the DNA layer (100 bp dsDNA ladder labeled with YOYO-1 initially at 10 µg/mL in 50 mM histidine buffer, 1 V) before and after compaction. (b) Corresponding cross-sectional intensity profile above the electrode surface. Images were acquired using a confocal microscope (Leica) with a 10x objective (2x zoom) at 400 Hz scanning speed and ~ 2.5 µm resolution in the z-direction.

2.3 Macromolecular Transport and Compaction

In previous group member's studies, we have shown that compaction of charged biomolecules at the electrode surface is electrophoretically dominated[59]. Briefly, we consider the case of DNA and note that the process is performed in a sealed environment to prevent evaporation and confine the liquid within a fixed volume to restrict bulk flow (Figure 2.5). The underlying mechanisms can therefore be understood by considering the relative influence of electrophoretic, electroosmotic, and electrochemical effects (electrolysis of water becomes significant at potentials above ~ 1.3 V). Diffusion of compacted DNA molecules from the anode surface can be neglected by considering a ~ 20 s compaction time, which yields a characteristic diffusion length scale of $(2Dt)^{0.5} \approx 8$ µm (~ 30 times smaller than the spacing between two electrodes). Here, t is the compaction time, and D is the diffusion coefficient of DNA molecules (estimated to be 1.4 x 10^{-9} cm^2/s[64]). Additionally, dielectrophoretic effects are expected to exert a relatively small influence under these conditions because the DC electric fields are of comparatively low magnitude and not strongly divergent, except perhaps in the immediate vicinity of the electrode corners.

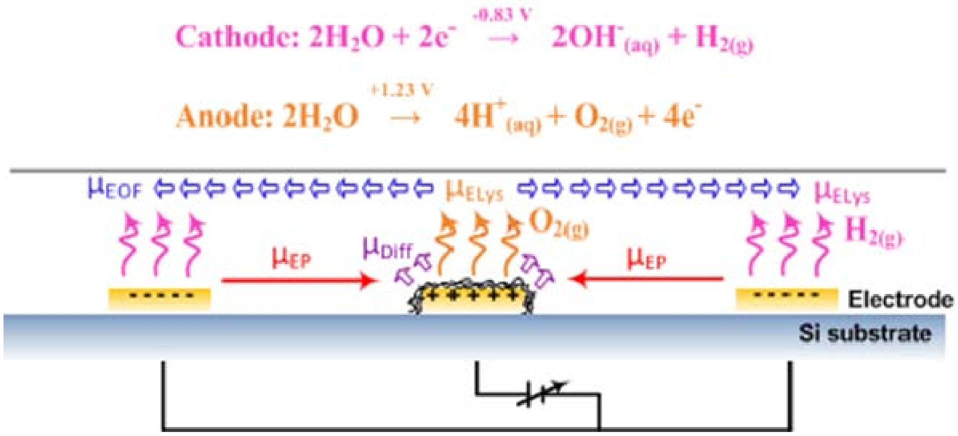

Figure 2.5 Overview of key physiochemical mechanisms associated with macromolecular compaction and subsequent microbubble formation. Charged macromolecules are electrophoretically transported to the electrode surface where they are locally subjected to gas evolution due to water electrolysis. Oxygen is produced at the anode and hydrogen is produced at the cathode above a threshold potential of ~ 1.3 V.

To characterize the influence of electroosmosis, we note that electroosmotic pumping is localized between the active electrode pair inside the microchannel, in contrast to the more conventional configuration where an electric field is applied across the entire channel length. In this case of localized electroosmosis, the balance between hydrodynamic effects inside and outside the actively pumped region results in a scaling of pumping velocity with applied potential between electrodes rather than electric field strength[65]. An estimate of the characteristic electroosmotic velocity can then be obtained from $\mu_{EOF} = \varepsilon\varepsilon_0\zeta V/\eta L$, where ε is the dielectric constant of the buffer solution, ε_0 is the permittivity of free space, ζ is the zeta-potential of the buffer solution, V is the applied potential, η is the fluid viscosity, and L is the entire length of the microchannel from inlet to outlet. Assuming characteristic material properties for water at room temperature ($\zeta = 100$ mV for the silicon/glass surface[66], a 1 V potential and $L = 3.1$ cm) yields a value of $\mu_{EOF} \approx 2.3$ μm/s.

An estimate of the characteristic electrophoretic migration velocity (μ_{EP}) can be obtained from the free solution mobility of double-stranded DNA ($\mu_0 \approx 4.5\times10^{-4}$ $\text{cm}^2/\text{V}\cdot\text{s}$ in TBE buffer[67]) and the electric field strength ($E \approx 40$ V/cm), yielding a velocity of $\mu_{EP} = \mu_0 \cdot E \approx 180$ μm/s. This result can be used to estimate the time for DNA to travel across the entire 250 μm interelectrode spacing (~ 2 s). It can be seen that, μ_{EOF} is nearly two orders of magnitude smaller than μ_{EP}, which is calculated on an open channel configuration and expected to represent an idealized upper limit to the actual μ_{EOF} achievable in the sealed arrangement. Therefore, we can infer that the process by which the DNA migrates toward the anode and forms a compacted film occurs quickly, after which the confined DNA interacts with gasses evolved due to the electrolysis of water (i.e., to form microbubble clouds).

According to the abovementioned, collection and enrichment of charged macromolecules within these electrode arrays is electrophoretically dominated owing to their internal arrangement within an enclosed microchannel, rendering electroosmotic velocity proportional to the applied potential rather than the electric field[59] (characteristic electrophoretic velocities are ~ 100 times greater than those due to electroosmosis) — a feature that distinguishes this phenomenon from anomalous DNA condensation effects previously reported under AC fields[68, 69]. Consequently, the governing mechanism can be viewed in terms of a local competition between (i) electrophoretic transport and compaction of charged macromolecules from the bulk solution into a thin film at the electrode surface, and (ii) the gas-producing electrochemical reactions responsible for bubble formation (i.e., hydrolysis of water yielding oxygen at the anode and hydrogen at the cathode). Using DNA as a probe to explore these interactions, we observe that the compacted film is only visible with the aid of fluorescent labeling at potentials below the threshold for electrolysis (~ 1.3 V) (Figure 2.6 a). Microbubble clouds appear as the potential begins to exceed this threshold, accompanied by emergence of strong surface reflectivity (Figure 2.6 b). As the potential is increased further, locally oversaturated gasses begin to coalesce into larger bubbles at the cathode after several minutes, but not at the anode where the compacted DNA film is localized (Figure 2.6 c). This behavior is much different than would be expected if the stabilizing film were not present because oxygen bubbles produced at the anode generally exhibit weak adhesion to metal electrodes and should therefore coalesce to a larger size than the cathodically generated hydrogen[70, 71]. If the potential is applied for a sufficiently long time, the stabilizing capacity of the macromolecular film saturates yielding coalescence at the anode, albeit to a lesser extent than at the cathode (Figure 2.6 d). This coalescence ruptures the compacted film, an effect that becomes visible as a dark zone centered on the anode flanked by bright regions on either side when the DNA is fluorescently labeled (Figure 2.6 e). No surface reflectivity is evident when carboxylated polystyrene beads are substituted for DNA, indicating that the rigid microspheres are unable to adopt a sufficiently dense packing to stabilize a microbubble layer despite their enrichment at the anode. This mechanism can be further tuned by altering the interplay between electrochemical and electrophoretic effects as demonstrated by addition of sodium dithionite ($Na_2S_2O_4$), a reducing agent that inhibits microbubble formation by establishing a competitive complexation interaction accelerating uptake of evolved oxygen (Figure 2.6 f).

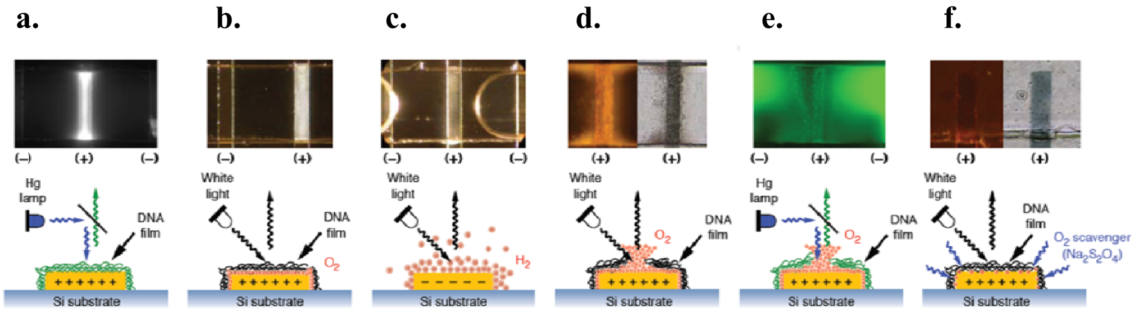

Figure 2.6 (a) Microbubble clouds are not evident below the electrolysis threshold, even though electrophoretically compacted DNA is visible when fluorescently labeled (100 bp dsDNA ladder labeled with YOYO-1 initially at 10 µg/mL in 50 mM histidine, 0.7 V). (b) Above this threshold the electrophoretically compacted DNA film acts to stabilize electrolytically produced oxygen microbubbles, generating strong reflectivity under oblique white light illumination (100 bp dsDNA ladder initially at 12 µg/mL in 10x TBE, 2.5 V). (c) The stabilizing macromolecular film resists local oversaturation so that coalescence into larger bubbles occurs more readily at the cathode (heptakis (6-O-sulfo)-β-cyclodextran initially at 100 µg/mL in 10x TBE, 3 V). (d) Oversaturation eventually sets-in at the anode under high potentials and/or at long times, rupturing the compacted film (100 bp dsDNA ladder initially at 20 µg/mL in 50 mM histidine, 1.8 V; images under reflected and transmitted light are shown at the left and right, respectively). (e) When fluorescently labeled, the ruptured DNA film is evident by a dark region on the anode flanked by bright zones on either side (100 bp dsDNA ladder labeled with YOYO-1 initially at 10 µg/mL in the supplied buffer, 1.5 V). (f) Microbubble clouds are no longer evident under either reflected (left) or transmitted (right) illumination upon addition of a reducing agent (100 bp dsDNA ladder initially at 20 µg/mL in 50 mM histidine with 0.06% w/v $Na_2S_2O_4$, 2.5 V applied for 30 min). Scale: all electrodes are 50 µm wide horizontally.

2.4 Kinetic Analysis of Microbubble Cloud Formation

Since both the number and size of attached bubbles varies over time[70], the average microbubble size and coverage can be used to characterize the bubble growth rate in terms of the reflected intensity under oblique white light illumination. We recorded the DNA capture process under different conditions and used image analysis to quantify the increase in reflected light intensity within a region of interest centered on the anode as a function of time upon application of a potential (Figure 2.7) Kinetics were characterized by fitting these data to a single-parameter exponential equation: y = 1-exp(-t/τ). Here, y is the normalized intensity of the compacted DNA film, t is the time in seconds, and τ is a characteristic time constant associated with microbubble formation.

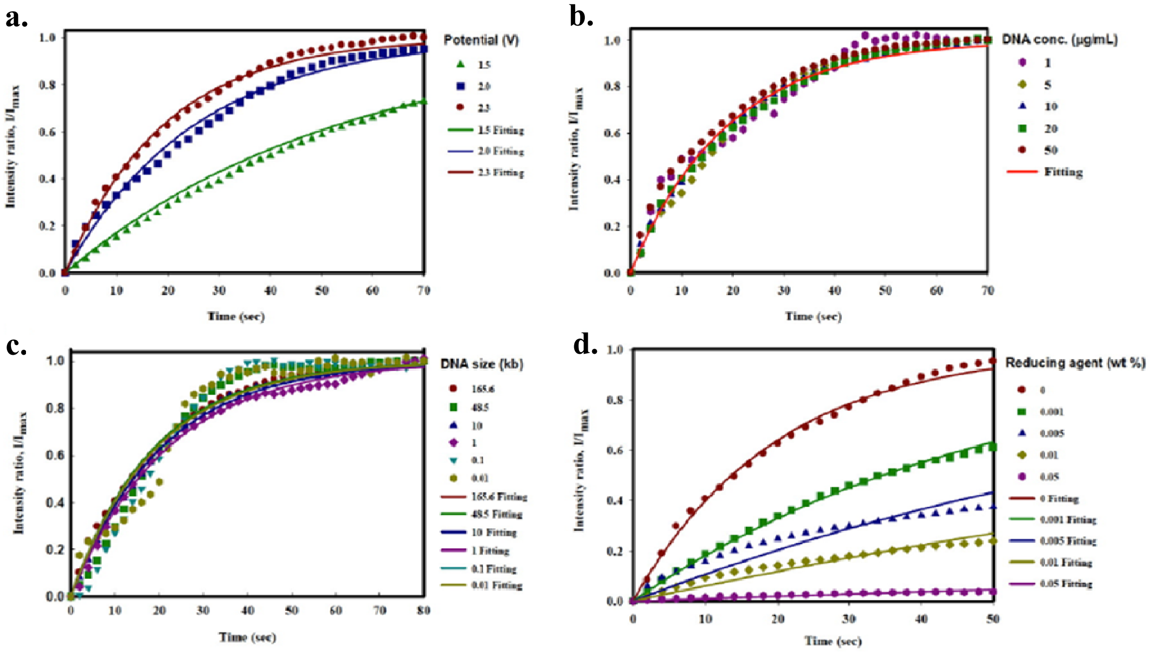

Figure 2.7 Normalized kinetic data associated with formation of microbubble layers in unlabeled DNA capture experiments (data in (a-d) correspond to plots in Figure 2.8, respectively). The resulting time constants are reported in Table 2.1. Data are shown for experiments varying (a) applied potential, (b) initial DNA concentration, (c) DNA fragment length, and (d) reducing agent concentration.

As mentioned above, we quantified the kinetics of microbubble cloud formation by recording the increase in reflected light intensity as a function of time within a region of interest centered on the active electrode so that representative time constants could be extracted. Reflectivity increases at a rate proportional to the applied potential[72, 73], reaching a plateau within ~ 60 s (Figure 2.8 a); and kinetics remain unchanged as the initial DNA concentration is varied from 10 to 50 µg/mL (Figure 2.8 b). Changes in DNA length influence the reflected intensity but do not strongly affect the kinetics, with T4 DNA (165 kb) able to stabilize larger microbubbles and generate stronger reflectivity than the much shorter 10 bp fragments (Figure 2.8 c). The corresponding time constants indicate that the kinetics maintain a similar order of magnitude across the entire ensemble of experimental conditions we investigated, implying that microbubble cloud formation is governed by a fundamentally consistent electrochemical mechanism (Table 2.1). Addition of $Na_2S_2O_4$ disrupts this balance, inhibiting development of the microbubble clouds and delaying attainment of an intensity plateau (Figure 2.8 d). But the magnitude and kinetics of surface reflectivity are eventually restored as the reducing agent is consumed by repeatedly actuating the electrodes (Figure 2.9).

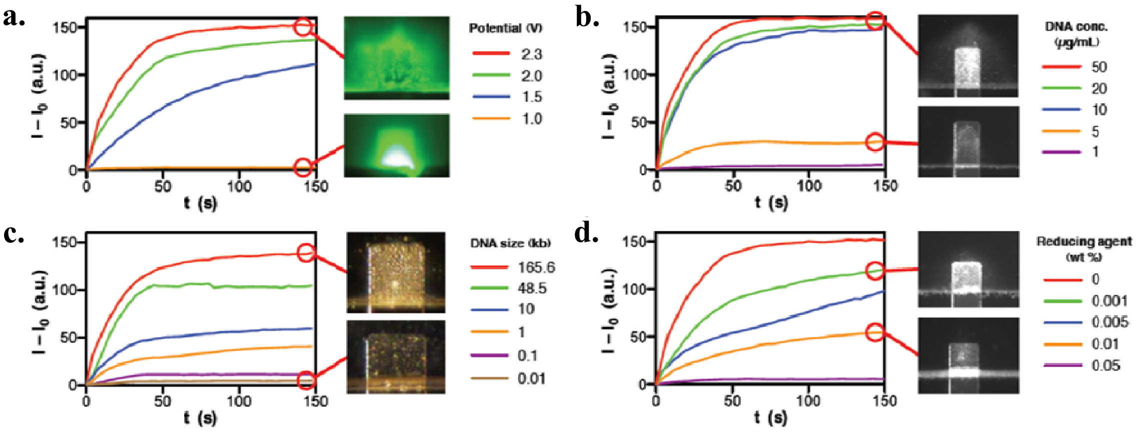

Figure 2.8 Kinetics of microbubble cloud formation. (a) Effect of applied potential (unlabeled 100 bp dsDNA ladder initially at 20 μg/mL in 50 mM histidine). (b) Effect of initial DNA concentration (unlabeled 100 bp dsDNA ladder in 50 mM histidine, 2.3 V). (c) Effect of DNA length (all samples initially at 20 μg/mL in 50 mM histidine, 2.3 V). (d) Effect of reducing agent $Na_2S_2O_4$ (unlabeled 100 bp dsDNA ladder initially at 20 μg/mL in 50 mM histidine, 2.3 V). Scale: all electrodes are 50 μm wide horizontally.

Table 2.1 Time constants τ associated with evolution of microbubble clouds in DNA capture experiments, obtained by fitting the kinetic data to a single-parameter exponential equation: $y = 1 - \exp(-t/\tau)$. All experiments were performed at a potential of 2.3 V, except for the data where the applied potential was varied

(Figure 2.8 a)		**(Figure 2.8 b)**		**(Figure 2.8 c)**		**(Figure 2.8 d)**	
Applied potential (V)	**t (s)**	**DNA conc. (μg/mL)**	**t (s)**	**DNA size (kb)**	**t (s)**	**Reducing agent (wt %)**	**t (s)**
1.5	53.6	1	18.3	165.6 (T4)	18.9	0	19.7
2.0	25.5	5	19.2	48.5 (λ)	18.9	0.001	50.1
2.3	19.3	10	18.9	10	20.4	0.005	88.3
		20	19.3	1	21.9	0.01	159.0
		50	16.4	0.1	19.4	0.05	1053
				0.01	19.3		

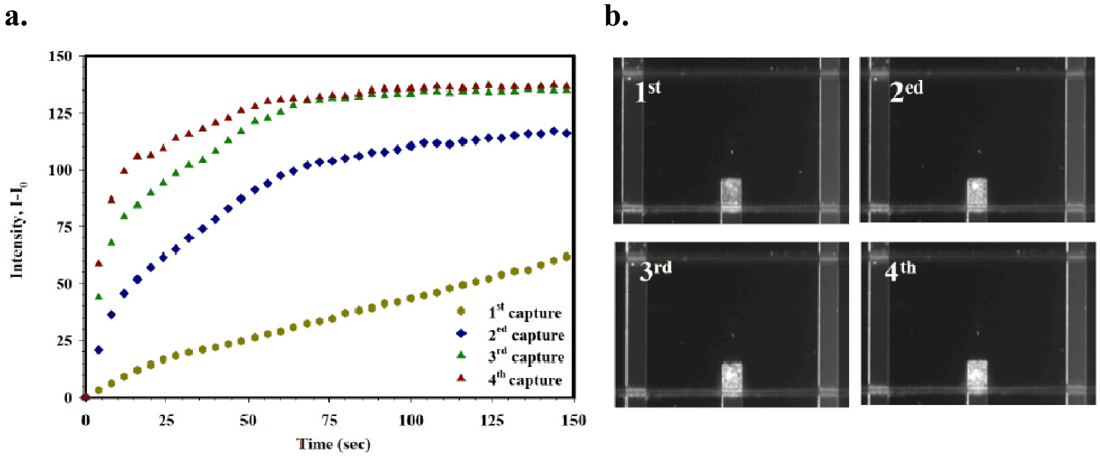

Figure 2.9 Decreased reflectivity in the presence of a reducing agent is restored when the DNA capture process is repeatedly performed. (a) Kinetics of surface reflectivity growth in response to repeated electrode capture. (b) Corresponding images show restoration of surface reflectivity (100 bp dsDNA ladder initially at 20 µg/mL in 50mM Histidine buffer with 0.01 wt% of $Na_2S_2O_4$, 2.3 V potential).

2.5 Materials and Methods

The setup and measurements of above the experiments are as follows:

2.5.1 Microchip Fabrication and Assembly

Design, construction, and operation of the microfabricated electrode array devices have been described in detail previously[59, 74]. Briefly, the devices consist of three main components: a silicon microchip (7.5 x 35 mm), a glass microchannel (3.9 x 33.5 mm), and a printed circuit board (4 x 6.4 cm). Silicon wafers (P(100), 500 µm thick, 15 cm diameter, 5,000 Å oxide layer; University Wafer), were cleaned in a reactive ion etcher, spin coated with hexamethyldisilazane (J.T. Baker) followed by a positive photoresist (Shipley 1827; Rohm & Haas Electronic Materials), patterned, and developed (MF-319 developer; Rohm & Haas Electronic Materials). Most studies were performed using platinum electrodes fabricated by depositing a 500 Å layer of titanium followed by a 1,000 Å layer of platinum using an electron beam evaporator. Transparent gold electrodes for experiments performed under transmitted light illumination were fabricated by depositing a 50 Å layer of chromium followed by a 200 Å layer of gold using a thermal evaporator. Glass microchannels were fabricated by depositing a 600 Å chromium layer followed by a 4,000 Å gold layer on glass wafers (borofloat, 500 μm thick, 15 cm diameter; Precision Glass and Optics) that had been cleaned in a reactive ion etcher. The wafers were then spin-coated with positive photoresist (Shipley 1827), patterned, developed with MF-319, and hard baked. After immersion for 10 min each in gold etchant (Transene) and chromium etchant (Cyantek), the exposed glass was then etched with a freshly prepared 7:3 (vol/vol) solution of hydrofluoric and nitric acids (etch rate ≈ 5 μm/min) to a channel depth of 45 μm (width = 275 μm). After dicing, fluidic access holes were drilled using an electrochemical discharge process. Silicon devices were mounted on printed circuit boards and wire-bonded to provide electrical connections. Glass microchannels were then bonded to the silicon device using a UV curable optical adhesive (SK-9 Lens Bond; Summers Laboratories).

2.5.2 Sample Preparation

Electrode capture experiments involving DNA were carried out using a 100 bp double-stranded DNA ladder (Bio-Rad) and monodisperse DNA samples with lengths of 10, 100, 1000, 10 kb (Fermentas), 48.5 kb (λ DNA; cat. no. N3011S, New England

BioLabs), and 165.6-kbp (T4 DNA; cat. no. 318-03971, Wako USA). The DNA samples were suspended in TBE (extended-range TBE; Bio-Rad) and histidine (Sigma-Aldrich) buffers. Experiments investigating addition of a reducing agent were performed using sodium dithionite ($Na_2S_2O_4$; Riedel-deHaën). Unlabeled samples were used as prepared, fluorescently labeled samples were prepared by adding YOYO-1 intercalating dye (Invitrogen/Molecular Probes) and β-mercaptoethanol (BME; Sigma–Aldrich) to inhibit photobleaching. Master mixes of fluorescently labeled DNA samples (10 μL) were prepared by adding the as-supplied DNA solution to 0.05 mM YOYO-1 intercalating dye in a 2:1 (vol/vol) ratio. After incubation for several minutes at room temperature, the suspension buffer was extracted with a vacuum centrifuge evaporator. The sample was then resuspended in the appropriate buffer system, and the desired amount of BME or reducing agent was added. Unlabeled DNA samples were prepared in the same way, but without addition of YOYO-1 and BME.

2.5.3 Microdevice Operation

DNA samples were loaded into the microchannel using a micro-needle tipped syringe, and access holes were sealed with removable adhesive to prevent evaporation. The same device could be used repeatedly for multiple samples after thoroughly rinsing with deionized water. Extensive comparison of results between new and reused devices indicated that no appreciable electrode fouling (as evidenced through accumulation of residue on the electrodes or glass channel walls and/or through significant deviations in electrode capture response) occurred as a consequence of repeated use when this cleaning procedure was followed.

2.5.4 Imaging and Detection

The electrode capture process was imaged using an Axioskop-2 Plus microscope (Zeiss) interfaced with an Orca-ER digital CCD camera (Hamamatsu). A combination of Openlab automation software (Improvision) and ImageJ open source analysis software was used to acquire images and extract intensity data within a user-defined region of interest. Intensity versus time data were fit to a single-parameter exponential equation using Origin software (OriginLab Corporation). For flow visualization studies, a dilution of 1 μm-diameter, carboxylate-modified polystyrene microspheres (FluoSpheres; cat. no. F-8823, Invitrogen/Molecular Probes) were added to serve as tracers.

CHAPTER III

UNLABELED DETECTION OF DNA *VIA* ELECTROCHEMICAL DISSOLUTION OF MICROFABRICATED CHROMIUM ELECTRODE ARRAY[*]

This chapter provides a novel approach that enables unlabeled biomolecules and chemical analytes to be detected using ordinary smartphone optics, which expands the use of advanced diagnostic capabilities. Electrochemical reactivity of chromium, ordinarily considered detrimental, is harnessed here to generate a signature that can be easily seen by monitoring electrode degradation under ordinary white-light illumination. The simplicity and robustness of this approach eliminates the need for labeling and/or pre-programming with specific receptors (e.g., oligonucleotide probes), making it feasible to greatly expand availability of a host of assays where detection complexity is a limiting constraint.

3.1 A Novel Unlabeled Detection Approach by Using Highly Reactive Chromium Electrode Array

The ability to detect unlabeled analytes, particularly biomolecules representing specific targets of interest, is a key to enabling broad availability of inexpensive

---

[*] Part of the data reported in this chapter is reprinted with permission from: Smartphone-Based Detection of Unlabeled DNA *via* Electrochemical Dissolution by Huang, Y.-W. and Ugaz, V. M., *Analyst*, **2013**, 138, 2522-2526. Copyright [2013] by The Royal Society of Chemistry.

diagnostic assays. Existing strategies predominantly involve introducing detectable probes that interact with the sample *via* chemical reactions or specific binding interactions with targeted receptors. Gold nanoparticles[75-79], quantum dots[80], magnetic nanoparticles[6, 81-83], and microfabricated cantilevers[84-86] have all been harnessed to enable sensitive optical and electrochemical detection of hybridization events. But these methods must be pre-programmed with appropriate receptor probes (e.g., oligonucleotides in the case of DNA detection) and often require multiple sample preparation and washing steps in order to perform optimally. If detection could be performed without labeling the sample or pre-programming the assay with specific probes, workflows associated with routine diagnostic assays (e.g., PCR) could be greatly simplified. This capability would be particularly beneficial in resource lean settings where a premium is placed on simplicity and robustness, as opposed to raw sensitivity[45-49].

Here we report a new approach that addresses these needs by exploiting electrochemical reactivity of chromium to permit true label-free detection via an easily visible signature (Figure 3.1). Chromium's inherent instability, ordinarily considered undesirable, is advantageous here because the rate of electrode degradation strongly depends on the bulk solution composition. These kinetics therefore reflect an interplay between electrochemical dissolution and electrophoretic transport of analytes to and from the electrode surface. The process is easy to monitor because the electrodes are large enough to view using simple optics (e.g., a smartphone camera).

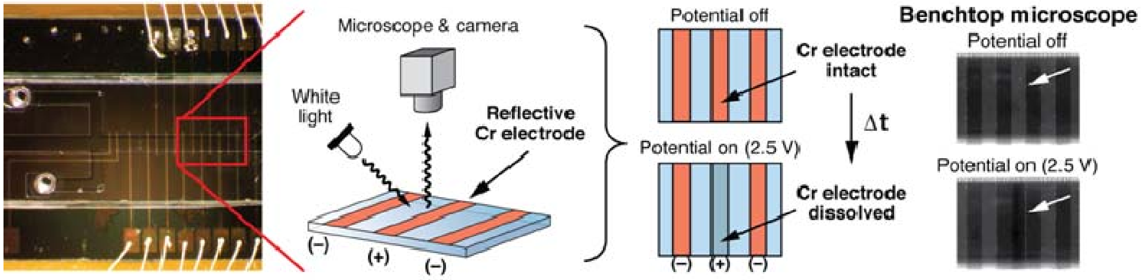

Figure 3.1 The microdevice design incorporates a glass microchannel (275 x 45 μm cross-section) bonded to a Si substrate patterned with a Cr microelectrode array. When a 2.5 V potential is applied, the Cr electrodes electrochemically dissolve at a rate dependent on the chemical composition of the bulk solution (arrows). The dissolution process can be readily detected by observing the change in reflected light intensity from the electrode surface.

To demonstrate the detection method, we constructed a microfluidic system incorporating an addressable chromium electrode array patterned along the microchannel floor (Figure 3.1) — an arrangement that allows very small potentials (2.5 V) to generate locally high electric fields (hundreds of V cm^{-1})[59, 87]. Electrode dissolution is monitored by recording the change in surface reflectivity with time under oblique illumination with ordinary white light, from which the average intensity within a region of interest centered on the electrode can be quantified. In this way, changes in dissolution rate in response to the bulk solution's chemical composition can be readily distinguished[88].

Despite its outward simplicity, the underlying chemical and physical processes governing electrode dissolution are relatively complex, owing to an interplay between electrophoretic transport of analytes toward and subsequent compaction at the surfaces of electrodes where the corresponding electrochemical reactions are localized. These surface phenomena are in turn influenced by local pH, ionic environment, and the activity of side reactions. The pH of aqueous solution directly affects the solubility of metal compounds[89]; and higher ionic strength reduces the thickness of electrical double layer to replace the Cr ions with cations in the bulk solution to cause more rapid metal dissolution[89, 90]. Dissolution kinetics at the electrode surface in an aqueous acidic environment can be broadly characterized in terms of the following mechanism[91-93].

$$Cr + H_2O \leftrightarrow CrOH_{ads} + H$$

$$CrOH_{ads} + H_3O^+ \rightarrow CrOH^+ + H + H_2O$$

$$CrOH^+ + H_3O^+ \leftrightarrow Cr^{2+} + H_2O$$

These kinetics are superimposed on corresponding reactions associated with electrolytic production of hydrogen and oxygen at the anode and cathode. The sensitivity of both these pathways to analyte composition forms the basis of our detection strategy.

3.2 Compositional and Size Dependence of the Chromium Dissolution Kinetics

We initially studied the fundamental performance of chromium electrodes by using fluorescently labeled DNA as a probe under different bulk conditions and recorded the change of fluorescent intensity as a function of time to obtain the reaction kinetics. The preliminary results show that the chromium electrode dissolution is highly related to the initial DNA concentration (Figure 3.2) and the compositions of buffer solution. This observation is promising to harness this reactivity as the basis of a new detection method whereby the rate of electrode dissolution is monitored and correlated with properties of the bulk solution. However, the fluorescent intensity cannot exactly response either the electrode dissolution or the DNA compaction processes since the intensity reflects both of the DNA concentration and the electrode surface reflectivity, which are tangled to each other and become difficult to separate individually. While the electrod dissolves completely, for instance, DNA starts to unpack slowly and the intensity decreases. The intensity decreasing rate retards at the highly compacted case (high concentrated DNA samples), and the intensity cannot restore since there is no electrod surface reflectivity. Thus, using unlabeled DNA samples would be the best way to display the electrode dissolution kinetics.

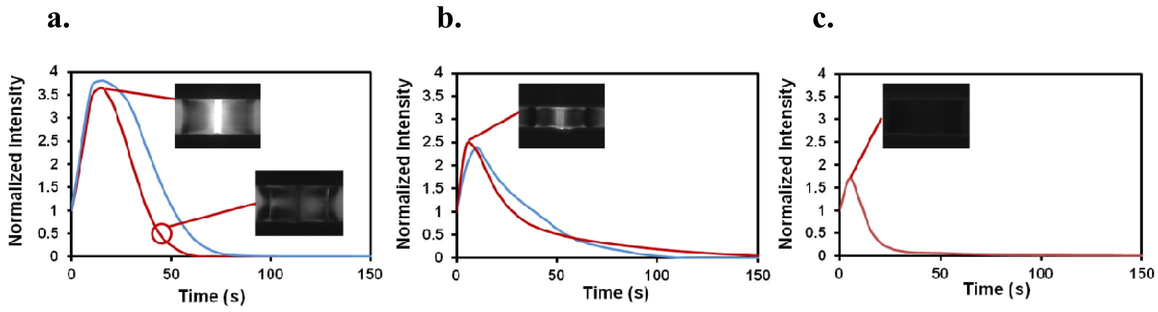

Figure 3.2 Effect of initial DNA concentration to chromium electrode compaction. DNA compaction experiments were performed using a 100 bp ds DNA ladder labeled with YOYO-1 in 50 mM histidine at 2.5V. The initial DNA concentration is 20 μg/mL (a), 10 μg/mL (b) and 5 μg/mL (c). Scale: all electrodes are 50 μm wide horizontally.

We made the next attempt to examine this compositional dependence by considering a panel of four different analytes: histidine buffer (50 mM, pH 7.6), a 100 bp dsDNA ladder (20 μg mL^{-1} in 50 mM histidine), a reducing agent (0.06% w/v $Na_2S_2O_4$ in 50 mM histidine), and at low pH (50 mM histidine, pH 4.4). Experiments were performed using a benchtop-scale microscope to observe the electrode dissolution process and record its time history for each sample composition. Our observations, shown in Figure 3.3 a, indicate several key trends. Electrode dissolution proceeds slowest in the near-neutral pH buffer environment, our base case for comparison. Addition of dsDNA accelerates the dissolution timescale somewhat, suggesting an influence of the electrophoretically compacted DNA film. Addition of a reducing agent at near neutral pH further accelerates dissolution, suggesting that its oxygen scavenging activity plays an important role. Finally, we observe that dissolution proceeds most rapidly in the low pH buffer. Good reproducibility was observed in all cases, with the only caveat being that a small degree of uncertainty was introduced because we manually synchronized actuation of the electrodes with the video recording.

These observations highlight the importance of the local pH environment in the vicinity of the electrode in governing the electrode dissolution process. Compared to the base case of buffer at near neutral pH, dissolution kinetics are accelerated either by addition of a reducing agent or by pH adjustment to a lower value, reflecting the inherent pH dependence of the above mentioned kinetic mechanism governing dissolution. In addition to direct compositional adjustment, addition of a reducing agent may also act to lower the local pH by introducing an oxygen scavenging side reaction. The behavior observed upon addition of DNA is somewhat less intuitive. We hypothesize that the electrophoretically compacted DNA film may influence the process by imposing a physical transport barrier that acts to enhance the local hydrogen ion concentration associated with the surface reaction products, yielding a local shift to lower pH that favors dissolution. The consequences of this interplay become further evident by comparing dissolution kinetics observed with DNA samples of different length (Figure 3.3 b; all samples prepared at 20 µg mL^{-1} in 50 mM histidine). These data display dramatically slower kinetics with increasing DNA length, accompanied by a visible morphological change at the electrode surface where the uniform dissolution is seen in the 100 bp ladder sample assumes a speckled pattern characterized by discrete reflective spots at longer DNA sizes. These differences suggest potential for some degree of size-dependent selectivity.

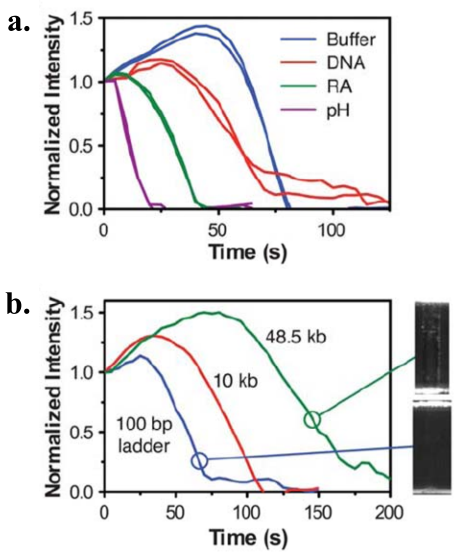

Figure 3.3 Electrode surface reflectivity unfolds differently during dissolution involving different analytes. (a) Evolution of reflected light intensity from the active electrode displays composition-dependent behavior as evident by comparing dissolution kinetics of histidine buffer (50 mM, pH 7.6), a 100 bp dsDNA ladder (20 µg/mL in 50 mM histidine), a reducing agent (0.06% w/v $Na_2S_2O_4$ in 50 mM histidine), and at low pH (50 mM histidine, pH 4.4). Results from two independent experiments are shown for each analyte to assess reproducibility. (b) The dissolution process evolves more slowly when DNA fragments of increasing length are probed (all samples prepared at 20 µg/mL in 50 mM histidine). These differences are accompanied by a transition from uniform reflectivity to the appearance of speckled zones on the dissolving electrode.

3.3 Possibility for Real-Time PCR Detection Application

We next applied this approach to detect a 237 bp PCR product replicated from a λ-DNA template. The PCR products were loaded directly into the microchip with no additional labeling or purification steps. When viewed through a benchtop microscope, the electrode reflectivity data reveal a shift toward faster dissolution when the target DNA is present as compared to the pre-reaction control (Figure 3.4 a). Although various approaches can be envisioned to quantitatively report the change in dissolution kinetics, we chose as a first approximation to examine the shift in the time for the electrode reflectivity to attain a peak value before decreasing due to dissolution. This parameter offers the advantage of being relatively easy to establish independent of run-to-run variations in absolute reflected light intensity. Using this approach, we observed a shift of $\Delta t_{\max}$ = 11.3 s between the pre-reaction control and post-reaction PCR products (Figure 3.4 a). These results demonstrate feasibility to function for PCR product analysis. The above mentioned dependence of dissolution kinetics on DNA fragment length (see Figure 3.3 b) also introduce intriguing possibilities by observing how dissolution kinetics evolve during the course of PCR replication (Figure 3.4 b). The process unfolds reproducibly in both the pre-reaction control and after 30 cycles of replication. But the dissolution profiles display much more variability when examined after 15 cycles, generally reflecting a trend of slower kinetics that we hypothesize may be a manifestation of the presence of long DNA fragments of variable length produced during early cycles prior to the onset of exponential replication of the 237 bp target. The length distribution associated with these non-specific products is inherently variable from run-to-run, potentially explaining the increased variability in dissolution rate observed at this stage of the reaction. It therefore appears feasible that dissolution kinetics could be exploited to extract information analogous to the critical cycle number (C_T) marking the onset of exponential replication by simply observing the transition between reflectivity profiles characteristic of the pre- and post-reaction samples. This is an important parameter that is widely employed to quantify a sample's starting concentration of template DNA, but is predominantly measured using fluorescence-based real-time PCR instrumentation.

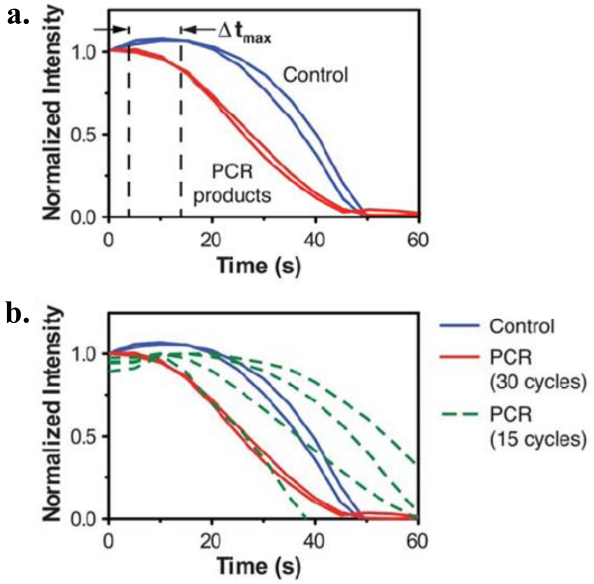

Figure 3.4 PCR products can be detected by observing electrode dissolution kinetics. (a) Accelerated dissolution kinetics are observed in the presence of the post-PCR products, as compared with the pre-reaction control. The time to reach a peak reflective intensity value before decreasing due to dissolution (Δt_{max}) offers a convenient observable parameter that is independent of run-to-run variations in absolute reflected light intensity. Results from two independent experiments are shown for each analyte to assess reproducibility. (b) Dissolution kinetics evolve differently at intermediate cycles of the PCR, likely owing to the presence of longer non-specific products produced at early stages of the reaction, potentially providing a way to determine the onset of exponential target replication.

3.4 Application for Smartphone-Based Detection of Unlabeled DNA

Since dissolution is readily observable under white light illumination owing to the relatively large electrode sizes involved, our method offers potential to function using optics at the level found in current-generation smartphones. Preliminary studies to demonstrate feasibility of smartphone-based imaging were performed with an Apple iPhone 4S using the *iFast Pro* camera app (enabled an 8x digital zoom to be applied during recording). The video files were exported as grayscale TIFF stacks and processed by the same workflow used in the benchtop experiments. A snap-on mini microscope (<$10 US; http://www.amazon.com[94]) was used to achieve increased magnification (Figure 3.5).We used only the mini-microscope's built-in LEDs for illumination in the smartphone experiments. Although electrode degradation could be clearly recorded, the camera's limited resolution and weaker LED illumination (only the mini-microscope's built in light source was used) introduced some variability in the absolute intensity scales that was challenging to systematically address. Instead, we examined the local intensity maximum on the electrode occurring shortly after application of the potential and compared the difference between values recorded in the PCR (post-reaction) and control (pre-reaction) samples (see Figure 3.4 a). Clear shifts were evident, with the intensity maximum occurring Δt_{max} = 11.3 and 13.0 s as determined using the benchtop microscope and smartphone camera respectively. While a number of snap-on microscope accessories are available that can be interfaced with smartphones, we chose this type of microscope because it is inexpensive and widely used for currency detection. Although we selected an iPhone to demonstrate proof of concept, this approach can be generically applied to a variety of smartphones, and is likely to become increasingly robust as imaging capabilities continue to rapidly improve.

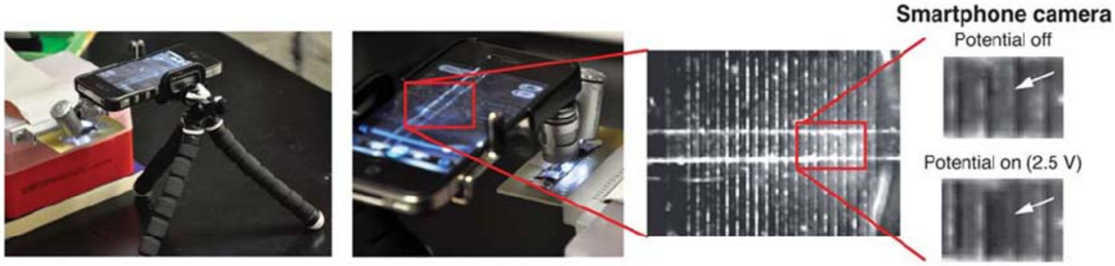

Figure 3.5 The microelectrode arrays are large enough to enable dissolution to be directly imaged using an ordinary smartphone (Apple iPhone 4S). Scale: all electrodes are 50 µm wide horizontally.

3.5 Possible Approaches for Quantification and Explication of the Dissolution Kinetics

Several approaches can be developed to quantify the dissolution kinetics and to examine the possible mechanisms governing the electrode dissolution (Figure 3.6 a). Since the heterogeneity in the numbers renders difficult statistical analysis, we performed data normalization to scale the original surface intensity and to favor the comparison from different batches of experiments. Here, we chose the method with respect to the initial and final values, $I_{\text{normalized}} = (I - I_{\text{final}})/(I_{\text{initial}} - I_{\text{final}})$, to set the initial and final stages equal to 1 and 0 respectively. Then, the underlying mechanisms can be understood by considering various parameters presented on the kinetics profile. In previous studies, we have shown that DNA molecules compact immediately (~ 20 s) and the influence of electrophoresis and electroosmosis are not comparable (chapter 2.3).

Therefore, we simply consider two electrochemical reactions, electrolysis of water and chromium dissolution, dominate the processes and can be represented by the slopes before (S_1) and after (S_2) the time reaching a peak reflective intensity value respectively. The peak value presented in time ($t_{\max}$) and the time when the intensity crosses the x-axis (t_{cross}) can be considered as the break of these two reactions. Also, the peak value tendered in intensity ($I_{\max}$) can associated to the gas-producing reaction responsible for microbubble formation (hydrolysis of water yielding oxygen at anode). The values obtained from above experiments (Figure 3.3) are organized in Table 3.1.

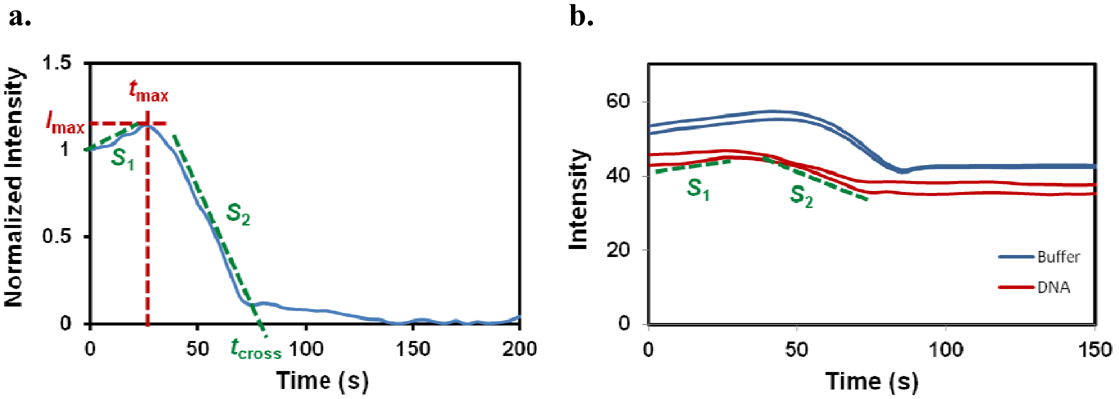

Figure 3.6 Various parameters presented on the kinetics profile associated with the underlying mechanisms. (a) Data normalization to scale the reflective intensity. The slopes before (S_1) and after (S_2) the time reaching a peak intensity value simply imply the reaction rate of two electrochemical reactions, electrolysis of water and chromium dissolution, respectively. The peak time value ($t_{\max}$) and the time when the intensity crosses the x-axis (t_{cross}) are considered as the termination of these two reactions. The peak intensity value ($I_{\max}$) is regarded as oxygen production provided from hydrolysis of water. (b) Original kinetics profile from experiments presents different values of slopes before (S_1) and after (S_2) the peak time since the data normalization twists the curve (data is corresponding to plots in Figure 3.3 a).

Table 3.1 Normalized kinetics parameters associated with two electrochemical reactions, electrolysis of water and chromium dissolution, in unlabeled DNA detection experiments. All experiments were performed at a potential of 2.5 V and data is corresponding to plots in Figure 3.3 a.

Sample	**Normalized**					**Raw**	
	t_{max}	t_{cross}	I_{max}	S_1	S_2	S_1	S_2
Buffer	40	84.0	1.38	0.0093	0.0402	0.0900	0.5089
	45	82.0	1.43	0.0099	0.0486	0.0887	0.4749
DNA	25	78.4	1.14	0.0057	0.0242	0.0465	0.2018
	25	79.3	1.27	0.0061	0.0236	0.0421	0.2199
RA	5	44.59	1.051	0.0102	0.0330	0.4026	1.3067
	5	45.08	1.069	0.0138	0.0332	0.5090	1.2254
pH	5	19.69	1.003	0.0005	0.0668	0.0216	2.7258
	5	19.57	1.010	0.0020	0.0651	0.0582	1.9119

Although Table 3.1 provides several viewpoints to examine the possible reaction processes, the over-simplification however cannot view the underlying mechanisms completely. The addition of hydrogen ions under low pH condition, for instance, speed the chromium dissolution but the oxygen produced reaction also provides hydrogen ions. In addition, the electrolysis of water proceeds continuously at the potential above ~ 1.3 V which makes it becomes difficult to cut these two reactions at any point. Furthermore, the data normalization set the initial and final stages are the same at all conditions which is like to tie the heads and toes of the curves and twists them to acquire the values of slopes (Table 3.1 and Figure 3.6 b) that are somehow different with the slopes obtained from the original data and cause misinterpretation of the kinetics in some way. The entire processes are relatively complicated even more than we can image at this moment that further studies can provide additional information to simplify appropriately. Simultaneous real-time measurement of reaction current as a function of time (Figure 3.7) can provide the additional information of total charges during the process. The analysis of the electrochemical noise from the current fluctuation can indicate the dimensions of gas microbubbles detaching from the electrodes associated with the bulk compositions[95, 96] that may provide the further investigation of water electrolysis to optimize the applications of electrochemical dissolution.

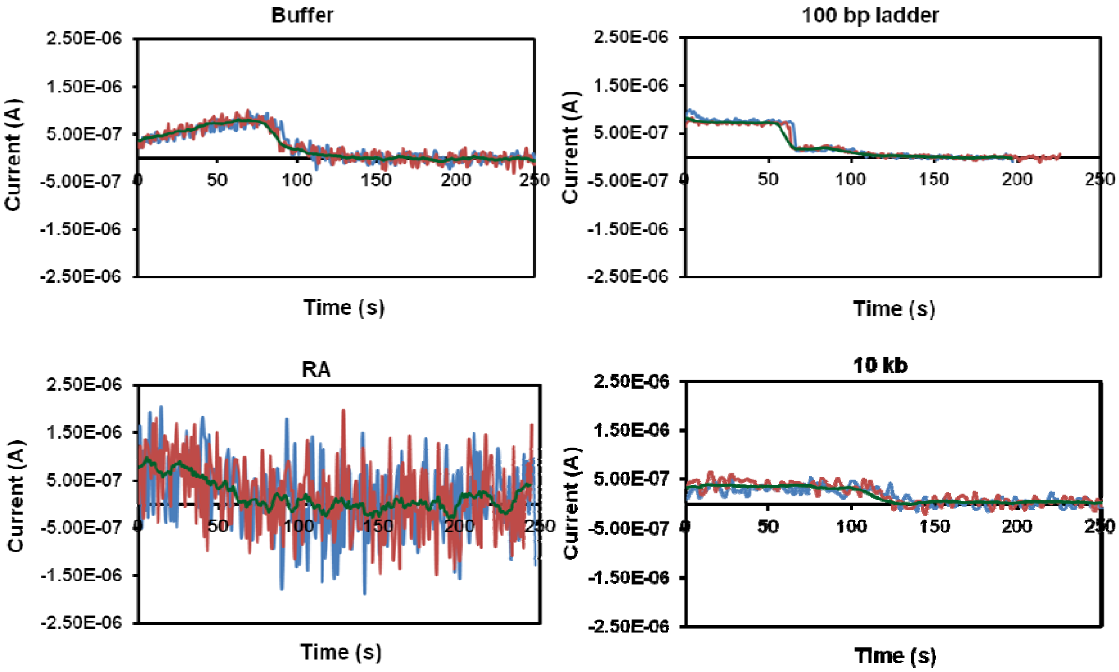

Figure 3.7 Simultaneously measure the reaction current as a function of time (data is corresponding to plots in Figure 3.3). Results from two independent experiments are shown for each analyte to assess reproducibility. Trendlines (green lines) are displayed the similar behavior among all compositions. Violent fluctuation was observed with reducing agent added. All experiments were performed at a constant potential of 2.5 V.

3.6 Progress and Outlook

We emphasize that the envisioned application for this technology is as a detection method for PCR-based assays. In this context, it is expected that products from a single reaction will be repeatedly analyzed, and that robust reaction conditions maximizing replication of the desired product have already been identified. In other words, our approach would be analogous to SYBR Green-based PCR analysis in the sense that the observed optical signal may not strongly discriminate between the product and any primer-dimers that may be present in an unoptimized reaction. In this scenario, that of a repeated robust diagnostic test, our approach offers a considerable advantage in terms of simplicity that outweighs some loss in overall selectivity. Therefore, while we do not anticipate that this method will be able to match the ultra-sensitive detection levels of conventional label- and/or probe-based approaches, the ability to detect analytes like PCR products using relatively crude smartphone-based optics is desirable in many settings. This capability is particularly remarkable considering that no labeling additives or chemical probes (e.g., sequence specific oligonucleotides) of any kind are employed. The same attributes that make chromium a poor choice for conventional electrochemistry (i.e., high reactivity) are precisely those that enable this approach to rapidly produce a visible signature representative of the analyte. Specificity can be enhanced by embedding tailored chemical functionality within the electrodes, albeit at the expense of added complexity. A further benefit of the chromium-based format is the ability to directly employ standard photomask plates as devices when optically transparent substrates are desired. Photomask manufacture is a standard process that inherently yields precise patterning and is widely available for small-batch fabrication needs so that new designs can be easily tested. This favorable combination of attributes make our approach a good candidate to greatly expand the use of advanced diagnostic capabilities, particularly in resource-lean settings where simplicity and robustness are paramount[2].

3.7 Materials and Methods

The setup and measurements of above the experiments are as follows:

3.6.1 Microchip Fabrication and Assembly

Design, construction, and operation of the microfabricated electrode array devices has been described in detail previously[59, 87]. Briefly, silicon wafers (P(100), 500 μm thick, 15 cm diameter, 5000 Å oxide layer; University Wafer), were cleaned in a reactive ion etcher, spin coated with hexamethyldisilazane (J.T. Baker) followed by a positive photoresist (Shipley 1827; Rohm & Haas), patterned, and developed (MF-319 developer; Rohm & Haas). Electrodes were fabricated by depositing a 600 Å chromium layer by thermal evaporation. Glass microchannels (275 x 45 μm cross-section) were etched on glass wafers (borofloat, 500 mm thick, 15 cm diameter; Precision Glass and Optics). Assembled devices were wire bonded to a printed circuit board so that electrodes could be individually addressed.

3.6.2 Sample Preparation

Electrode dissolution experiments were carried out using histidine (Sigma-Aldrich), a 100 bp double-stranded DNA ladder (Bio-Rad), and sodium dithionite (Na2S2O4; Riedel-deHaën). Additional experiments were performed using λ-DNA (New England Biolabs) and a monodisperse 10 kb fragment (Fermentas). Test solutions were prepared in 50 mM histidine buffer. PCR products were generated using a KOD DNA Polymerase kit (Novagen) using a λ-DNA template (New England Biolabs) and primers obtained from Integrated DNA Technologies (forward: CTGAGGCCGGGTTATTCTTG; reverse: CGACTGGCCAAGATTAGAGA). Reactions were run for 30 cycles (95 °C, 10 s; 60 °C, 30 s; 72 °C, 30 s), and products were verifiedvby agarose gel electrophoresis.

3.6.3 Microdevice Operation and Data Analysis

Benchtop imaging was performed using an Axioskop-2 Plus microscope (Zeiss) interfaced with an Orca-ER digital CCD camera (Hamamatsu) and a halogen light source. A combination of Openlab automation software (Improvision) and ImageJ open source analysis software was used to acquire images and extract intensity data within a user-defined region of interest. Intensity profiles were normalized with respect to the initial and final values to facilitate comparison ($I_{\text{normalized}} = (I - I_{\text{final}})/(I_{\text{initial}} - I_{\text{final}})$; where I represents reflected intensity on an 8 bit scale of 0 to 255). The system's current was simultaneously received at 1 s speed by a digital multimeter (Keithley 2100).

CHAPTER IV

TUNABLE SYNTHESIS OF ENCAPSULATED MICROBUBBLES BY COUPLED ELECTROPHORETIC STABILIZATION AND ELECTROCHEMICAL INFLATION[*]

This chapter details the limitations of microbubble generation and storage can be overcome by exploiting an interplay between microscale electrokinetics and electrochemistry that simultaneously confines macromolecular encapsulants near an electrode surface while inflating them with gasses evolved from electrochemical reactions localized there. Stabilized microbubbles incorporating a remarkably broad range of morphologies produced by manipulating these fundamental processes. This versatility by generating dense clouds of small microbubbles that enable label-free detection of virtually any charged macromolecule (showed chapter II), and here by synthesizing larger discrete encapsulated microbubbles of tunable size will be displayed in this chapter.

4.1 Challenges, Limitations and Applications of Microbubbles

The inherent instability of microbubbles, gas-filled bubbles in the 1 – 50 μm size range, is a manifestation of the enormous Laplace pressures imposed by their highly

---

[*] Part of the data reported in this chapter is reprinted with permission from: Tunable Synthesis of Encapsulated Microbubbles by Coupled Electrophoretic Stabilization and Electrochemical Inflation by Huang, Y.-W., Shaikh, F.A., Ugaz, V. M., *Angewandte Chemie (International Edition)*, **2011**, 50, 3739-3743. Copyright [2011] by John Wiley & Sons.

curved interfacial topologies.[97-100] Macromolecular encapsulants (e.g., amphiphilic surfactants, lipids) are often employed as stabilization agents to counter these extreme conditions by bolstering the interfacial barrier against gas outflow[101-105], which is a more effective manner comparing to choose a low solubility filling gas. Ferrara's study[106] displays a free air microbubble completely dissolves in less than a second in a gas-saturated liguid (f = 1) condition. Using an insoluble gas, such as perfluorobutane (PFB, n-C_4F_{10}), to increase the water permeation resistance (~300 times greater than air) shows that the lifetime is several orders of magnitude higher than air but still less than a minute, which is far too short for using as a medical device (Figure 4.1 a). However, shell resistance estimated under degassed condition (f = 0) shows that microbubble lifetime is significantly enhanced, by five orders of magnitude, by the shell's diffusion impedance to PFB (Figure 4.1 b).

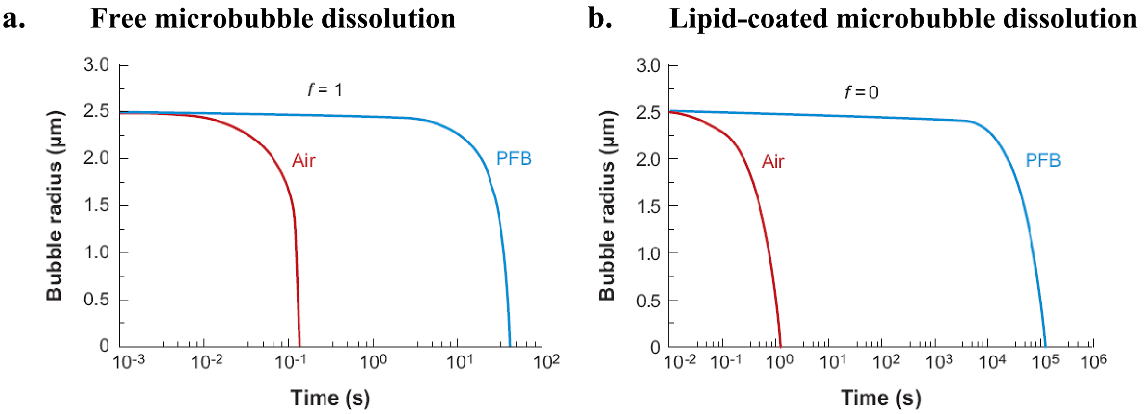

a. **Free microbubble dissolution**

b. **Lipid-coated microbubble dissolution**

Figure 4.1 Microbubble dissolution kinetics based on the modified Epstein-Plesset equation[106]. (a) Radius-time curves of a free microbubble composed of air and perfluorobutane (PFB) in a gas-saturated liguid (f = 1) condition. (b) Radius-time curves of lipid-coated microbubbles in degassed liguid (f = 0) condition. Copyright 2007 Annual Reviews.

The resulting stabilized microbubbles offer unique properties that have long been appreciated in the context of affinity separations (i.e., colloidal gas apherons[107, 108]), and more recently as contrast agents for ultrasound imaging[109, 110], as well as convenient platforms for tethering chemical compounds (receptors, antibodies, etc.) to enable highly specific *in vivo* targeting (either to precisely deliver drug payloads or to locally destroy surrounding tissue when ruptured by an applied ultrasonic field)[102, 106, 111, 112]. But despite these exciting applications, conventional batch-scale approaches used to produce encapsulated microbubbles are often relatively crude, based on mechanical agitation to entrain surrounding gas. Incredible progress has been made toward development of improved strategies at both the macro-scale (e.g., sonication and emulsification[113-116]) and micro-scale (e.g., flow focusing and T-junctions[117-121]), but a critical need still exists for approaches offering greater robustness to tune microbubble sizes and properties, as well as providing scalability from large-batches to single-dose amounts.

4.2 A Single Device for Tunable Size of Encapsulated Microbubble Preparation *via* Electrochemically Microfluidic Actuation

Conventional processing techniques to produce encapsulated microbubbles, such as sonication and high shear emulsification, provide high yield and low cost, but poor control over the microbubble size and uniformity. This is a problematic because microbubble behavior depends very strongly on the size. For instance, increasing the microbubble radius from 1 to 10 μm will change the resonance frequency of an unencapsulated microbubble from 4.74 to 0.35 MHz[122]. Moreover, microbubble size also affects the biodistribution and pharmacodynamics after intravenous injection, the bioeffects during ultrasound insonification and the gas release profile[123]. Microfluidic technologies, including flow focusing, T-junctions and coaxial electrohynamic atomization (CEHDA), have been mainly focused on the microbubble preparation with a high degree of control over the size and polydispersity[124] (Figure 4.2). These techniques, however, have relatively low production rates and usually need multiple devices to produce the required microbubble yields due to the restrictions on surfactant concentration and liquid viscosity[123, 125]. Additionally, the necessary of operation in the clean room condition increases the cost of lithographic etching equipment, while the subsequent running costs are comparatively low. Table 4.1 compares the microbubble yields obtained from using different microfluidic technologies, which is an important consideration from a commercial point of view. Even though the yield of traditional sonication would be expected to be higher ($\sim 1 \times 10^{10}$ bubbles min^{-1} or $\sim 1 \times 10^{7}$ bubble ml^{-1}[125]), the size distribution would be expected to be much broader (Figure 4.2) that the additional processing time is required to produce comparable monodispersible bubbles. Thus, it may be an acceptable trade-off in light of the development of microfluidic devices to produce uniform microbubbles.

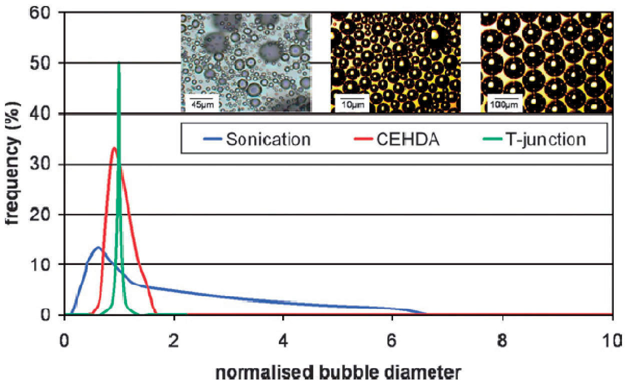

Figure 4.2 Typical size distributions of microbubbles prepared from a phospholipid suspension *via* sonication, coaxial electrohynamic atomization (CEHDA) and a microfluidic T-junction device[125]. Copyright 2008 The Royal Society of Chemistry.

Table 4.1 Comparison of microbubble yields obtained from different microfluidic technologies.

Preparation techniques	Schema	Microbubble mean diameter (μm)	Production rate (min^{-1})	Lifetime (hr)
CEHDA[114]	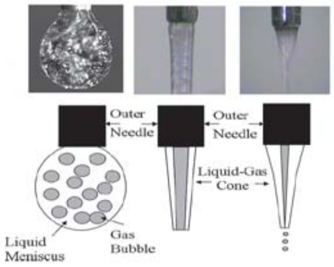	6.6μm ± 2.5	4 x 10^9	2.5
Flow Focusing[118]	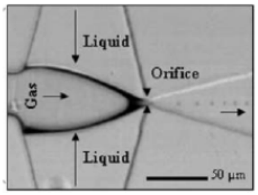	5μm ± 0.1	6 x 10^7	0.2
T-junction[120]	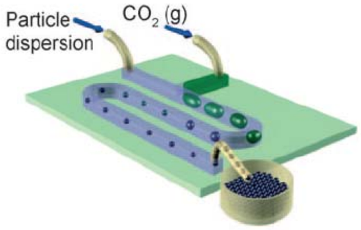	50	1.8 x 10^5	-

We proposed exploratory research to establish a new technique that will enable to synthesize a tunable size of encapsulated microbubbles by using a single microfluidic device. We have previously demonstrated a microfluidic device as abovementioned in chapter II, which can create a highly concentrated and compacted biomolecule film at the charged electrode surface and can be seen without chemical fluorophores labeled. This phenomenon has also been studied carefully in chapter II that charged biomolecules can become enriched to a very high concentration near an electrode surface while simultaneously experiencing infusion with electrochemically generated gasses to reflect injected light. A dramatic development is applying this same approach to synthesize encapsulated microbubbles by using ionic surfactants instead of DNA or protein (Figure 2.1 and Figure 4.4 d). Since the gas bubbles produce from water electrolysis, the theoretical bubble growth rate will depend on the supplied electric potential under the constant temperature and pressure based on the Faraday's law of electrolysis and the ideal gas law[72]. Therefore, we can regulate the supplied electric potential and the amplitude/duration to control the microbubble size and trigger the gas filled bubbles to depart from the electrode surface. In addition, the bubble growth process in polymers has been observed highly depended on the polymer concentration[126]. Thus, we can also adjust the concentration of surfactant concomitantly to produce tunable size of encapsulated microbubbles for medical applications.

4.3 Surfactant-Coated Microbubbles Formation *via* Different Power Strategy

We demonstrate this new approach by using ionic surfactants, such as sodium dodecyl sulfate (SDS) and dioctyl sodium sulfosuccinate (AOT), to make it possible to produce discrete stabilized microbubbles. Since SDS forms anionic micelles and AOT forms cationic micelles when the concentration above the critical micelle concentration (CMC) and electrolysis of water is responsible for the bubble formation, we expect to see oxygen filled SDS shell bubbles at the anode and hydrogen filled AOT shell bubbles at the cathode. Theoretically, oxygen and hydrogen start to be produced at the threshold potential of ~ 1.3 V. The practical potential, however, observed to generate microbubbles is higher above ~2.5 V both on SDS and AOT cases, which is referred to as overvoltage in electrochemistry commonly examined due to nonequillibrium kinetics of electron transfer, especially when a gas phase is present[127]. In addition, the speed and type of microbubble formation also depend on the supplied potential. At the bulk conditions slightly below the CMC, it takes longer time and higher potential to produce the locally oversaturated gases and form bubbles (Figure 4.3 a). When the condition reached the CMC, the aggregates of gas filled micelles is seen apparently at the charged electrodes within a minute (Figure 4.3 b). At a later time, the locally oversaturated gases begin to coalesce into larger bubbles after several minutes (Figure 4.3 c). At the condition greater than the CMC (~ 10x CMC), encapsulated microbubbles are continuously produced. To precisely control the size of microbubbles, we have to manipulate the amplitude and frequency of the supplied potential.

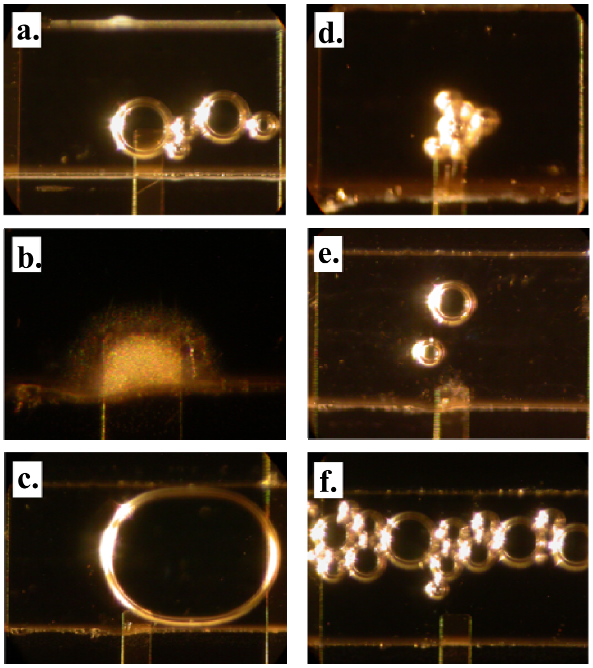

Figure 4.3 (a) SDS microbubbles are formed under the concentration slightly below the CMC at higher potential and longer time (10^{-1} CMC, 3 V applied for 15 min). (b) Gas filled SDS micelles are compacted at the anode under the CMC (1 CMC, 3.5 V applied for 60 s). (c) Larger bubble forms due to locally oversaturated gases coalescence at a longer time applied (1 CMC, 3.5 V applied for 5 min). (d) View of the moment of SDS microbubble formation at the concentration great than the CMC (10 CMC, 3 V applied for 20 s). (e) Discrete SDS microbubbles are produced by applying an initially higher potential then following a lower potential at the concentration above the CMC (10 CMC, 5 V applied for 15 s, then switched to 3 V applied for 30 s). (f) Large amount of discrete SDS microbubbles are produced by a low and then a higher potential applied at the concentration above the CMC (10 CMC, 3 V applied for 60 s, then switched to 5.5 V applied for 50 ms to trigger release). Scale: all electrodes are 50 μm wide horizontally.

Immediately terminating the potential at the flash of microbubbles formed could produce tiny bubbles but no bubbles release to the bulk solution (Figure 4.3 d), which is not useful for medical applications. Two further strategies have been applied to our study for triggering bubbles release and creating size-controlled microbubbles. Since the charged molecules compact to the working electrodes immediately and gases continuously produced by water electrolysis, we applied a higher potential in a very short time (~ several seconds) to speed up the tiny bubble formation. Then, a lower potential was applied to keep on the electrochemical gases producing for a while to balance the gases inside and outside the micelles till the equilibrium accomplishment (Figure 4.3 e). An advanced approach is to operate at regular potential we used to for surfactant migration and compaction, and then to apply a higher potential in a very short time (~ several milliseconds) for increasing the speed of electrochemical gases production to release the encapsulated microbubbles into bulk solution (Figure 4.3 f). The former approach produces more uniform microbubbles, but the latter approach provides larger amount of microbubbles.

4.4 Surfactant-Coated Microbubble Formation under Different Surfactant Concentration

Gas bubble generation in polymers is more complicated than the corresponding problems in a pure substance[128]. Deng P. *et al*.[126] investigated microbubble formation in DNA solution, which shows the microbubble growth process, including bubble diameter, lifetime and nucleation work, is highly related to DNA concentration and viscosity. Here, we applied this new approach in the presence of an anionic surfactant sodium dodecyl sulfate (SDS) instead of DNA to produce discrete stabilized microbubbles. Our study also confirmed that the surfactant concentration dominate the microbubble formation. At bulk conditions below the critical micelle concentration (CMC; a value of 8.3 mM was assumed[129]), surfactant molecules become compacted at the anode in the same way as the DNA behavior described in chapter II but do not attain a sufficiently dense packing to produce strong surface reflectivity (Figure 4.4 a). Under conditions in the vicinity of the CMC, the electrode surface is initially decorated by a field of reflective spots sparsely arrayed against a dark background, transforming into a dense halo at later times and/or higher potentials (Figure 4.4 b). At still higher surfactant concentrations (~10x CMC), a more dramatic change occurs whereby discrete encapsulated microbubbles are continuously produced and released into the bulk environment (Figure 4.4 c). This behavior can be explained by noting that above the CMC micelles from the bulk solution experience compaction at the electrode surface, as opposed to the individual surfactant molecules that predominate at lower concentrations (Figure 4.4 d). The relatively large size of these micellar structures imposes a steric barrier against adoption of the densely packed arrangement necessary to generate high reflectivity. But because they are immobilized in close proximity to the electrode surface, the compacted micelles become infused with the electrochemically evolved gas, thereby providing a driving force for production of encapsulated microbubbles. The size and quantity of the resulting microbubbles can be manipulated by adjusting the amplitude and duration of the applied potential, which simultaneously governs the underlying electrophoretic and electrochemical processes.

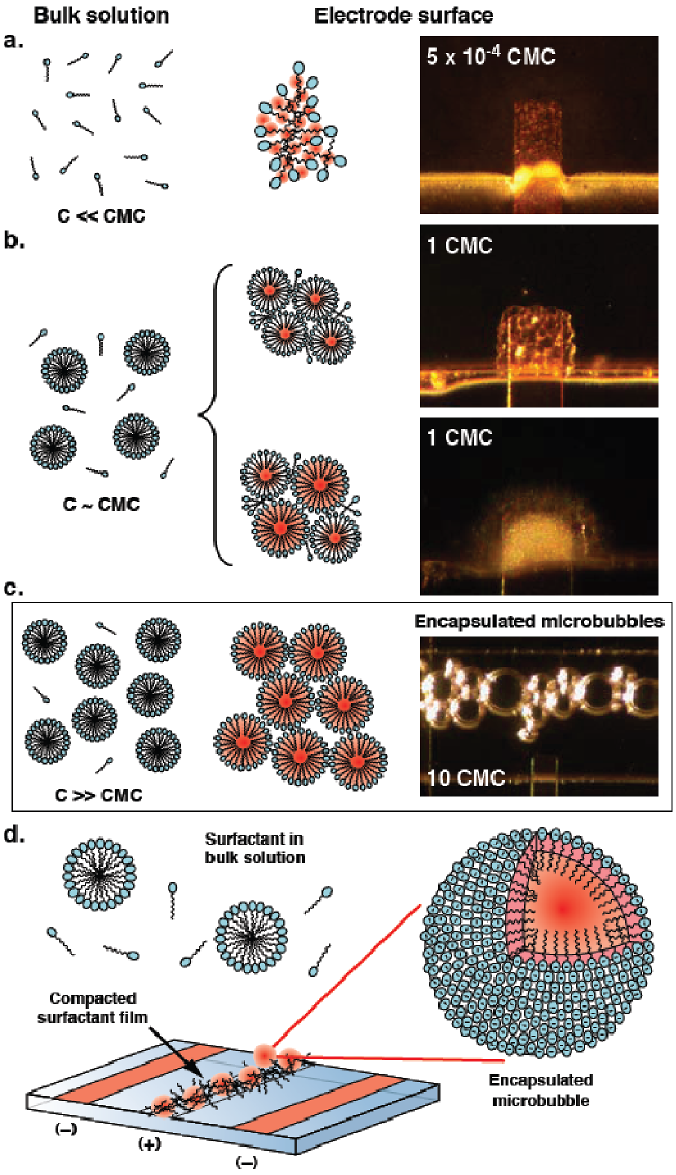

Figure 4.4 (a) Only weak surface reflectivity is evident at the anode when the surfactant concentration is below the CMC (2.8 V applied for 90 s). (b) Bright spots appear in the vicinity of the CMC, transforming into a dense opaque halo at higher potentials and/or longer times (top: 3 V applied for 90 s; bottom: 3.5 V applied for 60 s). (c) Discrete encapsulated microbubbles are produced at bulk concentrations above the CMC (3 V applied for 60 s for bubble formation, then switched to 5.5 V for 50 ms to trigger release). (d) Under these conditions, compacted micelles confined at the electrode surface become infused with electrochemically generated gasses. All surfactant solutions contain SDS in 50 mM histidine. Scale: all electrodes are 50 μm wide horizontally.

Dioctyl sodium sulfosuccinate (AOT) is an anionic surfactant as well which is soluble both in polar and apolar solvents but forms reverse micelles with a unique cationic surface (Figure 4.5 a) and has been regarded recently for encapsulated proteins[130, 131]. When mixed with water, AOT dissolves if its concentration is less than the CMC (a value of 2.24 mM was assumed[132]). For concentrations above the CMC, however, aggregates in equilibrium with individual surfactant molecules are formed. We also examined AOT by using our new approach to produce stabilized microbubbles. At bulk conditions closed to the CMC, a longer time (~ 15 min) has to be taken to enable micelle cloud visible at the cathode comparing to the similar condition of SDS (Figure 4.5 b). A denser surface reflectivity shows on the cathode under the slightly higher concentration above the CMC (~ 5x CMC) while larger coalescent bubbles form at higher potentials and longer times (Figure 4.5 c). Under the concentration far above the CMC (~ 20x CMC), aggregates is evident and a halo forms around the cathode due to the repellent from locally gases (Figure 4.5 d). Then, non symmetrical bubbles form at longer times (~ 10 min) with bigger diameters, which are not to be compared with the SDS bubbles (Figure 4.5 e) because the hydrophobic tails displayed on the surface of reverse micelles weaken the capability to stabilize gases. Previous studies demonstrated that bubble size and collapse process are retarded at high DNA/polymer concentrations due to increased viscosities[101, 104, 126, 133]. Therefore, we added glycerol and increased the CMC of SDS to raise the bulk viscosity and generated continuously discrete microbubbles with comparable uniform sizes (Figure 4.5 f), which provides a new strategy to manipulate monodispersible bubbles beyond adjusting the applied potential and surfactant concentration.

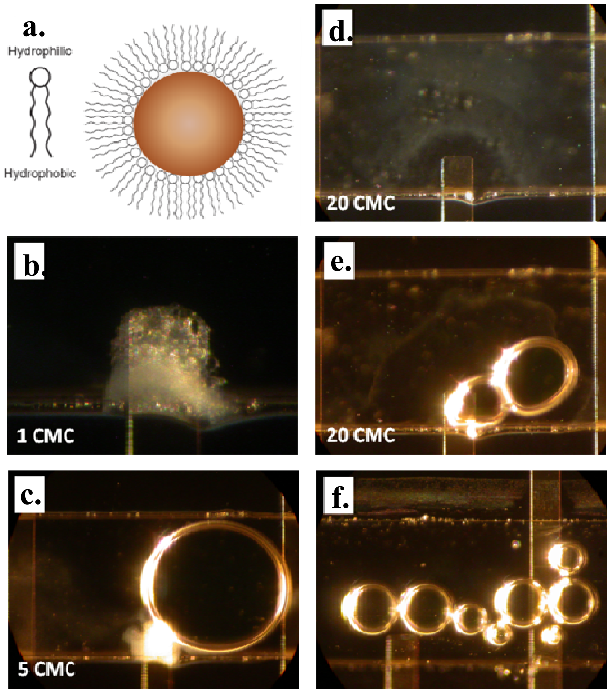

Figure 4.5 (a) Illustration of the reverse micelle forming and resulting reverse micelle particle. (b) Gas filled AOT micelles clouds are apparent at cathode in the vicinity of the CMC (1 CMC, 3 V applied for 15 min). (c) Denser AOT micelles clouds show at cathode while a larger bubble forms due to locally oversaturated gases coalescence when a longer time applied with the concentration slightly above the CMC (5 CMC, 3.5 V applied for 16 min) (d) AOT aggregates is evident in the bulk solution when the concentration is far above the CMC and a halo forms while the supplied potential applied to the cathode (20 CMC, 3 V applied for 20 sec). (e) Larger non symmetrical bubbles are produced under the concentration far above the CMC for a longer time potential applied (20 CMC, 3 V applied for 10 min). (f) Discrete uniform microbubbles are produced at a high viscosity solution prepared from glycerol and high concentration of SDS (30% glycerol and 40 CMC of SDS, 3.3 V applied for 150 s, then switched to 2.5 V applied for 30 s). Scale: all electrodes are 50 μm wide horizontally.

4.5 Materials and Methods

The design, construction, and operation of the microfabricated electrode array devices have been described in chapter II. Sodium dodecyl sulfate and dioctyl sodium sulfosuccinate (electrophoresis grade; Fisher) solutions were prepared in 50 mM histidine buffer. The encapsulated microbubbles produce process was imaged using an Axioskop-2 Plus microscope (Zeiss) interfaced with an Orca-ER digital CCD camera (Hamamatsu). The supplied potentials were provided by Agilent E364xA dual output DC power controlled by LabVIEW (National Instruments) to precisely regulate the amplitude and duration.

CHAPTER V

APPLICATION OF ON-CHIP ELECTRODE ARRAYS FOR ELECTROKINETICALLY ACTUATED PROTEIN CRYSTALLIZATION

This chapter displays an innovation we exploited for easy and rapid protein crystallization *via* electrokinetic actuation which simultaneously pre-concentrate protein molecules and migrate ions either to accelerate the process or to control the directions of the movement of certain ions. Protein crystallization is the bottleneck to obtain for the 3-D structural analysis which normally requires days to weeks from a concentrated pure solution. Here, we used hen egg white lysozyme as first study to demonstrate an on-chip method that is possible to achieve single crystals using small power (< 2 V) within a short timescale (1-2 hours) and without previous purification that provides capabilities for a straightforward interface of *in-situ* x-ray diffraction analysis to be performed as the protein formed inside the system.

5.1 Challenges and Conventional Methods of Protein Crystallization

Protein crystallization was first carried out 170 years ago[134]. Early workers focus on purification to establish the nature of proteins and their role in catalysis until the x-ray diffraction developed to provide structural information at atomic-resolution in the 1950s[135]. Today, we understand that protein biomarkers play a critical role in biomedical screening, disease detection, identification of therapeutic targets, and monitoring treatment efficacy. But transformative advances in molecular-level technologies for biomarker analysis and discovery are still necessary in order to overcome the barriers hindering development of more effective disease- and patient-specific therapeutics. While computational methods have greatly improved the capability to predict structure-function relationships, the sheer number of interactions involved pose daunting challenges that make it essential to conduct parallel experiments so that the predictions can be validated and refined[136, 137]. In addition to fundamental biological insights, protein structure determination is indispensable in the pharmaceutical industry where it plays a key role in guiding the development of new drugs and therapeutic compounds[138]. Knowledge of the detailed structure associated with an active site governing protein activity provides a natural target for design of compounds to regulate metabolic pathways corresponding to the disease or infection of interest. This knowledge in turn makes it possible to develop new drug compounds that influence such behavior. Finally, high throughput structural characterization methods are urgently needed to perform population-scale studies aimed at obtaining data to serve as inputs for structural biology and structural genomics research efforts[139].

5.1.1 The Challenges

Why are proteins generally more difficult to crystallize than small molecules and inorganic compounds? The main reason may be protein crystals have far few contacts in proportion to their molecular weight and are very weak even though the protein-protein contacts are comparable in binding energy to those between small molecules[135]. In addition, it is very difficult to purify proteins even with 100% chemical purity and each individual molecules exist different conformational states which even militate against formation of highly ordered crystals. Furthermore, the diversity of chemical groups involve in the contacts of protein crystals that imply slight changes in pH, ionic strength, temperature, or concentration of an auxiliary ion or molecule may strongly influence crystallization processes.

Currently, x-ray crystallography is the primary experimental tool employed to understand the fundamental processes that govern how proteins fold and assemble into well-defined structures because it delivers the molecular-scale resolution needed to elucidate relevant morphological details. But diffraction methods critically depend on the ability to produce high-purity crystal samples. Conventional crystallization processes are also inherently slow, involving suspending a protein of interest in an appropriate buffer solution and progressively increasing its concentration until supersaturated conditions are reached that favor nucleation and growth[140]. In order to drive the crystallization process, it is necessary to bring the protein laden solution into a supersaturated state. But the non-equilibrium nature of the supersaturation regime makes it challenging to precisely control, and the situation is further complicated by the wide range of parameters that can be varied. All the challenges point to the need for new methods that can enable protein crystallization to be performed rapidly and at greatly reduced cost.

5.1.2 Conventional Methods of Protein Crystallization

The present state-of-the-art in protein crystallization can be understood by considering the range of supersaturated conditions that can be probed using various approaches (Figure 5.1)[140]. In microbatch methods (Figure 5.1, line i), the starting point is a supersaturated solution with an initial protein concentration just inside the nucleation zone where crystallization is favored. In practice, it is desirable to reduce the concentration into the metastable region (where a phase transition can occur but may not be thermodynamically favored) as soon as crystallization begins in order to maximize the size of the crystals produced. Robots can dispense thousands of microbatch trials down to nanoliter volumes that can be harnessed for screening, fine-tuning and optimization experiments[138]. Vapor diffusion methods (Figure 5.1, line ii) begin with an undersaturated protein solution that is brought to supersaturation by gradual evaporation. The most common variation is the hanging drop approach. A broader range of metastable conditions can be explored, but the rate of concentration change decreases with time. In addition, the different trials are not easily transportable that a comparably large minimum quantity of protein may be required[138]. Dialysis method (Figure 5.1, line iii) provides a way to further tailor exchange between the protein solution and a precipitant across a semi-permeable membrane but requires expertise. Free interface diffusion (Figure 5.1, line iv) allows more complex phase trajectories to be followed by establishing a concentration gradient between the protein and precipitant that makes it become the most powerful as a fine-tuning screening technique. In all procedures, timescales of days to weeks are required to obtain diffraction quality crystals, and the methodology for zeroing-in on ideal crystallization conditions is still hit or miss.

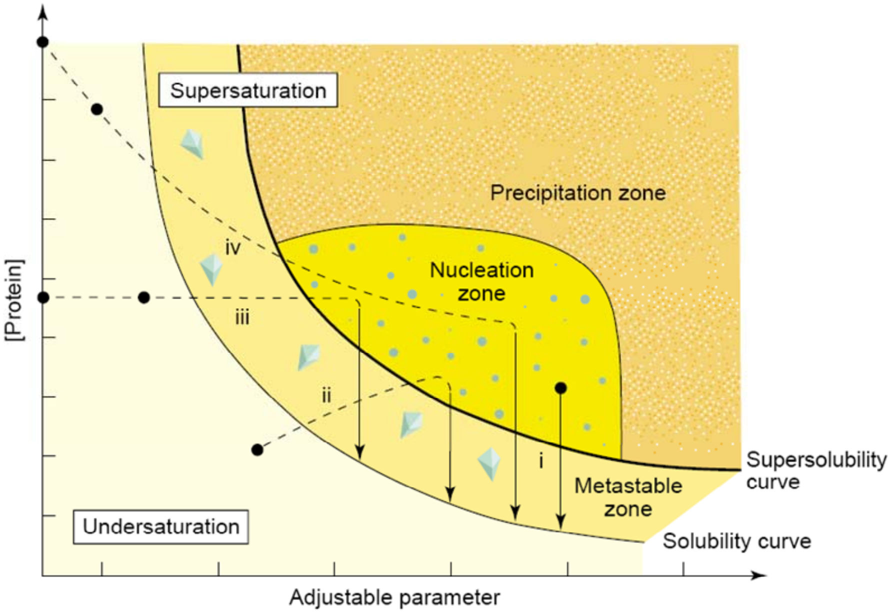

Figure 5.1 Simplified phase diagram for protein crystallization[140, 141]. Adjustable parameters include precipitant or additive concentration, pH and temperature. The overview of traditional crystallization methods is represented: (i) microbatch, (ii) vapor diffusion, (iii) dialysis and (iv) free interface diffusion. Each involves a different route to reach the nucleation and metastable zones, and all require long timescales (days to weeks). Copyright 1998 International Union of Crystallography.

Microfluidic methods have proven to be a key enabling technology to address some of these barriers, most notably by increasing throughput *via* massive parallelization so that more trials can be performed simultaneously[142, 143]. Some adaptations also permit *in-situ* x-ray diffraction analysis, eliminating the need to harvest and manipulate the crystals. But in the majority of these formats, the fundamental mechanism by which the crystallization process is executed remains identical to the macroscale, with the exception that the size of the container encapsulating the crystallization solution is greatly reduced[144-153]. Timescales of hours to days are generally required.

5.2 New Strategy for Protein Crystallization Using an Internal Electric Field

High-quality single crystals are extremely demanded for x-ray crystallography and they need a well-controlled nucleation process. To avoid uncontrolled nucleation, researchers often use seeding techniques to induce crystallization from metastable solutions, in which nucleation does not occur[154]. Other studies have considered a diversity of physicochemical parameters to control the nucleation phenomena, including using magnetic fields[155, 156], high-pressure[157, 158], ultrasonic fields[159], and electric fields[160-175]. The basic idea behind all of them is to locate the system in the nucleation area (Figure 5.1) and to provide energy for spontaneously producing the first nucleation. Among them, applying electric fields is the most direct and easiest approach.

The electric-field-induced protein crystallization can be classified into external and internal electric fields, depending on whether the electrodes are directly in contact with the protein solution (Figure 5.2). Normally, external electric field trials require high fields of up to 7.5 kV cm^{-1} [160-162, 166] but no chemical reactions occurring on the electrodes. The first study of internal-electric-field-induced protein crystallization was introduced by Chin *et al* [176], called electrophoretic diffusion, to crystallize a labile enzyme (human placental estradiol 17β-dehydrogenase) that could not been crystallized by other methods with a relatively small electric field (initially 15 - 20 V cm^{-1} and then

30 - 40 V cm^{-1}) and completed in 24 - 48 hours. Furthermore, Moreno's group [168-170] demonstrated a new technique, electrochemically assisted protein crystallization, to crystallize lysozyme at cathode and to obtain amorphous phase at anode with ~1 V and ~24 hours. Generally, applying electric fields influence the orientation of protein molecules that speeds up the nucleation velocity and reduces the induction time, but a supersaturated and metastable protein solution is still required for these procedures.

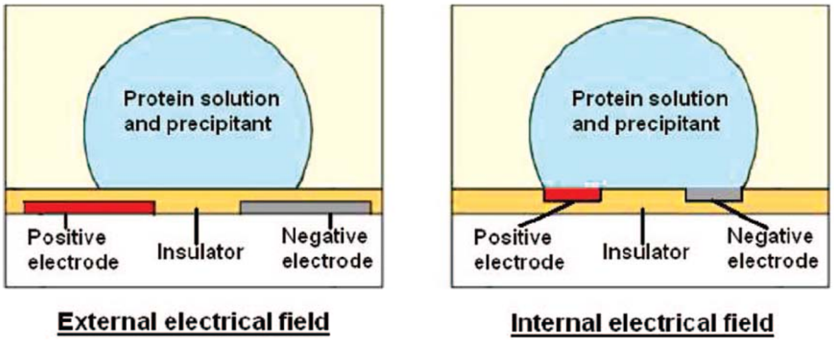

Figure 5.2 Experimental set-ups of a crystallization cell using an external and an internal electrical field, respectively[168]. For the external-electrical-field-setting, the electrodes are not in contact with the solution containing the interested proteins. On the contrary, the electrodes are directly in contact with a protein solution, called internal-electrical-field-setting. Copyright 2008 American Chemical Society.

We propose exploratory research to establish a transformative and fundamentally different approach to direct the protein crystallization process from un-purified and un-concentrated solutions by applying an internal electric field (Figure 5.3 a). Instead of increasing protein concentration throughout the entire bulk volume using evaporation, we propose to use microfabricated electrode arrays to increase protein concentration to extremely high levels within a very thin layer at the electrode surface (Figure 2.4). In this way, we can also repeat compaction for multi-dimensional concentration and supersaturated conditions favorable for crystallization can be quickly established within this enriched region (Figure 5.3 b). Since the process is actuated electrokinetically, it is also possible to exert a much finer level of control over crystallization than is achievable using evaporation. This would allow a wider range of parameter space within the supersaturated regime to be explored, including conditions that are currently impossible to access by evaporation. Even greater control is possible by superimposing a hydrodynamic flow of precipitant or solute over the collected protein layer to allow harvesting of desired crystals and re-suspension of undesired condensates to be performed on the fly. This method can be straightforwardly coupled with x-ray diffraction to permit real-time analysis of crystal structure.

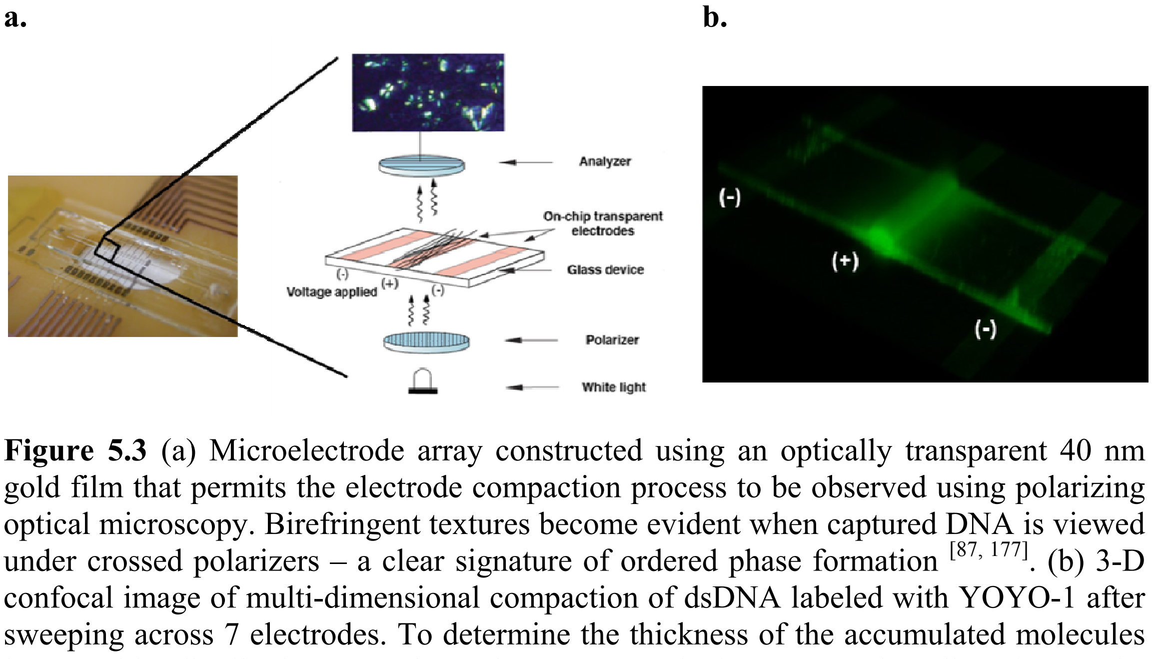

Figure 5.3 (a) Microelectrode array constructed using an optically transparent 40 nm gold film that permits the electrode compaction process to be observed using polarizing optical microscopy. Birefringent textures become evident when captured DNA is viewed under crossed polarizers – a clear signature of ordered phase formation [87, 177]. (b) 3-D confocal image of multi-dimensional compaction of dsDNA labeled with YOYO-1 after sweeping across 7 electrodes. To determine the thickness of the accumulated molecules layer and its distribution over electrode surface to obtain cross-section slice view of the captured molecules in the vicinity of the electrode surface.

5.3 Preliminary Studies of Lysozyme Single Crystals

In order to demonstrate our proposed concept, we performed preliminary studies to demonstrate its feasibility using hen egg white lysozyme as a model protein (Figure 5.4). All experiments were performed using a commercial crystallization kit. A freshly prepared solution was injected into a glass microchannel with gold electrodes and the loading ports were sealed to prevent evaporation (Figure 5.3 a). A 2 V potential was then applied between electrodes in the array. Within 1 min, formation of a dense halo of compacted protein around the outer perimeter of the cathode was observed. Next the voltage switched off to release the compacted protein zone back into the bulk solution. In the absence of the electric field, large single protein crystals appeared within ~1 hour. Parallel negative control experiments in which the electric field was not applied did not produce crystals after several days.

These results can be explained by considering the interplay between electrophoretic transport of the protein macromolecules and small-molecule ionic species present in the solution. When the potential is applied, the small-molecule species are likely to exhibit a higher mobility, resulting in rapid establishment of a dense cloud around the electrodes. In this stage, crystallization is suppressed due to this non-equilibrium ionic environment and/or conformational changes in the protein near the electrode surface. When the potential is switched off, the compacted protein halo begins to disperse and re-enters more favorable ionic conditions. The protein concentration within this front remains high enough to lie within the supersaturated regime, enabling it to act as a trigger for crystallization, thereby explaining the formation of crystals at some distance away from the cathode. The electric field is not applied during the crystallization process itself, it serves as an initial pre-concentration step for protein molecules and also provides directions of the movement of certain ions to accelerate the crystallization process. Although these are extremely preliminary results, we believe that the good repeatability we have observed with the process as depicted in Figure 5.4 demonstrates that this crystallization approach is feasible as a reproducible trigger for rapid protein crystallization. The results of the real-time x-ray diffraction for the crystal structure analysis did not apply to our work yet, but the ability to form diffraction quality crystals in the presence of an applied electric field has been previously demonstrated in the context of conventional macroscale methods [165, 170, 172, 175]. Thus, we believe this new technique has capability to enable protein to be rapidly crystallized and their structure can be characterized using *in-situ* x-ray diffraction analysis.

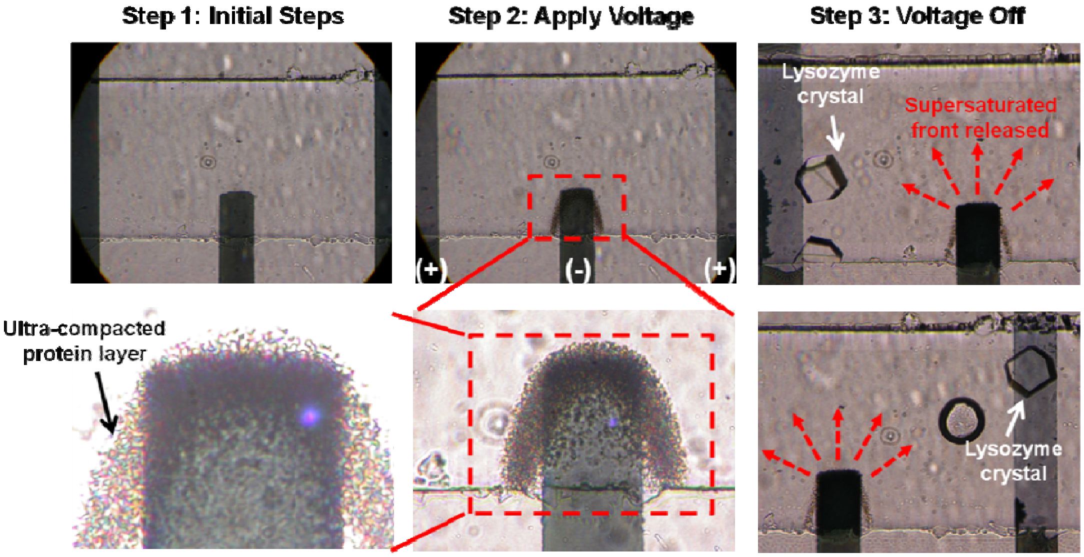

Figure 5.4 Preliminary results demonstrating feasibility of forming lysozyme single crystals by electrokinetic actuation. Within one minute after application of a 2 V potential between electrodes, a dense ultra-compacted protein layer becomes evident surrounding the capture electrode. The densely packed protein within this "halo" are then released when the voltage is switched off, and the resulting compacted front returns to equilibrium ionic conditions while remaining in a supersaturated state for nucleation of crystallization. Large single crystals are formed within 1-2 hours. Scale: all electrodes are 50 μm wide horizontally.

5.4 Materials and Methods

The design, construction, and operation of the microfabricated electrode array devices have been described in chapter II. Transparent gold electrodes for experiments performed under transmitted light illumination were fabricated by depositing a 50 Å layer of chromium followed by a 400 Å layer of gold using a thermal evaporator. Experiments were performed using a commercial crystallization kit (HR7-108; Hampton Research) to prepare a 50 mg/ml protein solution in a crystallization buffer containing 30% w/v polyethylene glycol monomethyl ether 5,000, 1.0 M sodium chloride, and 50 mm sodium acetate trihydrate pH 4.5.

CHAPTER VI

CONCLUSIONS AND FUTURE WORK

6.1 Summaries and Conclusions

In this study, we developed a versatile platform with addressable microfabricated electrode arrays (Figure 6.1). With slight modification of the electrode materials, this platform can provide multi-applications with small electrical power consumption (1–3 V) *via* the microscale interplay between electrophoresis and electrochemistry.

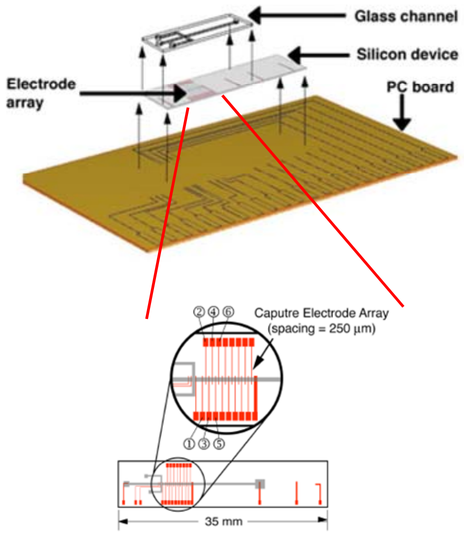

Figure 6.1 Illustration of microdevice construction and microfabricated electrode arrays. Diagram is reproduced from Shaikh and Ugaz (2006) [59].

Microfabricated platinum electrode arrays display the capability for a real label-free detection to avoid the drawback of conventional labeling methods. This new technique allows biomolecules (DNA, proteins) and other charged analytes to be detected in free solution *via* the surface reflectivity of stabilized microbubbls produced from the electrolysis of water, which has a threshold of ~1.3 V. This effect is reversible that enables for the subsequent reaction, and can be tuned to localize compaction by adjusting the buffer pH relative to the sample's isoelectric point. The interplay between microscale electrokinetics and electrochemistry can also be harnessed to simultaneously confine macromolecular encapsulants near an electrode surface while inflating them with gasses evolved from the electrolysis of water localized there for imaging and targeted therapeutics.

Microfabricated chromium electrode arrays demonstrate another application of unlabeled detection by monitoring electrode degradation under ordinary white-light illumination. The governing chemical and physical processes of the on-chip chromium electrode dissolution are relatively complicated but highly compositional- and size-dependent, which provides a promising further opportunity for a real-time PCR detection application. In addition, preliminary studies also displayed the feasibility of smartphone-based imaging with an Apple iPhone 4S using the *iFast Pro* camera app. The use of the existing hardware and/or software architecture of cell-phones to improve healthcare is a recently emerging topic since the world-population of at least one cell-phone subscription has been expected to further increase up to ~ 90% by 2015[178]. Our approach can be generically applied to a variety of smartphones, and is likely to become increasingly robust as imaging capabilities continue to rapidly improve, which will greatly expand the use of advanced diagnostic competences.

Protein crystallization has been demonstrated by electrokinetic actuation simultaneously to pre-concentrate protein molecules and to migrate the movement of certain ions that enables to obtain single crystals in a short timescale (1-2 hours) and without previous purification. The use of transparent electrodes is essential to allow the observation of the crystallization processes under transmitted light through crossed polarizers and to provide the capabilities for a straightforward interface of *in-situ* x-ray diffraction analysis.

6.2 Future Work

Although we have successfully built a diversified platform for simply unlabeled detection, tunable synthesis of encapsulated microbubble and rapid protein crystallization, advanced investigation will allow us to precisely control this technique and to expand the abilities for multiple user communities. The following are recommended to further improve the performance and capability of our system.

6.2.1 An Integrated Hydrodynamic Flow System

The ability to transport and manipulate solutions in microchannels is one of the fundamental issues of microfluidics. Electroosmotic flows have been used to transport fluid at the microscale, but they are sensitive factors such as buffer properties, surface composition, and the electric field. Quake's group[179] has developed a simple method to fabricate pneumatically activated valves on the basis of soft-lithographic procedure, which made a significant contribution. We have preliminarily followed the same principles of the diaphragm valves[180] to create two layer pneumatic microvalves (Figure 6.2 a, b) by using polydimethylsiloxane (PDMS), which can be operated as an efficient micropump by controlling the open/close of the microvalves *via* computer software (LabVIEW, National Instruments) adjusting the pressure in a displacement chamber on the pneumatic layer (Figure 6.2 c). We also have developed a clipped approach using transparent acrylic to incorporate the PDMS layer to our silicon/glass electrode array chips (Figure 6.3). This design solves the nonspecific absorption problem of PDMS and allows the silicon/glass chips to be reusable after cleaning. This micropump has been tested to inject dsDNA labeled with YOYO-1 for performing the buffer exchange (Figure 6.4). Even though this is a very beginning of the attempt, we believe further improvement of this microfludic system will have a better performance to collect targeted samples, to harvest desired crystals, and to continuously produce encapsulated microbubbles. In addition, an integrated on-chip microfluidic system as we endeavor to build up can also be used as a basic building block to construct highly sophisticated micro-analysis systems in the future.

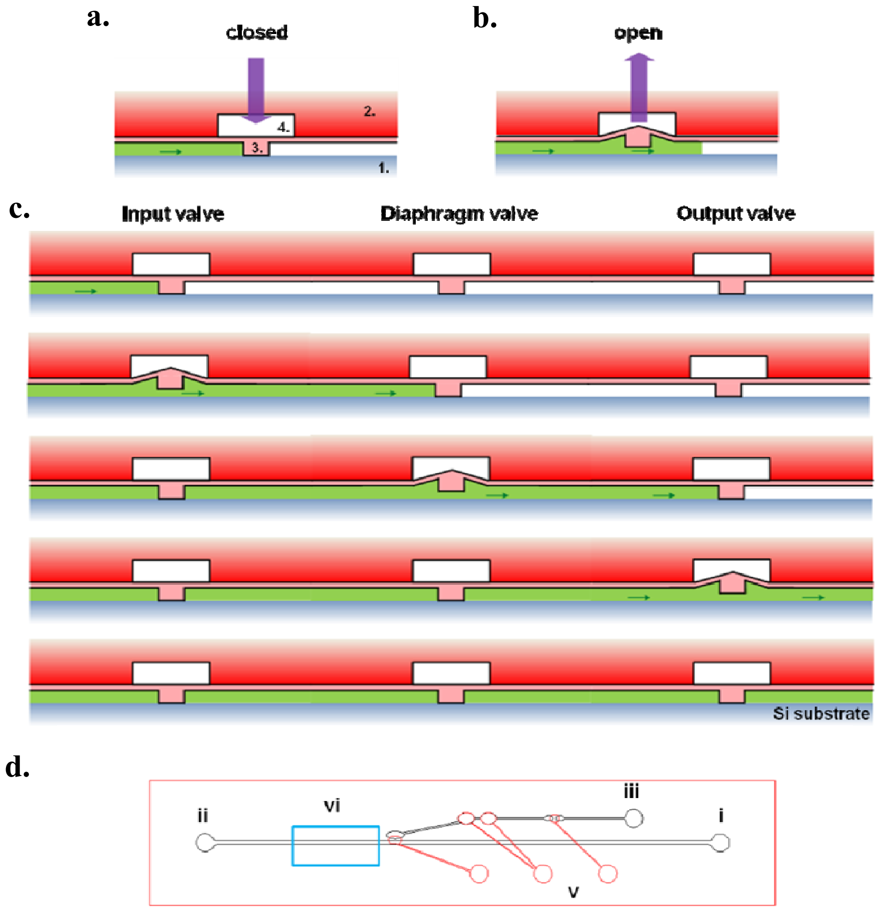

Figure 6.2 (a-b) Cross-sectional view of two-layer PDMS membrane valve. The valve is operated as closed when a positive pressure provided (a) and open when a negative pressure provided (b) (1: silicon substrate; 2: PDMS pneumatic layer; 3: PDMS microfludic channel; 4: displacement chamber). (c) Schematic diagram of micropump. The pumping involves cycles of three steps: open input valve and close diaphragm and output valves; open diaphragm valve and close input and output valves; open output valve and close input and diaphragm valves. (d) Schematic diagram of three microvalves and microfludic channel (i: buffer inlet; ii: buffer outlet; iii: sample injection; iv: electrode array; v: microvalves).

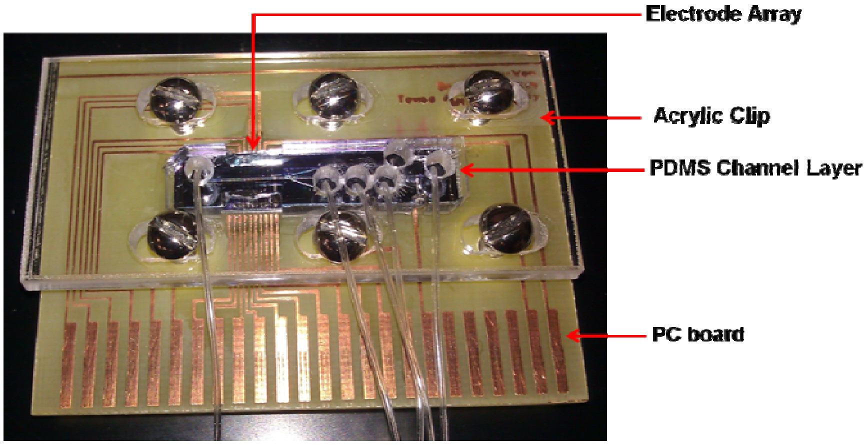

Figure 6.3 Illustration of acrylic clip and microdevice construction.

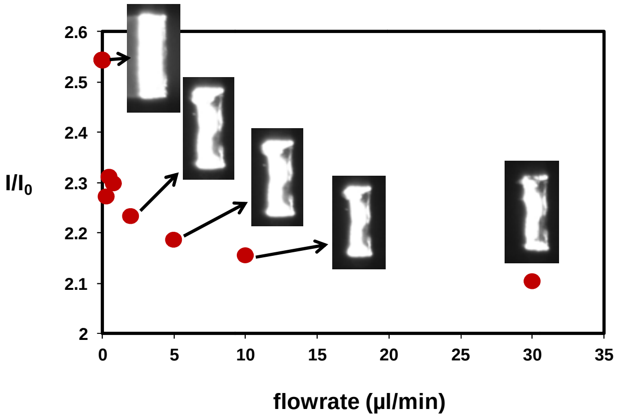

Figure 6.4 Preliminarily results demonstrating the performance of the micropump operation. Experiments were performed using a 100 bp dsDNA ladder initially at 10 µg/mL in 50 mM histidine with 10 %v/v β-mercaptoethanol, 2.0 V applied to capture the hydrodynamic flow DNA samples. The flow was setting from right to left on the diagram. Captured DNA samples wash away slowly with the increase of the flowrate based on the observation of the intensity decreasing. Scale: all electrodes are 50 µm wide horizontally.

6.2.2 Fundamental Characterization of Gas Evolution

Electrolysis of water (with a threshold of ~1.3 V) is the main reaction of our system to dominate the performance of label-free detections and synthesis of encapsulated microbubbles. Therefore, the investigation of the fundamental characterization of oxygen/hydrogen evolution on the electrodes will allow us to precisely control this microfabricated system. Simultaneous real-time measurement of reaction current as a function of time can provide an idea of total electrical charges between the electrochemical reactions. Assuming electrolysis of water is the only applied coulometric gas generation reaction, which occurs if a current is sent through two noble metal electrodes placed in water in terms of the following mechanism.

Anode: $2H_2O \rightarrow 4H^+ + 4e^- + O_{2\,(g)}$

Cathode: $2H_2O + 2e^- \rightarrow 2OH^- + H_{2\,(g)}$

Based on this reaction and assuming that all generated gases (O_2 and H_2) evolve in the form of gas bubbles, it can be derived that the total amount V_{gas} (m^3) depends linearly on the electrical charges Q (C).

$$V_{gas} = V_{H_2} + V_{O_2}$$

$$V_{H_2} = \frac{c}{2}$$

$$V_{O_2} = \frac{c}{4}$$

$$c = \frac{V_m}{F}\int i(t)dt = \frac{V_m Q}{F}$$

Where V_{H_2} and V_{O_2} are hydrogen and oxygen gas volumes, respectively; F is Faraday's number (96.49 x 10^3 C/mol); V_m (m^3 mol^{-1}) is the molar gas volume (24.7 x 10^{-3} m^3 mol^{-1}, at 25 ℃ and atmospheric pressure); and $i(t)$ (A) is the current as a function of time. Thus, we may be able to control the amount of gases produced from the reactions and to develop a micro-dosing system in the future. In addition, using a high-speed and high-resolution camera can help us to demonstrate the influence of microbubble size with the electric field[95, 181] (amplitude, frequency), bulk solution (type, ionic strength, and viscosity[133]), electrode material and roughness[96], and encapsulating materials[182] to establish the optimal conditions.

6.2.3 Chemical and Physical Mechanisms of Chromium Electrode Dissolution

The underlying chemical and physical processes governing the chromium electrode dissolution are relatively complex, but undoubtedly the changes of local pH and ionic environment by electronically active reactions play an important role. Deep investigation can help us to understand and develop the mechanisms and to optimize the performance of the micro-system. pH indicator provides a rough variation of the background electrolytes[183] but it may be difficult to observe clearly under a micro-surroundings. Computational simulation may be a good tool to develop the local pH distribution and to understand the effect of buffer protonation under the local mass transportation and chemical reactions [184-186]. In addition, computational simulation can also build up the profile of DNA compaction on the polarized electrodes and know prior to any active microarray layout design to optimize the performance[187].

6.2.4 Advanced Studies of Protein Crystallization

A mathematical model that describes accurately the crystallization process using an internal electric field is not yet available, and should be matter of interest for physical chemists[168]. This research will also give us more insights about the details of the crystallization process and will lead us to optimize the crystallization prior to using our system. In addition, developing a suitable microarray layout design to achieve enhanced compaction and nucleation of crystal growth, and if possible, to conduct several experiments at the same time with disposable materials would further increase the efficiency and reduce the cost of instrumentation. Patterning techniques [188-190] will allow us to induce a preferred surface alignment state at the electrode surface to promote nucleation and growth of single crystals for structural analysis. Coupling with x-ray diffraction to build up a real-time *in-situ* crystal structure analysis would be the goal of this study.

6.2.5 A Microfluidic Electrochemical-Based Quantitative PCR (qPCR) Chip

As abovementioned in chapter 3.3, we demonstrated a promising opportunity for real-time PCR detection and quantitation. In our knowledge, most common detection scheme for micro-PCR is based on fluorescence markers [191, 192]. Even though electrochemical-based detection has been reported currently, probe-modified electrodes and asymmetric PCR are still required to produce single-stranded target amplicons[27, 193, 194]. Gong's group[195] reported a relatively simple electrochemical-based micro-device to detect amplicons on bare electrodes *via* the changes of current signal of methylene blue as an electrochemically active species in the PCR mixture. Comparing our approach with these above methods, recording electrode reflectivity *via* electrochemical dissolution on bare electrodes and without additives is much more straightforward and simple operation. Further study to establish the relationship with PCR cycle-by-cycle and the calibration curve based on the threshold cycle (C_t) and DNA concentration would provide *in situ* quantification of the PCR amplicon and decide the detection limitation. Advanced functionalization with heaters/temperature sensors and superimposing a hydrodynamic flow can be developed for an *in situ* qPCR micro-system in the future with a commercialization potential.

REFERENCES

[1] O. Clerc, G. Greub, *Clinical Microbiology and Infection* **2010**, *16*, 1054.

[2] V. Gubala, L. F. Harris, A. J. Ricco, M. X. Tan, D. E. Williams, *Analytical Chemistry* **2012**, *84*, 487.

[3] L. Gervais, N. de Rooij, E. Delamarche, *Advanced Materials* **2011**, *23*, H151.

[4] C. D. Chin, V. Linder, S. K. Sia, *Lab on a Chip* **2012**, *12*, 2118.

[5] S. Choi, M. Goryll, L. Y. M. Sin, P. K. Wong, J. Chae, *Microfluidics and Nanofluidics* **2011**, *10*, 231.

[6] M. Koets, T. van der Wijk, J. van Eemeren, A. van Amerongen, M. W. J. Prins, *Biosensors & Bioelectronics* **2009**, *24*, 1893.

[7] A. W. Martinez, S. T. Phillips, G. M. Whitesides, E. Carrilho, *Analytical Chemistry* **2010**, *82*, 3.

[8] O. Mudanyali, D. Tseng, C. Oh, S. O. Isikman, I. Sencan, W. Bishara, C. Oztoprak, S. K. Seo, B. Khademhosseini, A. Ozcan, *Lab on a Chip* **2010**, *10*, 1417.

[9] D. Tseng, O. Mudanyali, C. Oztoprak, S. O. Isikman, I. Sencan, O. Yaglidere, A. Ozcan, *Lab on a Chip* **2010**, *10*, 1787.

[10] S. K. Sia, L. J. Kricka, *Lab on a Chip* **2008**, *8*, 1982.

[11] J. Durner, *Angewandte Chemie-International Edition* **2010**, *49*, 1026.

[12] K. B. Mogensen, H. Klank, J. P. Kutter, *Electrophoresis* **2004**, *25*, 3498.

[13] W. R. Vandaveer, S. A. Pasas-Farmer, D. J. Fischer, C. N. Frankenfeld, S. M. Lunte, *Electrophoresis* **2004**, *25*, 3528.

[14] A. M. Armani, R. P. Kulkarni, S. E. Fraser, R. C. Flagan, K. J. Vahala, *Science* **2007**, *317*, 783.

[15] V. Backman, R. Gurjar, K. Badizadegan, L. Itzkan, R. R. Dasari, L. T. Perelman, M. S. Feld, *Ieee Journal of Selected Topics in Quantum Electronics* **1999**, *5*, 1019.

[16] J. Emmelkamp, F. Wolbers, H. Andersson, R. S. DaCosta, B. C. Wilson, I. Vermes, A. van den Berg, *Electrophoresis* **2004**, *25*, 3740.

[17] T. Park, S. Lee, G. H. Seong, J. Choo, E. K. Lee, Y. S. Kim, W. H. Ji, S. Y. Hwang, D. G. Gweon, *Lab on a Chip* **2005**, *5*, 437.

[18] W. K. Ridgeway, E. Seitaridou, R. Phillips, J. R. Williamson, *Nucleic Acids Research* **2009**, *37*.

[19] A. C. Romano, E. M. Espana, S. H. Yoo, M. T. Budak, J. M. Wolosin, S. C. G. Tseng, *Investigative Ophthalmology & Visual Science* **2003**, *44*, 5125.

[20] H. Shao, D. Kumar, K. L. Lear, *Ieee Sensors Journal* **2006**, *6*, 1543.

[21] N. J. Petersen, K. B. Mogensen, J. P. Kutter, *Electrophoresis* **2002**, *23*, 3528.

[22] B. Filanoski, S. K. Rastogi, E. Cameron, N. N. Mishra, W. Maki, G. Maki, *Luminescence* **2008**, *23*, 22.

[23] X. X. Cai, N. Klauke, A. Glidle, P. Cobbold, G. L. Smith, J. M. Cooper, *Analytical Chemistry* **2002**, *74*, 908.

[24] J. C. Fanguy, C. S. Henry, *Electrophoresis* **2002**, *23*, 767.

[25] Z. Y. Wu, F. Fang, J. Josserand, H. H. Girault, *Electrophoresis* **2007**, *28*, 4612.

[26] M. Zuborova, Z. Demianova, D. Kaniansky, M. Masar, B. Stanislawski, *Journal of Chromatography A* **2003**, *990*, 179.

[27] R. H. Liu, J. N. Yang, R. Lenigk, J. Bonanno, P. Grodzinski, *Analytical Chemistry* **2004**, *76*, 1824.

[28] J. M. Armenta, A. A. Dawoud, I. M. Lazar, *Electrophoresis* **2009**, *30*, 1145.

[29] A. K. Naik, M. S. Hanay, W. K. Hiebert, X. L. Feng, M. L. Roukes, *Nature Nanotechnology* **2009**, *4*, 445.

[30] L. S. Bouchard, S. R. Burt, M. S. Anwar, K. V. Kovtunov, I. V. Koptyug, A. Pines, *Science* **2008**, *319*, 442.

[31] M. Mujika, S. Arana, E. Castano, M. Tijero, R. Vilares, J. M. Ruano-Lopez, A. Cruz, L. Sainz, J. Berganza, *Biosensors & Bioelectronics* **2009**, *24*, 1253.

[32] O. Tamarm, S. Comeau, C. Dejous, D. Moynet, D. Rebiere, J. Bezian, J. Pistre, *Biosensors & Bioelectronics* **2003**, *18*, 755.

[33] A. Q. Liu, H. J. Huang, L. K. Chin, Y. F. Yu, X. C. Li, *Analytical and Bioanalytical Chemistry* **2008**, *391*, 2443.

[34] C. Boozer, G. Kim, S. X. Cong, H. W. Guan, T. Londergan, *Current Opinion in Biotechnology* **2006**, *17*, 400.

[35] X. D. Hoa, A. G. Kirk, M. Tabrizian, *Biosensors & Bioelectronics* **2007**, *23*, 151.

[36] J. Wang, *Electroanalysis* **2005**, *17*, 1133.

[37] T. G. Drummond, M. G. Hill, J. K. Barton, *Nature Biotechnology* **2003**, *21*, 1192.

[38] A. T. Woolley, K. Q. Lao, A. N. Glazer, R. A. Mathies, *Analytical Chemistry* **1998**, *70*, 684.

[39] M. G. Olsen, J. M. Bauer, D. J. Beebe, *Applied Physics Letters* **2000**, *76*, 3310.

[40] D. Ross, M. Gaitan, L. E. Locascio, *Analytical Chemistry* **2001**, *73*, 4117.

[41] J. Wu, M. Gu, *Journal of Biomedical Optics* **2011**, *16*.

[42] I. M. Lazar, J. Grym, F. Foret, *Mass Spectrometry Reviews* **2006**, *25*, 573.

[43] A. Niemz, T. M. Ferguson, D. S. Boyle, *Trends in Biotechnology* **2011**, *29*, 240.

[44] S. L. Gutierres, T. E. Welty, *Annals of Pharmacotherapy* **2004**, *38*, 119.

[45] P. Yager, G. J. Domingo, J. Gerdes, in *Annual Review of Biomedical Engineering, Vol. 10*, **2008**, pp. 107.

[46] R. W. Peeling, D. Mabey, *Clinical Microbiology and Infection* **2010**, *16*, 1062.

[47] B. H. Weigl, D. S. Boyle, T. de los Santos, R. B. Peck, M. S. Steele, *Expert Review of Medical Devices* **2009**, *6*, 461.

[48] P. Yager, T. Edwards, E. Fu, K. Helton, K. Nelson, M. R. Tam, B. H. Weigl, *Nature* **2006**, *442*, 412.

[49] P. Gascoyne, J. Satayavivad, M. Ruchirawat, *Acta Tropica* **2004**, *89*, 357.

[50] M. A. Dineva, L. Mahilum-Tapay, H. Lee, *Analyst* **2007**, *132*, 1193.

[51] S. Raja, J. Ching, L. Q. Xi, S. J. Hughes, R. Chang, W. Wong, W. McMillan, W. E. Gooding, K. S. McCarty, M. Chestney, J. D. Luketich, T. E. Godfrey, *Clinical Chemistry* **2005**, *51*, 882.

[52] S. Tanriverdi, L. J. Chen, S. Q. Chen, *Journal of Infectious Diseases* **2010**, *201*, S52.

[53] P. Sabounchi, A. M. Morales, P. Ponce, L. P. Lee, B. A. Simmons, R. V. Davalos, *Biomedical Microdevices* **2008**, *10*, 661.

[54] P. M. Milos, *Expert Review of Molecular Diagnostics* **2009**, *9*, 659.

[55] P. R. Nair, M. A. Alam, *Ieee Transactions on Electron Devices* **2007**, *54*, 3400.

[56] D. Stoddart, A. J. Heron, E. Mikhailova, G. Maglia, H. Bayley, *Proceedings of the National Academy of Sciences of the United States of America* **2009**, *106*, 7702.

[57] M. Barbaro, A. Bonfiglio, L. Raffo, A. Alessandrini, P. Facci, I. Barak, *Ieee Electron Device Letters* **2006**, *27*, 595.

[58] M. Ben Ali, M. Lemiti, N. Jaffrezic-Renault, C. Martelet, J. M. Chovelon, H. Ben Ouada, *Thin Solid Films* **2001**, *383*, 292.

[59] F. A. Shaikh, V. M. Ugaz, *Proceedings of the National Academy of Sciences of the United States of America* **2006**, *103*, 4825.

[60] F. Livolant, A. Leforestier, *Progress in Polymer Science* **1996**, *21*, 1115.

[61] M. Nakata, G. Zanchetta, B. D. Chapman, C. D. Jones, J. O. Cross, R. Pindak, T. Bellini, N. A. Clark, *Science* **2007**, *318*, 1276.

[62] Z. Reich, E. J. Wachtel, A. Minsky, *Science* **1994**, *264*, 1460.

[63] R. L. Rill, T. E. Strzelecka, M. W. Davidson, D. H. Vanwinkle, *Physica A* **1991**, *176*, 87.

[64] A. E. Nkodo, J. M. Garnier, B. Tinland, H. J. Ren, C. Desruisseaux, L. C. McCormick, G. Drouin, G. W. Slater, *Electrophoresis* **2001**, *22*, 2424.

[65] T. E. McKnight, C. T. Culbertson, S. C. Jacobson, J. M. Ramsey, *Analytical Chemistry* **2001**, *73*, 4045.

[66] B. J. Kirby, E. F. Hasselbrink, *Electrophoresis* **2004**, *25*, 187.

[67] N. C. Stellwagen, C. Gelfi, P. G. Righetti, *Biopolymers* **1997**, *42*, 687.

[68] S. Magnusdottir, H. Isambert, C. Heller, J. L. Viovy, *Biopolymers* **1999**, *49*, 385.

[69] L. Mitnik, C. Heller, J. Prost, J. L. Viovy, *Science* **1995**, *267*, 219.

[70] L. J. J. Janssen, C. Sillen, E. Barendrecht, S. J. D. Vanstralen, *Electrochimica Acta* **1984**, *29*, 633.

[71] D. Kohlheyer, J. C. T. Eijkel, S. Schlautmann, A. van den Berg, R. B. M. Schasfoort, *Analytical Chemistry* **2008**, *80*, 4111.

[72] S. H. Chiu, C. H. Liu, *Lab on a Chip* **2009**, *9*, 1524.

[73] S. J. Yang, P. C. Tsai, E. S. Kooij, A. Prosperetti, H. J. W. Zandvliet, D. Lohse, *Langmuir* **2009**, *25*, 1466.

[74] F. A. Shaikh, V. M. Ugaz, *DNA focusing using microfabricated electrode arrays, Vol. 544*, Humana Press, Inc., Totowa, NJ, **2009**.

[75] H. Cai, Y. Q. Wang, P. G. He, Y. H. Fang, *Analytica Chimica Acta* **2002**, *469*, 165.

[76] M. Ozsoz, A. Erdem, K. Kerman, D. Ozkan, B. Tugrul, N. Topcuoglu, H. Ekren, M. Taylan, *Analytical Chemistry* **2003**, *75*, 2181.

[77] S. I. Stoeva, J. S. Lee, C. S. Thaxton, C. A. Mirkin, *Angewandte Chemie-International Edition* **2006**, *45*, 3303.

[78] X. Su, R. Kanjanawarut, *Acs Nano* **2009**, *3*, 2751.

[79] X. Zhang, H. Su, S. Bi, S. Li, S. Zhang, *Biosensors & Bioelectronics* **2009**, *24*, 2730.

[80] J. Wang, G. D. Liu, A. Merkoci, *Journal of the American Chemical Society* **2003**, *125*, 3214.

[81] D. R. Baselt, G. U. Lee, M. Natesan, S. W. Metzger, P. E. Sheehan, R. J. Colton, *Biosensors & Bioelectronics* **1998**, *13*, 731.

[82] M. M. Miller, P. E. Sheehan, R. L. Edelstein, C. R. Tamanaha, L. Zhong, S. Bounnak, L. J. Whitman, R. J. Colton, *Journal of Magnetism and Magnetic Materials* **2001**, *225*, 138.

[83] J. Wang, A. B. Kawde, *Analyst* **2002**, *127*, 383.

[84] J. Fritz, M. K. Baller, H. P. Lang, H. Rothuizen, P. Vettiger, E. Meyer, H. J. Guntherodt, C. Gerber, J. K. Gimzewski, *Science* **2000**, *288*, 316.

[85] F. Huber, M. Hegner, C. Gerber, H. J. Guntherodt, H. P. Lang, *Biosensors & Bioelectronics* **2006**, *21*, 1599.

[86] R. McKendry, J. Y. Zhang, Y. Arntz, T. Strunz, M. Hegner, H. P. Lang, M. K. Baller, U. Certa, E. Meyer, H. J. Guntherodt, C. Gerber, *Proceedings of the National Academy of Sciences of the United States of America* **2002**, *99*, 9783.

[87] Y.-W. Huang, F. A. Shaikh, V. M. Ugaz, *Angewandte Chemie-International Edition* **2011**, *50*, 3739.

[88] F. C. Richard, A. C. M. Bourg, *Water Research* **1991**, *25*, 807.

[89] L. J. Zhang, Y. Zhang, X. H. Zhang, Z. X. Li, G. X. Shen, M. Ye, C. H. Fan, H. P. Fang, J. Hu, *Langmuir* **2006**, *22*, 8109.

[90] A. Gencoglu, A. Minerick, *Lab on a Chip* **2009**, *9*, 1866.

[91] G. T. Burstein, M. A. Kearns, J. Woodward, *Nature* **1983**, *301*, 692.

[92] D. M. Drazic, J. P. Popic, *Journal of the Serbian Chemical Society* **2005**, *70*, 489.

[93] D. M. Drazic, J. P. Popic, B. Jegdic, D. Vasiljevic-Radovic, *Journal of the Serbian Chemical Society* **2004**, *69*, 1099.

[94] http://www.amazon.com/Apple-iPhone-Magnify-Microscope-Light/dp/B0055V5PEA/ref%C2%BCsr_1_1?ie%C2%BCUTF8&qid%C2%BC1342552556&sr%C2%BC8-1&keywords%C2%BCiphone+microscope, search for iPhone microscope, accessed 7 August 2013.

[95] C. Gabrielli, F. Huet, M. Keddam, A. Sahar, *Journal of Applied Electrochemistry* **1989**, *19*, 683.

[96] F. Huet, M. Musiani, R. P. Nogueira, *Journal of Solid State Electrochemistry* **2004**, *8*, 786.

[97] P. B. Duncan, D. Needham, *Langmuir* **2004**, *20*, 2567.

[98] P. S. Epstein, M. S. Plesset, *Journal of Chemical Physics* **1950**, *18*, 1505.

[99] S. Ljunggren, J. C. Eriksson, *Colloids and Surfaces a-Physicochemical and Engineering Aspects* **1997**, *130*, 151.

[100] L. E. Scriven, *Chemical Engineering Science* **1959**, *10*, 1.

[101] M. Borden, *Soft Matter* **2009**, *5*, 716.

[102] M. A. Borden, C. F. Caskey, E. Little, R. J. Gillies, K. W. Ferrara, *Langmuir* **2007**, *23*, 9401.

[103] M. A. Borden, G. V. Martinez, J. Ricker, N. Tsvetkova, M. Longo, R. J. Gillies, P. A. Dayton, K. W. Ferrara, *Langmuir* **2006**, *22*, 4291.

[104] E. Dressaire, R. Bee, D. C. Bell, A. Lips, H. A. Stone, *Science* **2008**, *320*, 1198.

[105] D. H. Kim, M. J. Costello, P. B. Duncan, D. Needham, *Langmuir* **2003**, *19*, 8455.

[106] K. Ferrara, R. Pollard, M. Borden, *Annual Review of Biomedical Engineering* **2007**, *9*, 415.

[107] P. Jauregi, J. Varley, *Trends in Biotechnology* **1999**, *17*, 389.

[108] F. Sebba, *Journal of Colloid and Interface Science* **1971**, *35*, 643.

[109] J. R. Lindner, *Nature Reviews Drug Discovery* **2004**, *3*, 527.

[110] E. G. Schutt, D. H. Klein, R. M. Mattrey, J. G. Riess, *Angewandte Chemie-International Edition* **2003**, *42*, 3218.

[111] S. Huber, T. Helbich, J. Kettenbach, W. Dock, I. Zuna, S. Delorme, *Radiology* **1998**, *208*, 485.

[112] I. Lentacker, B. G. De Geest, R. E. Vandenbroucke, L. Peeters, J. Demeester, S. C. De Smedt, N. N. Sanders, *Langmuir* **2006**, *22*, 7273.

[113] K. Bjerknes, K. Dyrstad, G. Smistad, I. Agerkvist, *Drug Development and Industrial Pharmacy* **2000**, *26*, 847.

[114] U. Farook, E. Stride, M. J. Edirisinghe, *Journal of the Royal Society Interface* **2009**, *6*, 271.

[115] M. Kukizaki, M. Goto, *Journal of Membrane Science* **2006**, *281*, 386.

[116] E. C. Unger, T. P. McCreery, R. H. Sweitzer, V. E. Caldwell, Y. Q. Wu, *Investigative Radiology* **1998**, *33*, 886.

[117] A. M. Ganan-Calvo, J. M. Gordillo, *Physical Review Letters* **2001**, *87*, 274501.

[118] K. Hettiarachchi, E. Talu, M. L. Longo, P. A. Dayton, A. P. Lee, *Lab on a Chip* **2007**, *7*, 463.

[119] K. Pancholi, E. Stride, M. Edirisinghe, *Journal of Drug Targeting* **2008**, *16*, 494.

[120] J. I. Park, Z. Nie, A. Kumachev, A. I. Abdelrahman, B. R. Binks, H. A. Stone, E. Kumacheva, *Angewandte Chemie-International Edition* **2009**, *48*, 5300.

[121] J. H. Xu, S. W. Li, Y. J. Wang, G. S. Luo, *Applied Physics Letters* **2006**, *88*.

[122] J. Wu, W. L. Nyborg, *Advanced Drug Delivery Reviews* **2008**, *60*, 1103.

[123] J. A. Feshitan, C. C. Chen, J. J. Kwan, M. A. Borden, *Journal of Colloid and Interface Science* **2009**, *329*, 316.

[124] G. M. Whitesides, *Nature* **2006**, *442*, 368.

[125] E. Stride, M. Edirisinghe, *Soft Matter* **2008**, *4*, 2350.

[126] P. G. Deng, Y. K. Lee, P. Cheng, *Journal of Micromechanics and Microengineering* **2004**, *14*, 693.

[127] S. Z. Hua, F. Sachs, D. X. Yang, H. D. Chopra, *Analytical Chemistry* **2002**, *74*, 6392.

[128] M. S. Plesset, A. Prosperetti, *Annual Review of Fluid Mechanics* **1977**, *9*, 145.

[129] A. Cifuentes, J. L. Bernal, J. C. DiezMasa, *Analytical Chemistry* **1997**, *69*, 4271.

[130] P. L. Luisi, *Angewandte Chemie-International Edition in English* **1985**, *24*, 439.

[131] P. F. Flynn, A. K. Simorellis, W. D. Van Horn, in *Annual Reports on Nmr Spectroscopy, Vol 62, Vol. 62* (Ed.: G. A. Webb), **2007**, pp. 179.

[132] E. Acosta, M. Bisceglia, J. C. Fernandez, *Colloids and Surfaces a-Physicochemical and Engineering Aspects* **2000**, *161*, 417.

[133] Z. H. Nie, M. S. Seo, S. Q. Xu, P. C. Lewis, M. Mok, E. Kumacheva, G. M. Whitesides, P. Garstecki, H. A. Stone, *Microfluidics and Nanofluidics* **2008**, *5*, 585.

[134] A. McPherson, *Journal of Crystal Growth* **1991**, *110*, 1.

[135] S. D. Durbin, G. Feher, *Annual Review of Physical Chemistry* **1996**, *47*, 171.

[136] M. J. F. Austin, L. Babiss, *Aaps Journal* **2006**, *8*, E185.

[137] B. B. Spear, M. Heath-Chiozzi, J. Huff, *Trends in Molecular Medicine* **2001**, *7*, 201.

[138] N. E. Chayen, E. Saridakis, *Nature Methods* **2008**, *5*, 147.

[139] S. E. Brenner, *Nature Reviews Genetics* **2001**, *2*, 801.

[140] N. E. Chayen, *Current Opinion in Structural Biology* **2004**, *14*, 577.

[141] N. E. Chayen, *Acta Crystallographica Section D-Biological Crystallography* **1998**, *54*, 8.

[142] L. Li, R. F. Ismagilov, in *Annual Review of Biophysics, Vol 39, Vol. 39* (Eds.: D. C. Rees, K. A. Dill, J. R. Williamson), **2010**, pp. 139.

[143] C. Hansen, S. R. Quake, *Current Opinion in Structural Biology* **2003**, *13*, 538.

[144] W. B. Du, L. Li, K. P. Nichols, R. F. Ismagilov, *Lab on a Chip* **2009**, *9*, 2286.

[145] C. L. Hansen, E. Skordalakes, J. M. Berger, S. R. Quake, *Proceedings of the National Academy of Sciences of the United States of America* **2002**, *99*, 16531.

[146] L. Li, D. Mustafi, Q. Fu, V. Tereshko, D. L. L. Chen, J. D. Tice, R. F. Ismagilov, *Proceedings of the National Academy of Sciences of the United States of America* **2006**, *103*, 19243.

[147] S. L. Perry, G. W. Roberts, J. D. Tice, R. B. Gennis, P. J. A. Kenis, *Crystal Growth & Design* **2009**, *9*, 2566.

[148] B. Zheng, C. J. Gerdts, R. F. Ismagilov, *Current Opinion in Structural Biology* **2005**, *15*, 548.

[149] B. Zheng, R. F. Ismagilov, *Angewandte Chemie-International Edition* **2005**, *44*, 2520.

[150] B. Zheng, L. S. Roach, R. F. Ismagilov, *Journal of the American Chemical Society* **2003**, *125*, 11170.

[151] B. Zheng, L. S. Roach, J. D. Tice, C. J. Gerdts, D. Chen, R. F. Ismagilov, in *Micro Total Analysis Systems 2004, Vol 2* (Eds.: T. Laurell, J. Nilsson, K. Jensen, D. J. Harrison), **2005**, pp. 145.

[152] B. Zheng, J. D. Tice, R. F. Ismagilov, *Analytical Chemistry* **2004**, *76*, 4977.

[153] B. Zheng, J. D. Tice, L. S. Roach, R. F. Ismagilov, *Angewandte Chemie-International Edition* **2004**, *43*, 2508.

[154] R. Boistelle, J. P. Astier, G. Marchismouren, V. Desseaux, R. Haser, *Journal of Crystal Growth* **1992**, *123*, 109.

[155] M. Ataka, E. Katoh, N. I. Wakayama, *Journal of Crystal Growth* **1997**, *173*, 592.

[156] G. Sazaki, E. Yoshida, H. Komatsu, T. Nakada, S. Miyashita, K. Watanabe, *Journal of Crystal Growth* **1997**, *173*, 231.

[157] A. Kadri, B. Lorber, G. Jenner, R. Giege, *Journal of Crystal Growth* **2002**, *245*, 109.

[158] C. Charron, M. C. Robert, B. Capelle, A. Kadri, G. Jenner, R. Giege, B. Lorber, *Journal of Crystal Growth* **2002**, *245*, 321.

[159] S. Ueno, R. I. Ristic, K. Higaki, K. Sato, *Journal of Physical Chemistry B* **2003**, *107*, 4927.

[160] C. N. Nanev, A. Penkova, *Journal of Crystal Growth* **2001**, *232*, 285.

[161] M. Taleb, C. Didierjean, C. Jelsch, J. P. Mangeot, A. Aubry, *Journal of Crystal Growth* **2001**, *232*, 250.

[162] M. Taleb, C. Didierjean, C. Jelsch, J. P. Mangeot, B. Capelle, A. Aubry, *Journal of Crystal Growth* **1999**, *200*, 575.

[163] A. Moreno, G. Sazaki, *Journal of Crystal Growth* **2004**, *264*, 438.

[164] G. Sazaki, A. Moreno, K. Nakajima, *Journal of Crystal Growth* **2004**, *262*, 499.

[165] N. Mirkin, B. A. Frontana-Uribe, A. Rodriguez-Romero, A. Hernandez-Santoyo, A. Moreno, *Acta Crystallographica Section D-Biological Crystallography* **2003**, *59*, 1533.

[166] M. I. Al-Haq, E. Lebrasseur, W. K. Choi, H. Tsuchiya, T. Torii, H. Yamazaki, E. Shinohara, *Journal of Applied Crystallography* **2007**, *40*, 199.

[167] Z. Hammadi, S. Veesler, *Progress in Biophysics & Molecular Biology* **2009**, *101*, 38.

[168] B. A. Frontana-Uribe, A. Moreno, *Crystal Growth & Design* **2008**, *8*, 4194.

[169] Y. Perez, D. Eid, F. Acosta, L. Marin-Garcia, J. Jakoncic, V. Stojanoff, B. A. Frontana-Uribe, A. Moreno, *Crystal Growth & Design* **2008**, *8*, 2493.

[170] P. J. Espinoza-Montero, M. Esther Moreno-Narvaez, B. A. Frontana-Uribe, V. Stojanoff, A. Moreno, *Crystal Growth & Design* **2012**, *13*, 590.

[171] Z. Hammadi, J. P. Astier, R. Morin, S. Veesler, *Crystal Growth & Design* **2007**, *7*, 1472.

[172] C. Charron, C. Didierjean, J. P. Mangeot, A. Aubry, *Journal of Applied Crystallography* **2003**, *36*, 1482.

[173] B. R. Silver, P. R. Unwin, *Chemical Communications* **2008**, 5179.

[174] Z. Hammadi, J. P. Astier, R. Morin, S. Veesler, *Crystal Growth & Design* **2009**, *9*, 3346.

[175] M. I. Al-Haq, E. Lebrasseur, H. Tsuchiya, T. Torii, *Crystallography Reviews* **2007**, *13*, 29.

[176] C. C. Chin, J. B. Dence, J. C. Warren, *Journal of Biological Chemistry* **1976**, *251*, 3700.

[177] F. Shaikh, Ph.D thesis, Texas A&M University (College Station), **2008**.

[178] H. Zhu, O. Yaglidere, T.-W. Su, D. Tseng, A. Ozcan, *Lab on a Chip* **2011**, *11*, 315.

[179] M. A. Unger, H. P. Chou, T. Thorsen, A. Scherer, S. R. Quake, *Science* **2000**, *288*, 113.

[180] W. H. Grover, A. M. Skelley, C. N. Liu, E. T. Lagally, R. A. Mathies, *Sensors and Actuators B-Chemical* **2003**, *89*, 315.

[181] R. Al Shakarji, Y. He, S. Gregory, *Hydrometallurgy* **2011**, *109*, 168.

[182] S. Sirsi, M. Borden, *Bubble science engineering and technology* **2009**, *1*, 3.

[183] H. Corstjens, H. A. H. Billiet, J. Frank, K. Luyben, *Electrophoresis* **1996**, *17*, 137.

[184] S. Kassegne, B. Arya, N. Yadav, *Sensors and Actuators B: Chemical* **2010**, *143*, 470.

[185] C. R. Cabrera, B. Finlayson, P. Yager, *Analytical Chemistry* **2001**, *73*, 658.

[186] I. L. Arnaud, J. Josserand, J. S. Rossier, H. H. Girault, *Electrophoresis* **2002**, *23*, 3253.

[187] J. Vazquez, J. L. Sanchez-Rojas, *Current Applied Physics* **2009**, *9*, 333.

[188] N. E. Chayen, E. Saridakis, R. El-Bahar, Y. Nemirovsky, *Journal of Molecular Biology* **2001**, *312*, 591.

[189] N. E. Chayen, E. Saridakis, R. P. Sear, *Proceedings of the National Academy of Sciences of the United States of America* **2006**, *103*, 597.

[190] V. K. Gupta, N. L. Abbott, *Science* **1997**, *276*, 1533.

[191] E. A. Ottesen, J. W. Hong, S. R. Quake, J. R. Leadbetter, *Science* **2006**, *314*, 1464.

[192] P. Belgrader, S. Young, B. Yuan, M. Primeau, L. A. Christel, F. Pourahmadi, M. A. Northrup, *Analytical Chemistry* **2001**, *73*, 286.

[193] R. Y. Lai, E. T. Lagally, S. H. Lee, H. T. Soh, K. W. Plaxco, A. J. Heeger, *Proceedings of the National Academy of Sciences of the United States of America* **2006**, *103*, 4017.

[194] T. M. H. Lee, M. C. Carles, I. M. Hsing, *Lab on a Chip* **2003**, *3*, 100.

[195] T. H. Fang, N. Ramalingam, D. Xian-Dui, T. S. Ngin, Z. Xianting, A. T. Lai Kuan, E. Y. Peng Huat, G. Hai-Qing, *Biosensors and Bioelectronics* **2009**, *24*, 2131.